DEFORMATION ANALYSIS OF SAND SPECIMENS USING 3D DIGITAL IMAGE CORRELATION FOR THE CALIBRATION OF AN ELASTO-PLASTIC MODEL

A Dissertation

by

AHRAN SONG

Submitted to the Office of Graduate Studies of
Texas A&M University
in partial fulfillment of the requirements for the degree of

DOCTOR OF PHILOSOPHY

August 2012

Major Subject: Civil Engineering

Deformation Analysis of Sand Specimens using 3D Digital Image Correlation for the Calibration of an Elasto-Plastic Model

DEFORMATION ANALYSIS OF SAND SPECIMENS USING 3D DIGITAL IMAGE CORRELATION FOR THE CALIBRATION OF AN ELASTO-PLASTIC MODEL

A Dissertation

by

AHRAN SONG

Submitted to the Office of Graduate Studies of
Texas A&M University
in partial fulfillment of the requirements for the degree of

DOCTOR OF PHILOSOPHY

Approved by:

Chair of Committee,	Zenon Medina-Cetina
Committee Members,	Marcelo Sanchez
	Chloe Arson
	Javier Jo
	Gokhan Saygili
Head of Department,	John Niedzwecki

August 2012

Major Subject: Civil Engineering

ABSTRACT

Deformation Analysis of Sand Specimens using 3D Digital Image Correlation for the Calibration of an Elasto-Plastic Model. (August 2012)

Ahran Song, B.S., Sungkyunkwan University, South Korea;

M.S., Sungkyunkwan University, South Korea

Chair of Advisory Committee: Dr. Zenon Medina-Cetina

The use of Digital Image Correlation (DIC) technique has become increasingly popular for displacement measurements and for characterizing localized material deformation. In this study, a three-dimensional digital image correlation analysis (3D-DIC) was performed to investigate the displacements on the surface of isotropically consolidated and drained sand specimens during triaxial compression tests.

The deformation of a representative volume of the material captured by 3D-DIC is used for the estimation of the kinematic and volumetric conditions of the specimen at different stages of deformation, combined with the readings of the global axial compression of the specimen. This allowed for the characterization of a Mohr-Coulomb plasticity model with hardening and softening laws.

In addition, a two-dimensional axisymmetric finite element model was built to simulate the actual experimental conditions, including both the global and local kinematics effects captured by 3D digital image correlation analysis on the boundary of the specimen.

A comparison between the axisymmetic model predictions and the experimental observations showed good agreement, for both the global and local behavior, in the case of different sand specimen configuration, including loose, dense and half-loose half-dense specimens.

DEDICATION

To my family

ACKNOWLEDGEMENTS

I would like to thank my committee chair, Prof. Zenon Medina-Cetina for his guidance and provision of financial assistance, and my committee members, Prof. Marcelo Sanchez, Prof. Chloe Arson, Prof. Javier Jo, and Dr. Gokhan Saygili for their sincere advice and support throughout the course of this research.

Thanks are also extended to my friends in geotechnical engineering and colleagues in stochastic geomechanics laboratory group for making my time at Texas A&M University a great experience. I am really grateful to Patricia and Vishal for sharing the happy moments as reliable friends and to Patrick for spending his valuable time to proofread this thesis. Also, I will remember warm and friendly Korean students and their families, especially Seok-gyu who would take care of me all the time.

Finally, thanks to my family for their encouragement and support and to Naoki for his patience during my studies.

TABLE OF CONTENTS

Page

LIST OF FIGURES

Page

Page

Page

Page

Page

LIST OF TABLES

Page

1. INTRODUCTION

1.1 Antecedents

Duncan's state of the art review (1994) on advanced constitutive models provided important key points on the limitations that practice have on the modeling of geotechnical structures. Lade's state of the art review (2005) went further and provided a more specific overview of the principles, characteristic features, and requirements for the calibration of constitutive models, for the proper model selection and implementation in advanced case studies. Potts and Zdravkovic (1999) reviewed various methods of analysis including from closed form to full numerical analysis in terms of the fundamental theoretical solutions, and also provided the ability of each method to satisfy the design requirements. Hicher and Shao (2008) rearranged several failure criteria and suggested the appropriate type of soils for each criterion that is validated by experimental results for a different type of soils. Also, Brinkgreve (2005) stated a difficulty of the selection of soil parameters in terms of insufficient data from correlation and laboratory testing for application in finite element soil models. All these contributions, ignored the effect of material heterogeneity and local kinematic effects at the time of calibrating the constitutive models. Meaning that only considered the global stress and strain effects captured on the axial direction of the specimens.

This dissertation follows the style and format of the *Journal of Geotechnical and Geoenvironmental Engineering*.

Digital image correlation (DIC) is one of the most widely used optical techniques for full displacement measurements, allowing for the identification and characterization of local kinematic effects. DIC developed basically for the characterization of material deformations in the early 1980s, and since then the DIC concept has been extended from 2D DIC using a single camera system, to 3D-DIC using a multi camera system. The major progress on the use of DIC technology can be located in the early 1990s, with advances in the quality of digital camera and computational capabilities (McNeill et al. 1997; Sutton et al. 2000; Sutton et al. 2008). Recently, more elaborated studies of the 3D-DIC technique have been dedicated to improved previous 2D DIC dealing with planar surfaces, in-plane deformations, and perpendicular camera setting to the object surface (Sutton et al. 2008). Nowadays, the development of the 3D-DIC technique permits to measure anisotropic, volumetric and heterogeneous strains (Almeida et al. 2008). For instance, in order to improve the understanding of specimens' failure mechanisms, a 3D-DIC system was implemented for investigating shear and compaction bands in sand specimens (Desrues and Viggiani 2004; Rechenmacher 2006; Charalampidou et al. 2010), showing even at the grain level, the kinematics of these effects. Notice that in the case of a 3D-DIC system using only two cameras, the measurement area for a cylindrical sample is expected to be approximately one third of the circumference due to the maximum overlap area between any given pair of images (Tai et al. 2010).

What these investigations have in common is that they found significant heterogeneous responses in apparently homogeneous specimens, and suggested various

methods for better understanding the effect of full boundary displacement fields. Although previous research has provided valuable information for the understanding of DIC implementation, further research is still required on its incorporation on standard model calibration (Medina-Cetina and Rechenmacher 2010).

Herein, once the notion of incorporating local deformation effects into the calibration process has been discussed, it is fair to mention that the selection of a soil constitutive model itself and its corresponding calibration process are not simple tasks to complete. This process is dependent on several conditions, including its ability to capture the physics associated to the particular application where the model is going to be used, its easiness to apply it, its availability in a numerical solver (i.e. commercial finite element codes), and its feasibility for calibration purposes, among others (Duncan 1994; Potts 2003; Brinkgreve 2005; Lade 2005; Boldyrev et al. 2006).

1.2 Proposed Approach

This work is based on the population of a comprehensive experimental database containing a series of triaxial compression tests on sand specimens performed by Medina-Cetina (2006). This work aims at computing the collected 3D digital image data from the surface of soil specimens using 3D-DIC. That is to generate 3D local kinematic information that is retrieved during a compression test over the surface of the deforming specimen. A comprehensive investigation into the localized deformation of sand specimens using 3D digital image correlation (3D-DIC) is carried out including 3D geometrical transformation and interpolation/extrapolation processes with the aim of

identifying the global behavior of the specimen. From the kinematic and volumetric conditions of the specimen at different stages of deformation, combined with the corresponding readings of the global axial compression of the specimen, this work aims at characterizing simple elasto-plastic constitutive models for quantifying their advantages and limitations for prescribed experimental conditions.

To achieve this goal, first, a qualitative analysis is presented describing typical failure mechanisms on a series of dry sand triaxial specimens; second, a simple elasto-plastic constitutive model with hardening and softening capabilities is calibrated using a single finite element; and finally, a 2D finite element model is developed for comparing the actual experimental results. Results on the modeling of local kinematics effects, demonstrate the ability of the proposed constitutive model to reproduce accurately the overall mechanical behavior of a sand specimen under the given conditions. This approach is further extended for the case of true heterogeneous materials, proving the relevance of accounting for spatial variability of the elasto-plastic constitutive parameters within the numerical model. The calibration process to determine constitutive model parameters is discussed for comparing actual triaxial testing data and numerical predictions when material heterogeneity and evolutionary material degradation is considered. By means of this calibration methodology that accounts for the model performance of soil constitutive models, it can be a meaningful way to determine what constitutive model provides better predictions and practical solutions to the actual soil behavior, when observations on local kinematic effects are available.

2. SOIL EXPERIMENTATION

2.1 Triaxial Testing

The triaxial test and 3D imaging systems setup used to populate the experimental database is presented in Figure 2.1 (Medina-Cetina 2006). A departure from standard triaxial tests was the removal of the Plexiglass cell to avoid reflection and refraction effects by light and fluid, respectively. This means that tests were conducted on sand specimens vacuum consolidated, instead of fluid-based consolidation during the image acquisition. An automated triaxial device developed by Geocomp was used to execute the compression tests and to measure the global stress-strain axial response. The 3D imaging system consisted of two digital cameras positioned approximately 25cm from each other, and 50cm from the sample as shown in Figure 2.1 (b).

The material for the triaxial compression test was a dry sand, classified as SP, having Cu=2.34 and Cc=1.11, and provided an adequate color spectrum suitable for pattern recognition during imaging analysis. A specimen was constructed using a standard cylindrical mold following dry pluviation or vibratory compaction methods reaching a relative density varying between 83 and 99% for dense sand specimens and 46% for a loose sand specimen (test 121304b). After the specimen setup, the mold was removed and an isotropic compression of vacuum pressure was applied to the base of the sample with a vacuum pump in order to keep the sample stable. The specimen was loaded with a controlled deformation rate of 0.2% of axial strain/min.

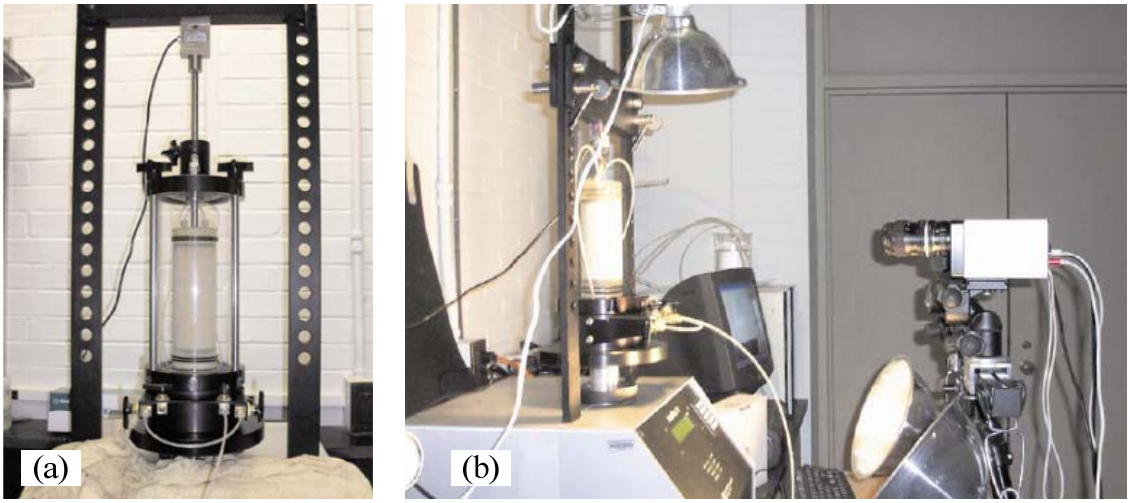

Figure 2. 1 Triaxial Geocomp system (a), and 3D imaging system (b) (Medina-Cetina 2006)

The experimental characteristics of all triaxial tests included in the database are presented in Table 2.1. This shows the results of twenty seven experiments, classified as follows: twenty five dense specimens, one half loose and half dense specimen (test 120704c), and one loose sand specimen (test 121304b). Most specimens were consolidated at 40kPa of vacuum pressure, but three tests were consolidated at a confining pressure of 20kPa (test 121304d) and 60kPa (100103c and 121304c tests) respectively. The average diameter of all specimens was 71.15 mm with a standard deviation of 0.27 mm, and the corresponding average height was 158.31 mm, with a standard deviation of 1.62 mm. After excluding the data of a layered specimen and a loose sand specimen, the dense specimens' average initial density was 1,712.89 kg/m^3 with a standard deviation of 10.10kg/m^3, and the corresponding average relative density was 91.72% with a standard deviation of 3.43% respectively. From all experiments, eighteen samples were prepared in three layers by a vibratory compaction method and

eight samples were prepared by a dry pluviation method. The layered specimen (half loose and half dense) was built in two compacting layers, with the lower half dense layer with relative density of 98.87% and the upper loose layer with relative density of 30.54%. The boundary of two layers was located at the mid height of the specimen.

Table 2. 1 Experimental characteristics of triaxial tests

No.	Test Name	Height (mm)	Diameter (mm)	Initial Density (kg/m^3)	Relative Density (%)	Sample Preparation	Note
1	092903b	155.50	71.33	1,710.95	91.09	Mold tempered	-
2	093003b	156.67	71.41	1,696.00	85.96	Mold tempered	-
3	100103a	157.67	71.29	1,702.22	88.10	Mold tempered	-
4	100103b	155.83	71.24	1,717.13	93.18	Mold tempered	-
5	100103c	157.67	71.54	1,703.87	88.67	Mold tempered	60kPa confinement
6	100103d	154.33	70.86	1,702.41	88.17	Mold tempered	-
7	100203a	157.50	71.45	1,715.32	92.57	Mold tempered	-
8	100203b	155.00	71.48	1,711.91	91.41	Mold tempered	-
9	100303b	158.17	71.29	1,718.70	93.71	Mold tempered	-
10	101104a	159.33	70.87	1,724.89	95.79	Dry Pluviation	Light reflection
11	101204a	160.00	71.46	1,708.03	90.09	Dry Pluviation	-
12	120604a	159.33	71.31	1,721.06	94.50	Dry Pluviation	Light reflection
13	120604b	159.33	70.94	1,715.13	92.50	Dry Pluviation	Light reflection
14	120604c	158.83	70.72	1,717.48	93.30	Mold tempered	Light reflection
15	120604d	158.83	70.84	1,716.99	93.13	Mold tempered	Light reflection
16	120704a	158.83	71.37	1,708.07	90.11	Mold tempered	Light reflection

Table 2. 1 continued

No.	Test Name	Height (mm)	Diameter (mm)	Initial Density (kg/m^3)	Relative Density (%)	Sample Preparation	Note
17	120704b	159.00	71.30	1,686.96	82.82	Mold tempered	Light reflection
18	120704c	157.67	70.88	1,648.06	68.90	Mold tempered	Layered specimen
		79.50	71.27	1,734.17	98.87	-	Lower: dense sand
		78.17	70.68	1,549.61	30.54	-	Upper: loose sand
19	120904a	158.67	71.15	1,707.72	89.99	Mold tempered	Light reflection
20	120904b	160.00	70.98	1,720.40	94.28	Mold tempered	-
21	120904c	159.67	71.11	1,713.13	91.83	Mold tempered	-
22	120904d	159.00	71.13	1,707.89	90.04	Mold tempered	-
23	120904e	160.00	70.99	1,718.70	93.71	Mold tempered	-
24	121304a	160.00	71.30	1,721.73	94.73	Dry Pluviation	-
25	121304b	158.17	70.86	1,588.84	46.39	Dry Pluviation	Loose specimen
26	121304c	160.00	70.48	1,718.72	93.72	Dry Pluviation	60kPa confinement
27	121304d	159.50	71.38	1,736.71	99.71	Dry Pluviation	20kPa confinement

For the sample in a water-filled cell, the cell pressure supplies a uniform radial stress, σ_r, and an additional force, F_a, is measured by a force transducer. If the cross-sectional area of the sample is A, then the total axial stress, σ_a is given by $\sigma_a=\sigma_r+(F_a/A)$. The deviatoric stress, σ_d, is calculated by $\sigma_d=\sigma_a-\sigma_r=(F_a/A)$ (Atkinson and Bransby, 1978). Although dry samples were used for experiments, the test setup satisfies conditions of a conventional drained triaxial compression test. The cell pressure was constant and a

change of volume was allowed while the deviatoric stress increased. Thus, the calculated deviatoric stress is considered in an effective stress.

Global stress-strain curves for all tests are presented in Figure 2.2. For dense sand specimens with a confining pressure of 40kPa, the maximum deviatoric stress oscillated between 220 and 255kPa, and the deviatoric stress at the critical state ranged between 155 and 185kPa. For the two tests with a confining pressure of 60kPa, the deviatoric stresses were 317~359kPa at peak and 265~270kPa at critical state. It is hypothesized that deviations in deviatoric stress with the same confinement condition were caused by the variation of relative density within the specimen as a results of the sample preparation methods. The loose specimen test has no peak stress and yields to 150kPa from 3.2% of axial strain to the critical state. The layered specimen test does not have a typical behavior of a dense sand specimen and shows the behavior of a loose sand specimen.

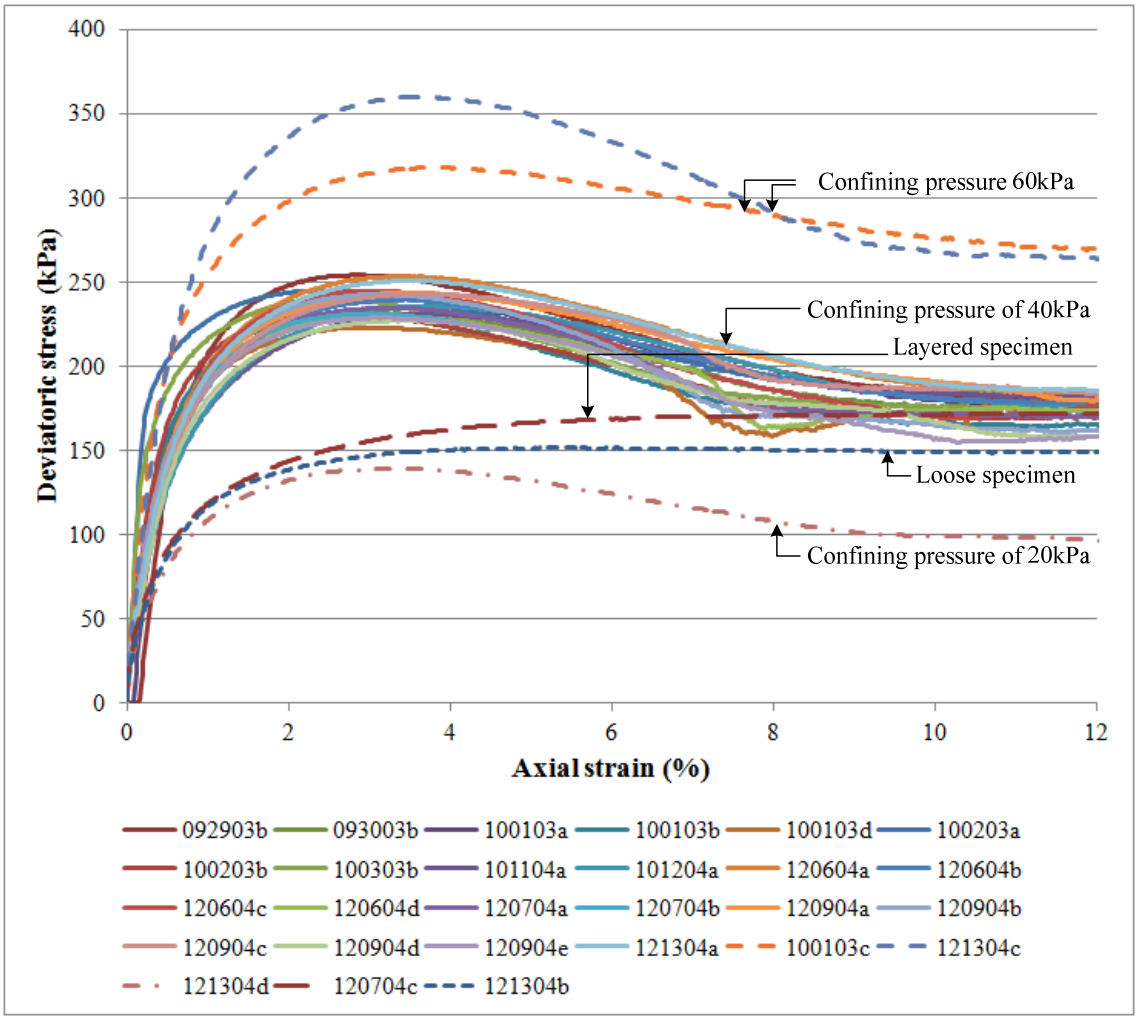

Figure 2. 2 Triaxial stress-strain curves for all tests

Although a dry sample is prepared, the specimen is exposed to the atmospheric air pressure and moisture. This explains the existence of cohesion with respect to matric suction. The shear strength of saturated soils for the Mohr-Coulomb theory is defined as $\tau=c'+(\sigma-u_w)\tan\phi'$, where c' is effective cohesion. The shear strength of unsaturated soils is proposed by Fredlund et al. (1996) as $\tau=c'+(\sigma-u_a)\tan\phi'+(u_a-u_w)\beta\tan\phi'$, where u_a is the pore-air pressure, u_w is the pore-water pressure, (u_a-u_w) is matric suction, and β

represents the decrease in effective stress resistance as matric suction increases. β is dependent on the water content of soil and expressed as being equal to $\tan\phi^b / \tan\phi'$. From the equation, $[(u_a - u_w)\beta\tan\phi']$ part is defined by Peterson (1988) as an apparent cohesion due to suction and it explains the cohesion of the specimen.

However, for the soils above the groundwater level, a conventional saturated soil mechanics concept is generally sufficient for engineering purposes (Powrie 1997). Thus, the assumption of zero cohesion can be acceptable in this study. The parameter, β depends on the saturation ratio and varies from 0 for dry soils to 1 for saturated soils (Powrie 1997; Nuth and Laloui 2008). Assuming a dry sample of the tests, the strength equation becomes $\tau=(\sigma-u_a)\tan\phi'$. If u_a is replaced with σ_r which is vacuum pressure for the dry sample compared with the deviatoric stress form presented above, using vacuum compression as a confining pressure is allowed for the effect stress analysis.

Mohr's circles for experiments on dense sand specimens are illustrated in Figure 2.3. From these result, under the assumption that the cohesion is equal to zero, it is observed that an averaged friction angle at peak strength is calculated as 48.46° with a standard deviation of 0.85°.

A failure envelope and friction angles at the peak strength for dense sand specimens are presented in Figure 2.4. Peak strength data plotted as normal stress vs. shear stress shows a curved failure envelope as seen in Figure 2.4 (a). The friction angle at peak strength is found by means of a best fit straight line, having an equation of the form, $\tau=c+\sigma\tan\phi$, where c is assumed to be equal to zero here for sand specimens. This assumption leads to the overestimation of the actual peak strength at low stress,

depending on how to draw the best fit line (Holtz and Kovacs 1981; Powrie 1997). This results in an apparent peak friction angle higher than the average friction angle at low confining stress, and even lower at high confining stress (Figure 2.4 (b)). Vesic and Clough (1968) depicted this behavior of dense and loose sand specimens with respect to pressure sensitivity. The friction angle of loose samples was the same at different stress levels, but the friction angle of dense samples was sensitive at a low stress level and constant at a high stress level.

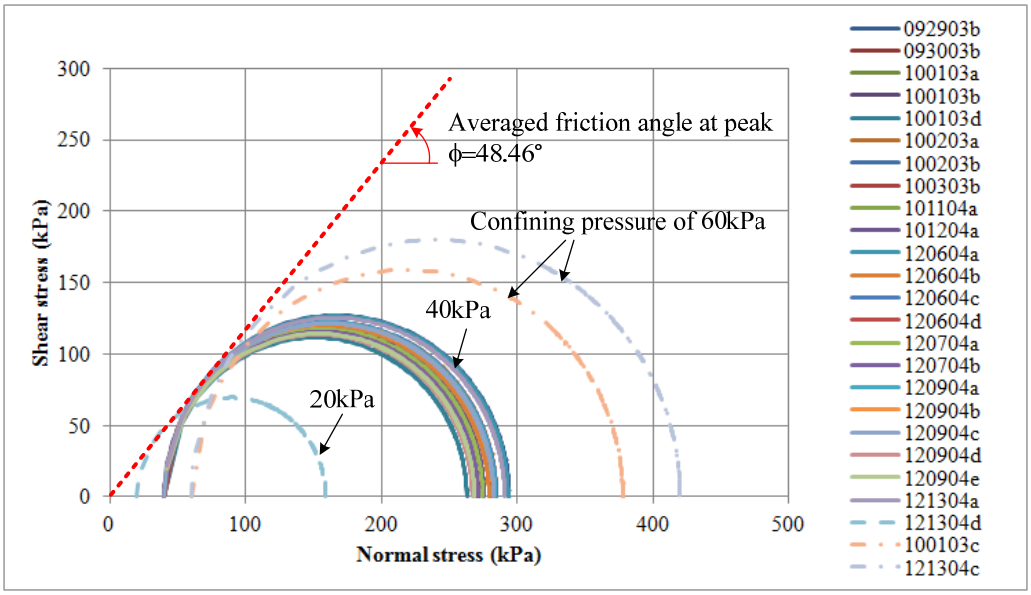

Figure 2. 3 Mohr's circles of triaxial tests for dense specimens

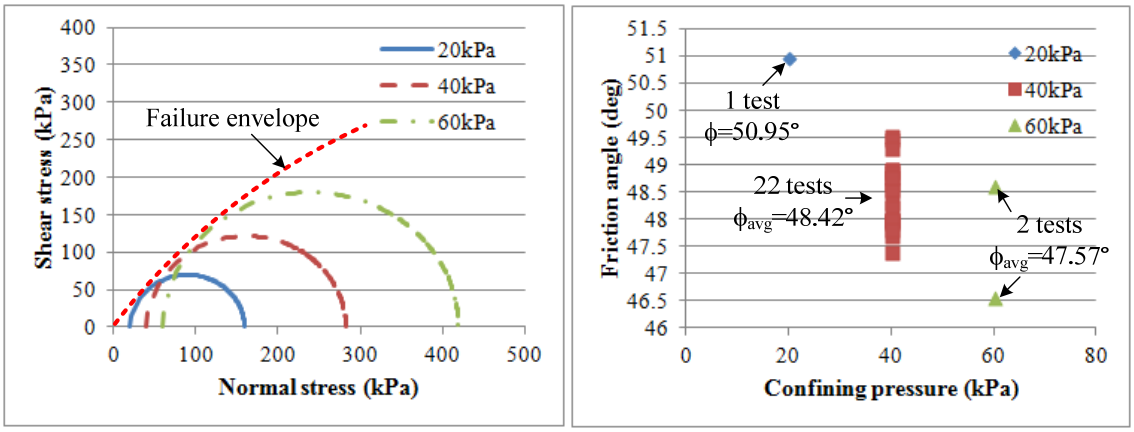

(a) Curved failure envelope (b) Friction angle distribution

Figure 2. 4 Curved failure envelope and friction angles at failure for dense specimens

2.2 3D Digital Image Correlation Analysis

2.2.1 Digital Image Correlation

A digital image correlation technique is a reliable and accurate approach for the investigation of local kinematics, aimed at capturing local phenomena of deforming specimens. 3D digital image correlation (3D-DIC) is developed based on principles similar to human eye's depth perception, viewing the same object from two different viewpoints and judging distance. An innovative qualitative interpretation of the specimen deformation is provided by the use of digital images, which are taken simultaneously every 15 seconds corresponding to 0.05% of axial strain during the triaxial compression test using two 14-bit digital cameras Q-IMAGING PMI-4201, with 4.2 Mega pixels of resolution (2024×2024 pixels). Sample images that capture the state of the sample at deformation stages of 0.2%, 3.6%, 7% and 12% of axial strain by one

digital camera are shown in Figure 2.5. These images illustrate amplification of bulging failure procedure as the state of the sample at the elastic zone, peak stress, softening zone, and critical state, respectively.

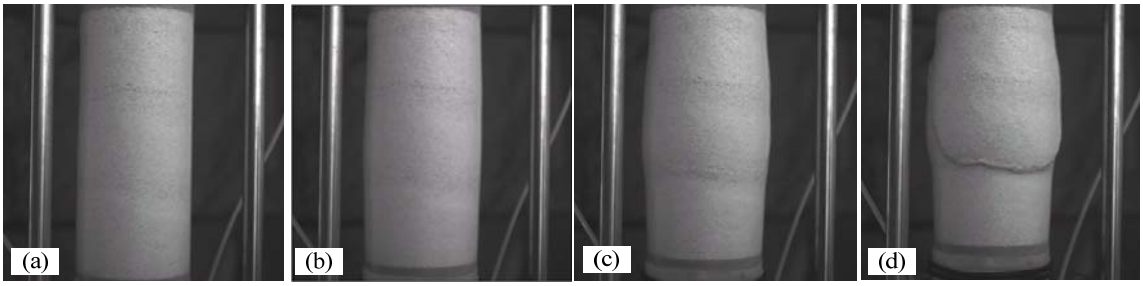

Figure 2. 5 Photo images of test 120904c at (a) 0.2% of axial strain (b) 3.6% of axial strain (c) 7% of axial strain (d) 12% of axial strain

Commercial software VIC-3D, a digital image correlation (DIC) system, developed by Correlated Solutions Inc. was used to digitalize the photo images and to assimilate the images into 3D full-field displacements, as captured from the surface of the specimen. For the correlation analysis to be performed, VIC-3D requires the selection of an area of interest and a seed window at the first set of images. An area of interest is where displacements are quantified and a seed window is defined as the common pixels that are clearly identified in order to obtain an initial guess for the next images, on both left and right images as shown in Figure 2.6. A subset of 45 pixels and a step size of 3 pixels were selected to achieve as close to grain-scale resolution in the displacement measurement as possible.

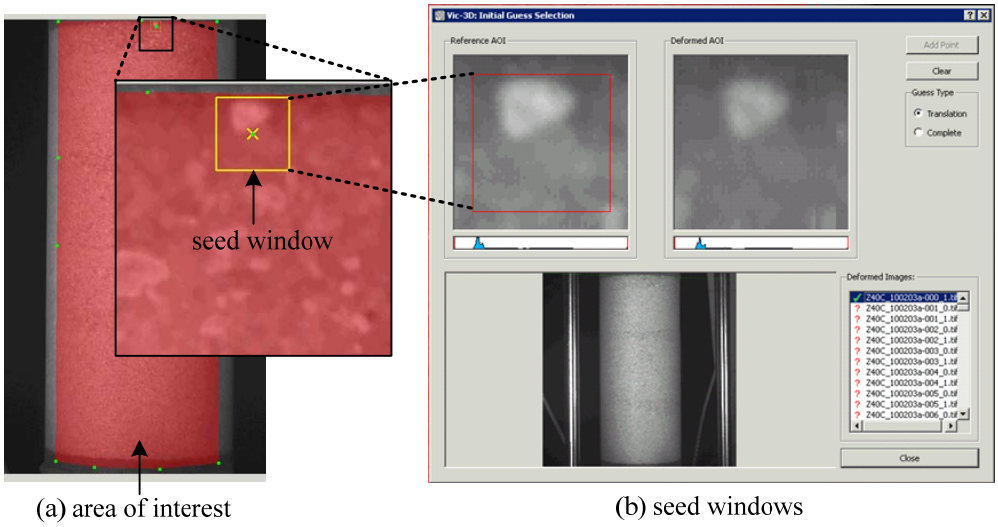

Figure 2. 6 Reference image (a) area of interest (b) seed windows (VIC-3D)

Once the 3D imaging system is calibrated and the reference image is prepared for analysis, VIC-3D can perform the 3D surface reconstruction. The common section captured by two cameras is where the displacement fields are analyzed which accounts for 40~50 mm horizontal width, which is equivalent to about one third of the circumstance of the specimen from the top view (Figure 2.7 (a) and (b)). VIC-3D generates 2D and 3D contour plots of the displacement fields available in the common section. The gray scale image of the 2D plot displays the lost data area while the color image displays the value of the current contour variable as well as the 3D plot. Horizontal displacement fields at 12% of axial strain for test 120904c are presented in 2D and 3D shapes Figure 2.7 (c).

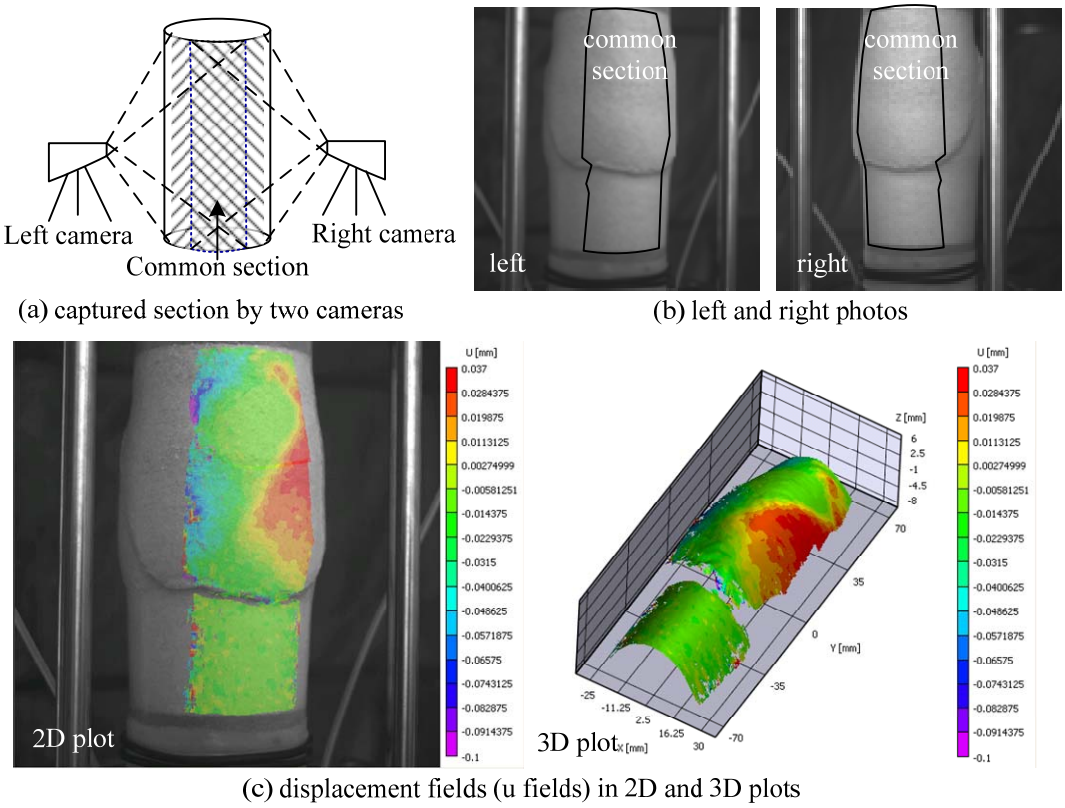

(a) captured section by two cameras

(b) left and right photos

(c) displacement fields (u fields) in 2D and 3D plots

Figure 2. 7 Common section captured by the VIC-3D two cameras system (a and b) and displacement fields in 2D and 3D shapes (c)

The tests recorded deformation data up to 12% of the axial strain, from which it was impossible to trace local deformations with respect to the undeformed state. To overcome this problem, the 3D-DIC system VIC-3D, updated the reference images for every 4th image, i.e. every 0.2% of axial strain, thus incremental displacements were computed. For example, Figure 2.8 illustrates the incremental displacement fields at 3.0% of axial strain when the reference image is the image at 2.8% of axial strain. The orientation of the system setup is described in a global Cartesian system, and u, v, and w are displacements corresponding to x, y, and z directions respectively. Then, in order to measure cumulative displacement fields and impose the finite element displacement

fields on digital images, it was required to develop a numerical integration of each sequential 3D-DIC. A detail description about this integration is presented later on this work.

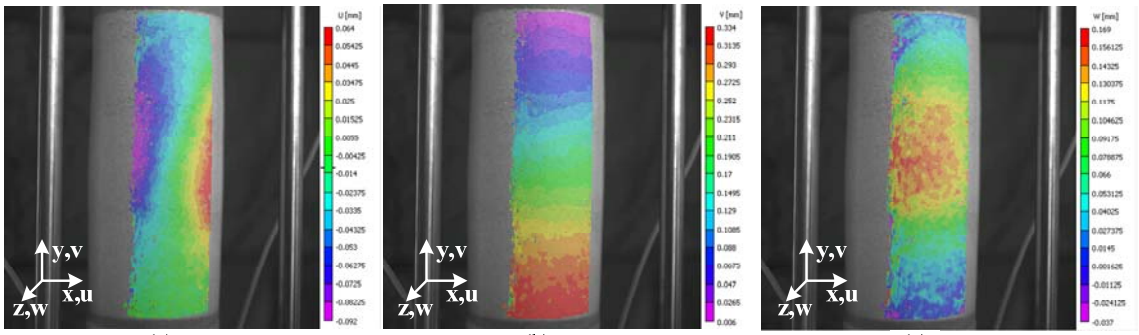

(a) (b) (c)

Figure 2. 8 Incremental displacement fields of test 120904c between 2.8% and 3.0% of axial strain, obtained by 3D-DIC process: (a) u field (b) v field (c) w field

The accuracy of accumulation approach of DIC data is validated by measuring vertical or horizontal displacements. Displacement of DIC data of a plane strain test are compared with the references measured by LVDT transducer and a bearing sled for vertical and horizontal movements, respectively (Chupin et al. 2011). Similarly, triaxial measurements were used as the reference when compared with displacements of digital images in Figure 2.9 (Medina-Cetina 2006). The vertical displacements were observed on the boundary with the bottom porous stone within the linear elastic domain. The difference between the reference and digital image correlation in vertical displacements results that the mean of the absolute error 0.00mm, with a standard deviation of 0.02mm, and the measurement accuracy is of the order of ±0.02mm. Previous research suggests

that the accuracy of the horizontal and out-of-plane displacements should be of the same order as the vertical displacements (Sutton et al. 2000).

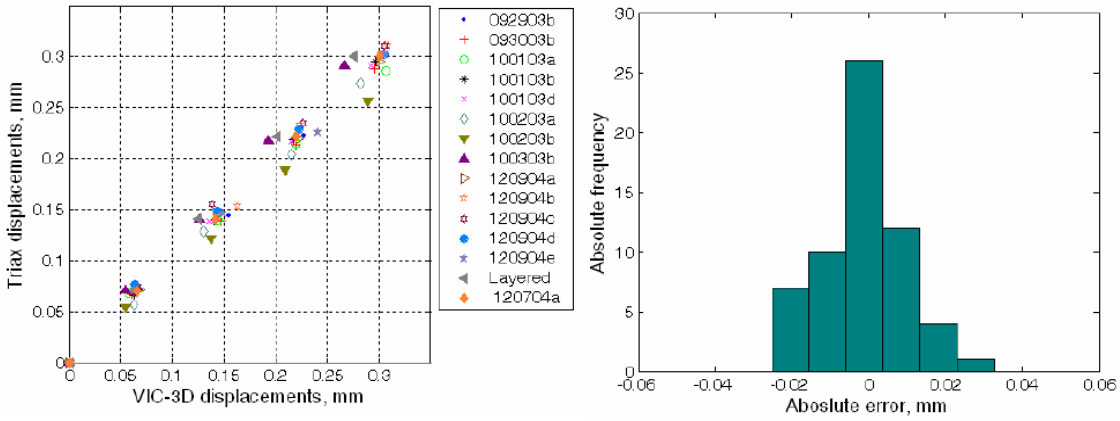

(a) Comparison of diaplacement measurements (b) Absolute error of displacement measurements

Figure 2. 9 Accuracy analysis: (a) comparison of displacement measurements between triaxial test system and VIC-3D (b) absolute frequency histogram of absolute error of displacement measurements between triaxial test system and VIC-3D (Medina-Cetina 2006)

2.2.2 Qualitative Assessment of Localization Effects

Shear band observations in laboratory tests have been reported by several authors (Desrues 1996; Desrues and Viggiani 2004; Rechenmacher 2006). Most of these investigations were obtained from specifically designed plane strain biaxial tests that are convenient to study strain localization. In a number of cases, it is known that failure surfaces take place along pre-existing discontinuities or the loss of homogeneity by the test execution and preparation. Medina-Cetina (2006) conducted a series of compression tests on triaxial sand specimens, with a 3D digital imaging system in order to detect and characterize similar localized effects. Different patterns can be identified for the triaxial axisymmetric tests, demonstrating the presence of a set of patterns, including both

bulging and shearing modes. Their variations are hypothesized to be caused by material heterogeneity. Another difference with 2D investigations is that the cylindrical samples have a curved surface and no designated discontinuities. These features make it difficult to identify the characteristics of a captured area before the sample reaches failure.

The deformed sample photos and corresponding incremental displacement fields between 11.8% and 12% of axial strain, in the x, y, and z directions captured by VIC-3D are presented in Figure 2.10 except for the test 120704b. The test 120704b (no.17) ends at 10% of axial strain, thus its photo and corresponding incremental displacement fields are estimated at 10% of axial strain (Figure 2.10). The numbers on the photos indicates the number of the test as mentioned in Table 2.1.

From these images, it is observed that a shearing mode consisting of two shear bands that cross each other and form a 'v' shape was found in thirteen tests. A bulging mode that constitutes a clear separation of the bottom segment appearing at the upper segment, expanding in the radial direction was observed in twelve tests. The defined section between the upper and bottom segments was made by development of shear bands and the crust of the upper segment tending slide along the shear failure surface. The layered specimen (no.18) showed a bulging mode on the loose upper segment indicating an exacerbated compressing behavior when compared with the other results, but no significant bulging was observed for the dense lower segment. The loose specimen (no.25) showed localization in terms of axial strain, but no shear bands.

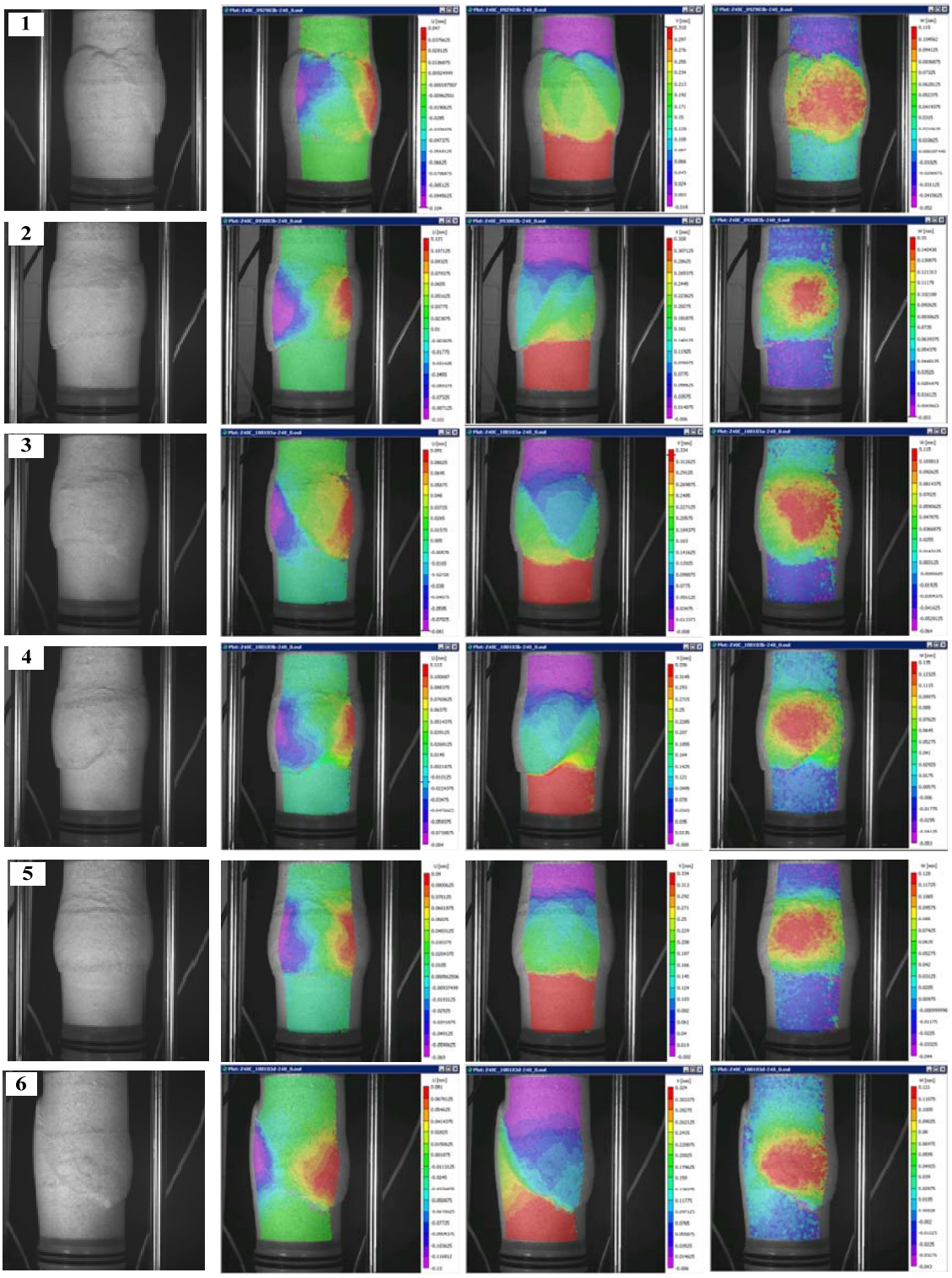

Figure 2. 10 Digital image and corresponding incremental displacement fields at 12% of axial strain (a) photo image (b) u field (c) v field (d) w field

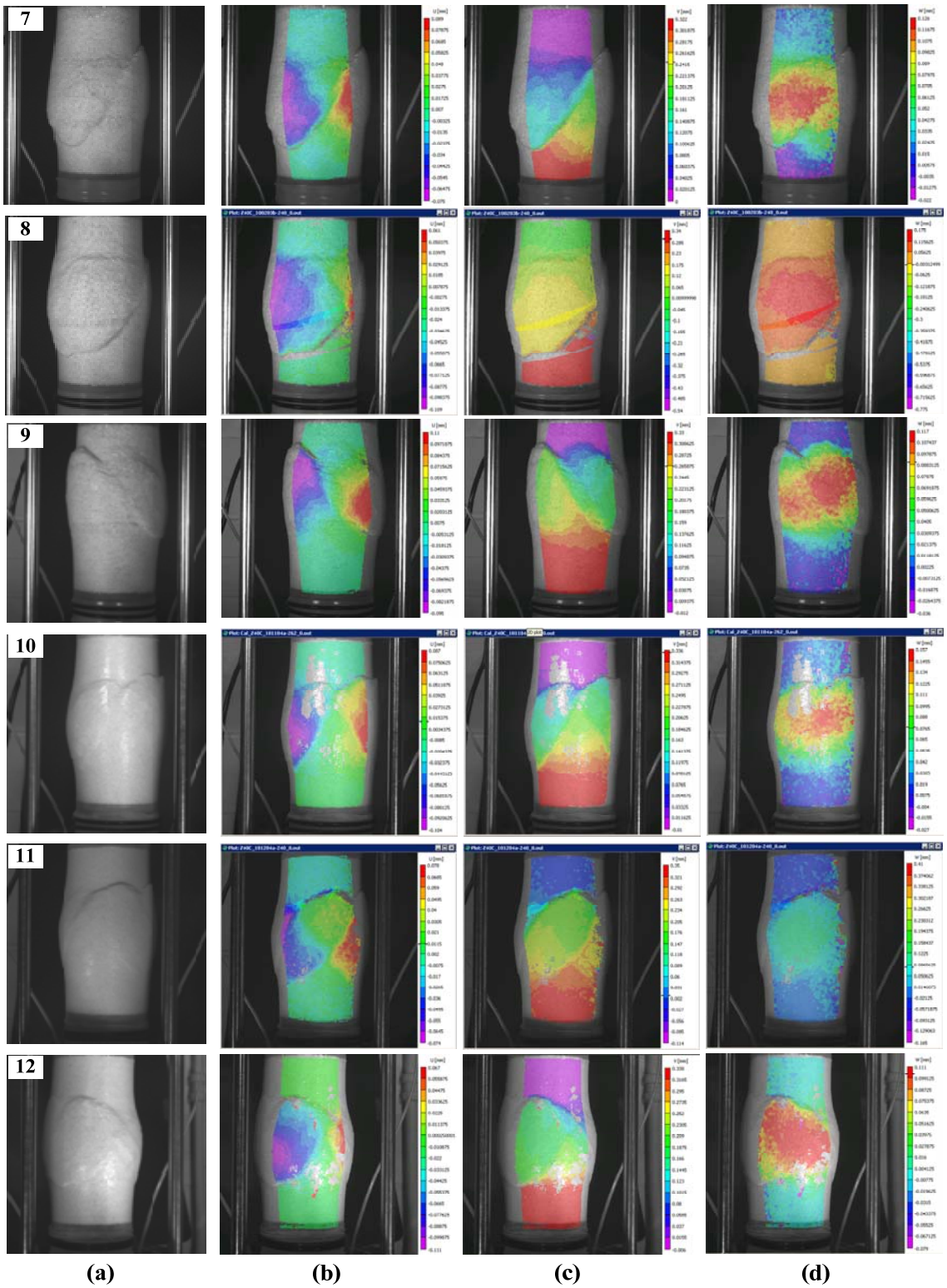

Figure 2. 10 continued

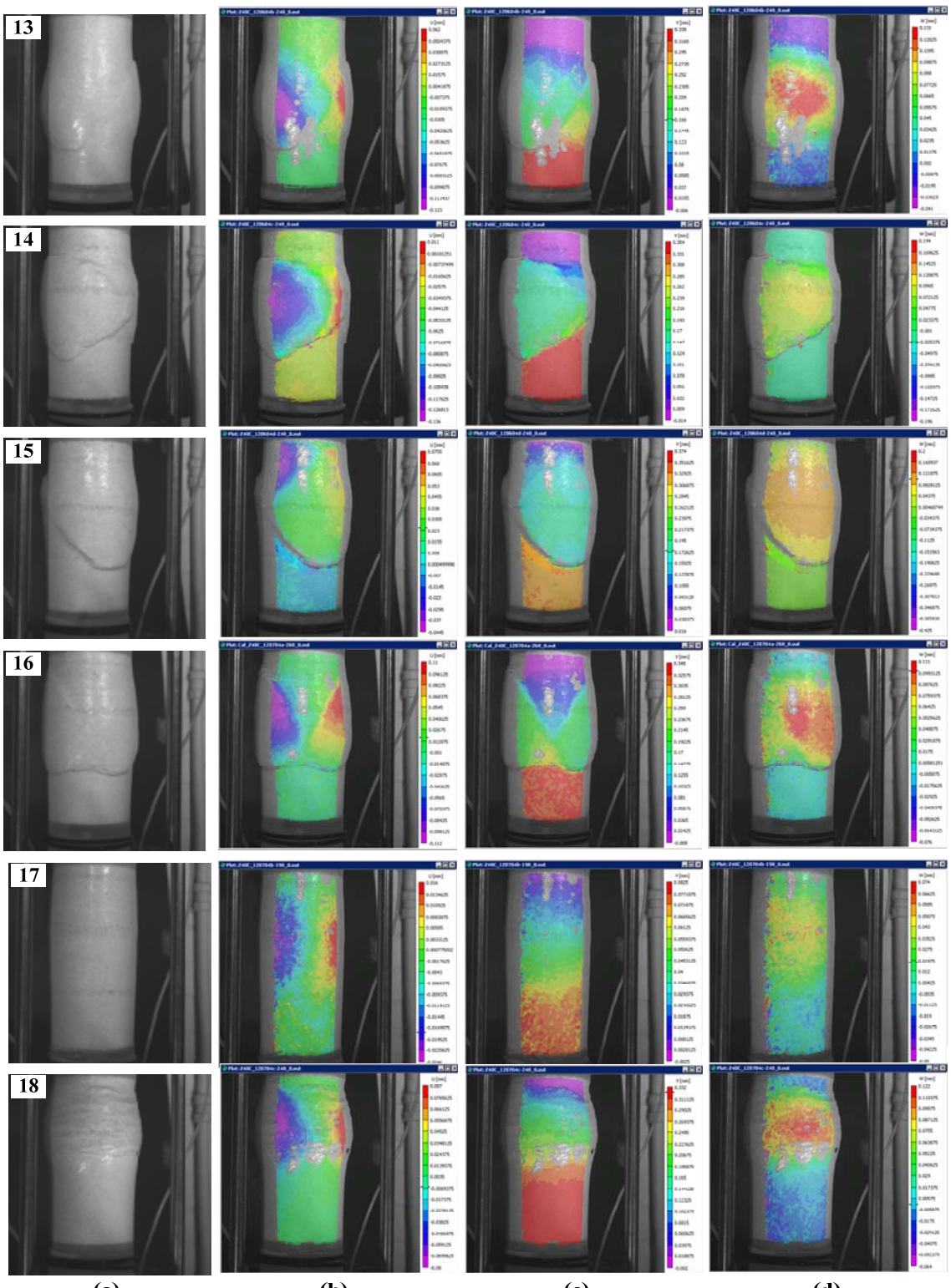

Figure 2. 10 continued

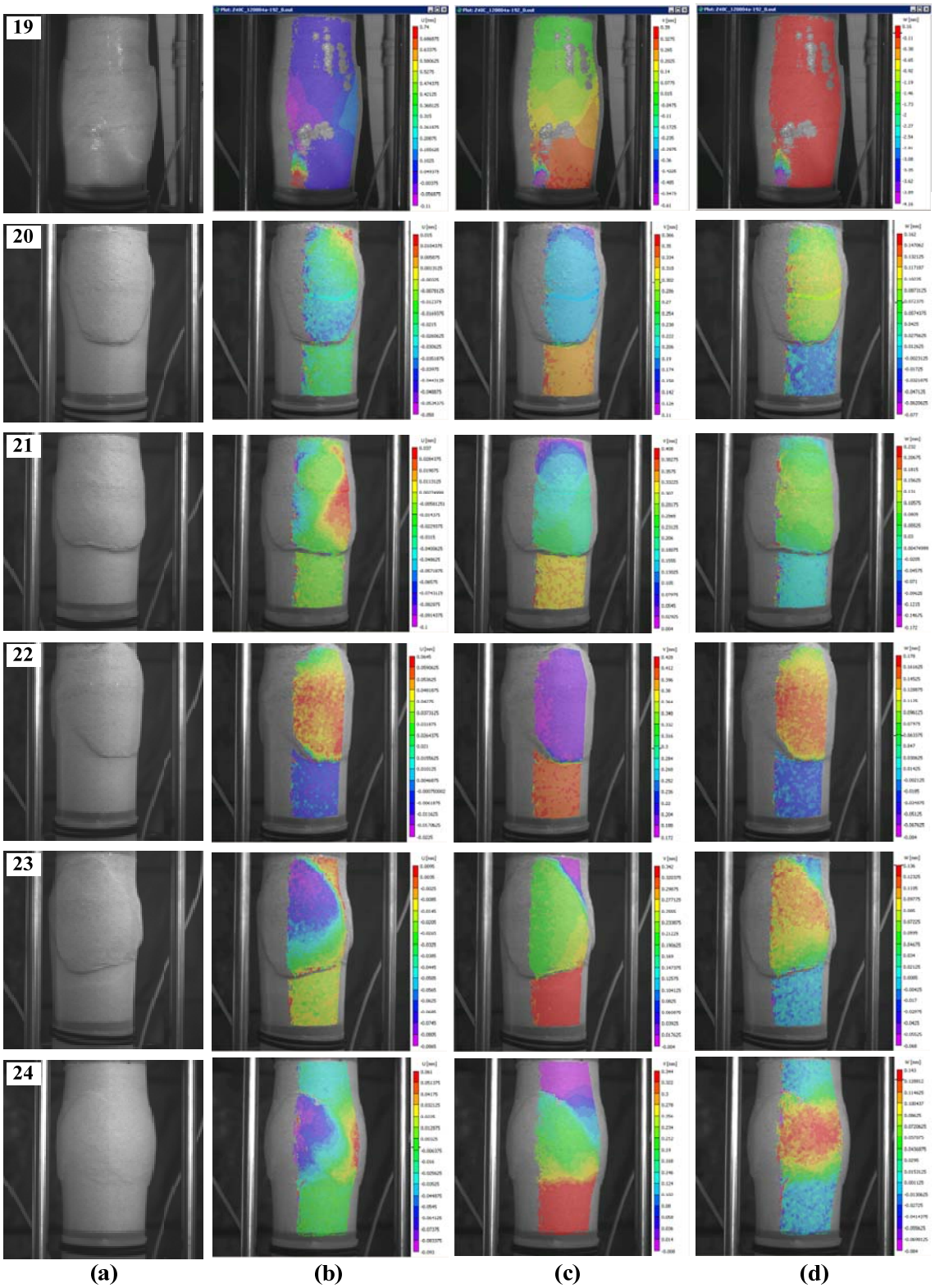

Figure 2. 10 continued

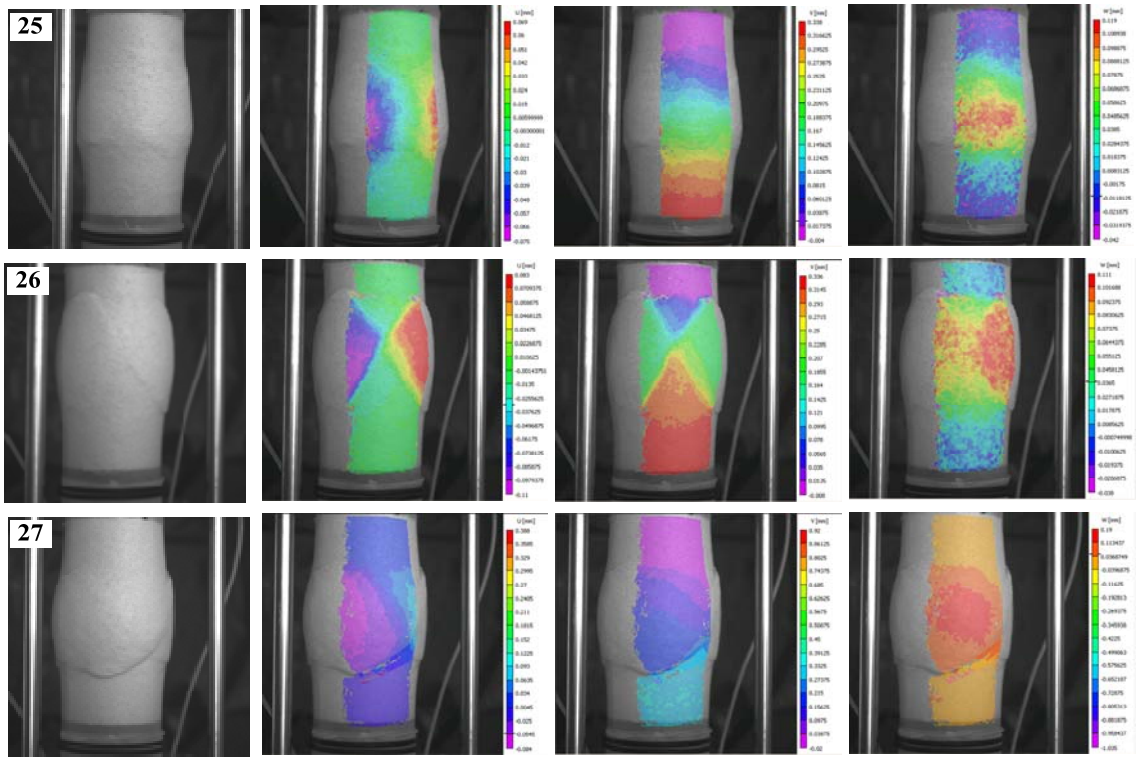

(a) (b) (c) (d)

Figure 2. 10 continued

3. 3D DIGITAL IMAGE TRANSFORMATIONS AND INTERPOLATION

3.1 Digital Image Corrections

A 3D-DIC system suffers from the accumulation of inherent error sources such as cross-camera matching, camera calibration, multiple correlation runs and triangulation when integrating segments of the displacement fields (Lava et al. 2011; Sutton et al. 2008). The image data is obtained from VIC-3D, which has already considered corrections for data alignment included in the calibration procedure. From the calibration images, various system parameters, including camera-based parameters such as focal length, image center, lens distortion and the relative orientation of the two cameras in space are computed. Still the plotted shape of the 3D image data on the Cartesian coordinate system seems to be slightly inclined, which was corroborated by analyzing the coefficients of the hyperplane equation fitted to the coordinates of the cloud of data points at the undeformed stage. The best fit plane is found by regression of all data points and it is very sensitive to the number, a shape and a placement of the collected image data. To correct for these deviations, a 3D geometric rotation and translation was conducted with the aim of starting the cumulative analysis of deformations with the best spatial data reference possible. A 3D geometrical transformation procedure includes the following steps: (1) the coefficients of an equation of a best fit plane are computed by regression of all data points, (2) the initial data points are rotated with the angles calculated from the relationship between a normal vector of a best fit plane and the y- and z-axes, (3) after rotations, the transformed data points are

translated in the y- and z-directions for imposing the data points into the physical coordinate system.

3.2 Assessment of the Trend Fitting Plane

The selected coordinate system introduced in VIC-3D is configured by a best fit plane. The best fit plane method imposes a best fit plane on the image data is used to calculate the transformation of data. In the case when a best fit plane is adopted, the origin of the best fit plane is located in the middle of the sample height in the x-y plane and inside of the sample in the z-direction, and the depth of the origin may vary in the z-direction due to the position of the two cameras. Thus, the physical coordinate system of a sample is determined to be different from the selected coordinate system of the analyzed image data. However, the image data points follow a best fit plane, so by controlling the best fit plane, 3D geometrical transformations can be conducted.

Since it was not possible to retrieve the VIC-3D equation of the best fit plane, this was found by regression of all the displacement data points. Exported data after digital image correlation analysis included coordinates of data points and the incremental displacements in the x-, y-, and z-directions with respect to the reference image. Coefficients of the trend fitting plane were computed by the code shown in Figure 3.1. The fitting plane had the form of $z=ax+by+c$, where a, b, and c are regression-type coefficients. For example, an equation of a fitting plane for the test 120904c was $z=0.00266x-0.00003y+0.00000$.

```
%<Part 1. Geometrical transformations>%%%%%%%%%%%%%%%%%%%%%%%%%%%%%%%%
clear all
fno1='Z40C_120904c-004';%change file name
fnam1=[fno1 '_0.csv'];
A=xlsread(fnam1);
A=A(~any(isnan(A),2),:);%remove NaN rows
A(A(:,1)==A(1,1),:)=[];%filter a repeated node
A=[A(:,1) A(:,2) A(:,3) A(:,7) A(:,8) A(:,9)];%save X,Y,Z,U,V,W
%a fitting plane%-----------------------------------------------------
const=ones(length(A),1);
coeff=[A(:,1) A(:,2) const]\A(:,3);%z=coeff(1)*x+coeff(2)*y+coeff(3)
```

Figure 3. 1 Code for finding an equation of a fitting plane

3.3 3D Geometrical Transformations

3.3.1 Rotation Analysis

A 3D geometrical transformation is a way to modify the current coordinates by translation, scaling, reflection, shearing, or rotation by the use of a matrix and vector systems. In this study, rotation and translation were used to improve the selected coordinate system.

The best fit plane obtained by regression of all data points was found to be not parallel to the x-y plane, and slightly inclined, because of the non-uniform distribution of data points generated after the 3D-DIC. In order to straighten the fitting plane to the x-y plane, data points must be rotated. The rotation angles are computed by the relationship between the normal vector of a fitting plane and the y- or z-axes. The normal vector, **n**,

of a fitting plane is induced from the coefficients of a fitting plane with a general form (a,b,-1). Note that a vector forms a right-handed system. A cross product of **n** and a unit vector of the z-direction is a vector, **m**.

$$\mathbf{m}=(0,0,1)\times(a,b,-1)=\begin{vmatrix} i & j & k \\ 0 & 0 & 1 \\ a & b & -1 \end{vmatrix}=-bi+aj=(-b,a,0)$$

The angle, φ, between a vector **m** and a unit vector in the y-direction is given by the following formula.

$$\varphi=\cos^{-1}\left(\frac{(-b,a,0)\bullet(0,1,0)}{\sqrt{a^2+b^2}}\right)=\cos^{-1}\left(\frac{a}{\sqrt{a^2+b^2}}\right)$$

The angle, θ, between a vector **n** and a unit vector of the negative z-direction is given by the following formula.

$$\theta=\cos^{-1}\left(\frac{(a,b,-1)\bullet(0,0,-1)}{\sqrt{a^2+b^2+1}}\right)=\cos^{-1}\left(\frac{1}{\sqrt{a^2+b^2+1}}\right)$$

The plane should be adjusted to be parallel to the x-y plane, thus the normal vector, **n**, rotates on the z-axis with an φ angle and becomes the transformed vector **n'**. The vector, **n'**, rotates on y-axis with a negative θ angle and becomes a vector **n"**. Data points follow a fitting plane with rotations of the normal vector, **n**, so that it straightens up with a fitting plane that is parallel to x-y plane. Figure 3.2 shows the rotation steps and normal vectors at each step in space and Figure 3.3 illustrates the rotation processes of data points. The transformation process in matrix form is coded based on the 3D rotation description of Foley et al. (1996), and the code is shown in Figure 3.4.

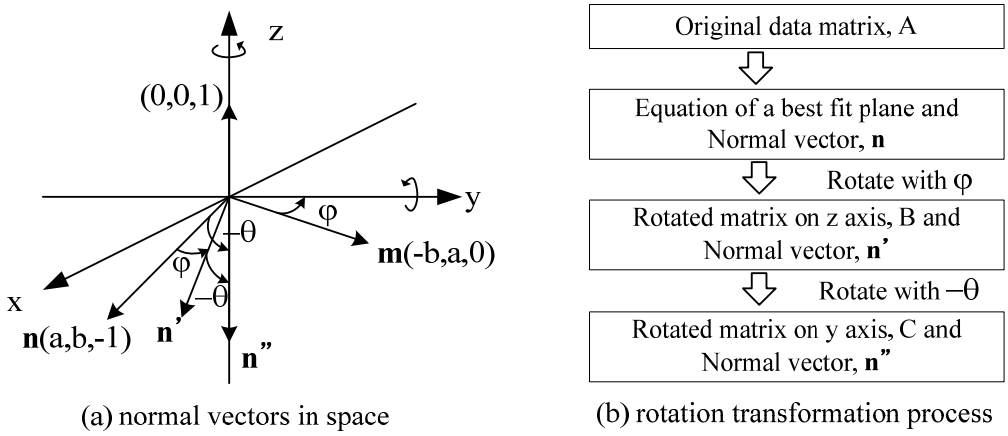

Figure 3. 2 3D geometrical transformation process (a) normal vectors in space (b) rotation process

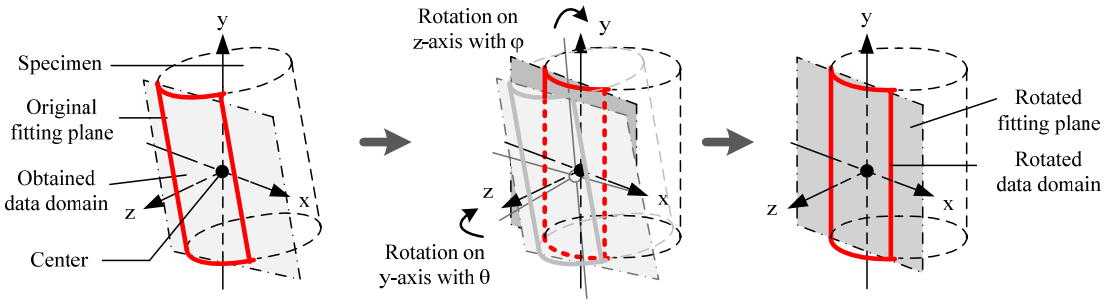

Figure 3. 3 Schematic view of 3D transformations: rotation

```
%Rotation on the z-axis
psi=acos(coeff(1)/sqrt((coeff(1)^2)+(coeff(2)^2)));
if coeff(2)<0%if coeff a>0,b<0, use(psi), a>0,b>0, use(-psi) for Rz
    Rz=[cos(psi) -sin(psi) 0 0 0 0;
        sin(psi) cos(psi) 0 0 0 0;
        0 0 1 0 0 0
        0 0 0 cos(psi) -sin(psi) 0
        0 0 0 sin(psi) cos(psi) 0
        0 0 0 0 0 1];
```

Figure 3. 4 Code for rotation process

```
else
    Rz=[cos(-psi) -sin(-psi) 0 0 0 0;
        sin(-psi) cos(-psi) 0 0 0 0;
        0 0 1 0 0 0
        0 0 0 cos(-psi) -sin(-psi) 0
        0 0 0 sin(-psi) cos(-psi) 0
        0 0 0 0 0 1];
end
B=Rz*A';
%Rotation on the y-axis
theta=acos(1/sqrt((coeff(1)^2)+(coeff(2)^2)+1^2));
Ry=[cos(-theta) 0 -sin(-theta) 0 0 0;
    0 1 0 0 0 0;
    sin(-theta) 0 cos(-theta) 0 0 0
    0 0 0 cos(-theta) 0 -sin(-theta);
    0 0 0 0 1 0;
    0 0 0 sin(-theta) 0 cos(-theta)];
C=Ry*B;
C=C';
```

Figure 3. 4 continued

To illustrate the proposed post-processing scheme, a simple case with 10 coordinate points is taken from the boundary of test 120904b. Results of the fitting plane and rotation of data points are shown in Figure 3.5. Blue data points and an inclined plane indicate the state before the rotations and red data points and a horizontal plane in the x-z view show the position after rotations. In the same way, this rotation process is applied to the test 120904b and the results are presented in Figure 3.6. Before rotations, the equation of the plane is z=0.00433x+0.00001y+0.00000 and after the

rotations, the equation of the plane of transformed data points changes to z=0.00011x+0.00000y+0.00000. This means that a fitting plane is changed to be parallel to the x-y plane and the coefficients of the plane, a and b, become closer to zero, indicating a proper coordinate transformation.

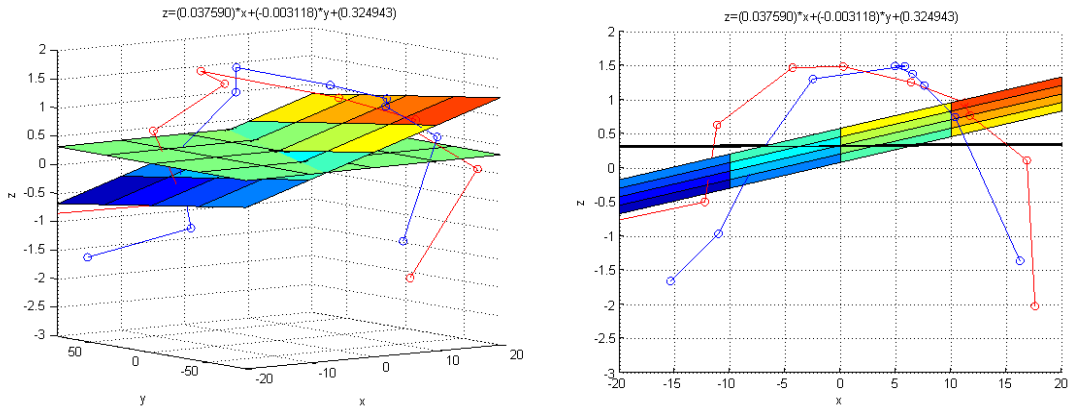

(a) xyz view (b) x-z view

Figure 3. 5 Geometrical transformation of 10 data points (a) xyz view (b) x-z view

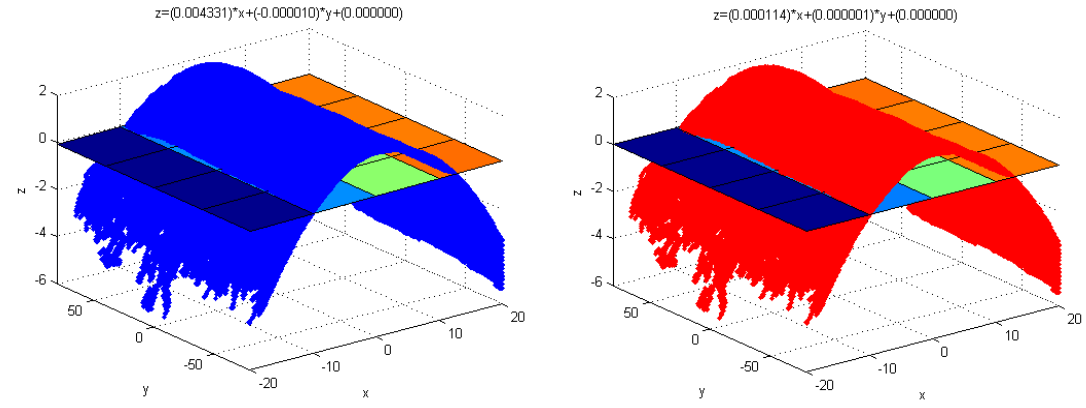

(a) before rotation (b) after rotation

Figure 3. 6 Geometrical transformation of test 120904b (a) before rotations (b) after rotations

3.3.2 Translation Analysis

After the 3D-DIC pre- and post- processing is completed, the origin of the data points is set up inside and mid-height of a sample. In the physical coordinate system, the bottom of a specimen is assumed to be the x-z plane with y=0 and the center axis of a sample coincides with the y-axis, which means that all data points must move up (y-direction) and forward (z-direction) to impose displacement fields on a finite element model. The data points are translated to the new coordinate system by adding translation amounts to the current coordinates of the points. All data points are moved by 'yb' and 'z_add'. 'yb' is the distance in the y-direction from the bottom to the center and it is decided by reading of bottom coordinates from the first digital image of the undeformed state. 'z_add' is the distance in the z-direction from the center of a specimen to the best fit plane and it is calculated by subtracting 'z_avg' from the measured radius presented in Table 2.1. 'z_avg is an averaged value, taken from the data points with the threshold between -0.02 mm and 0.02 mm of x because 'z_avg' is theoretically the z value when x is equal to zero, but real data is scarcely at the position of exact x=0. Figure 3.7 and 3.8 illustrate how to find 'yb' and 'z_add' and the translation process. Code in Figure 3.9 explains how to compute 'z_add' and shows the translation matrix.

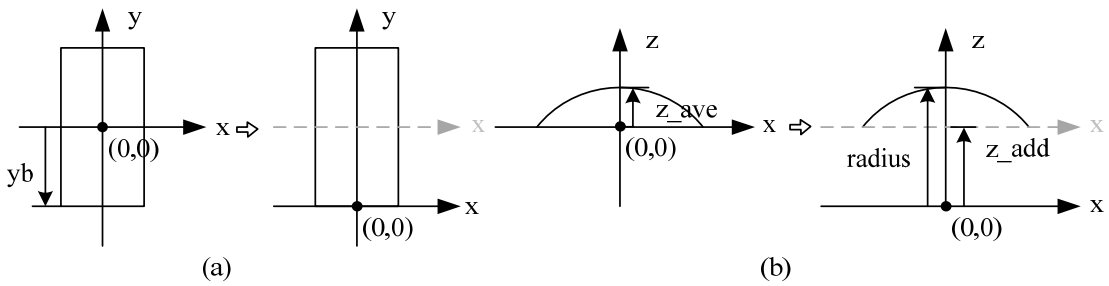

Figure 3. 7 Translation on y- and z- directions (a) y-direction translation (b) z-direction translation

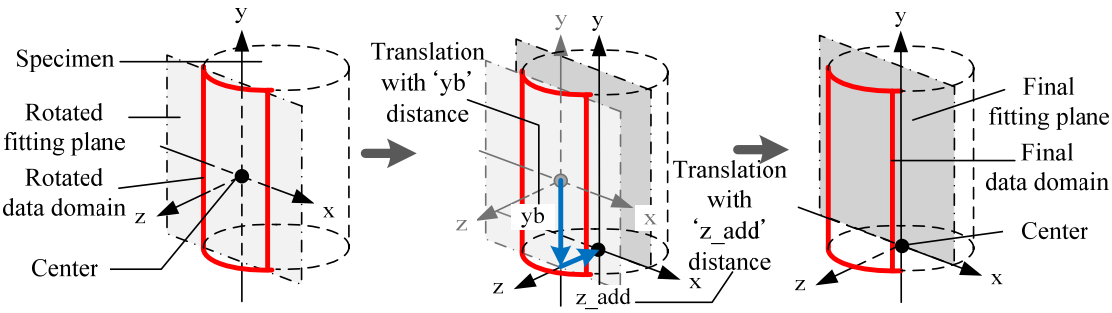

Figure 3. 8 Schematic view of 3D transformations: translation

```
%Translation y- and z- directions ----------------------------------
%yb from 'Reference_coordinates.xls': check minY, maxY, and height
yb=-78.6352;
%radius from 'DIA_SummaryAnlayses.xls' Data Summary sheet
radius=35.55;
row=find(-0.02<=C(:,1)&C(:,1)<=0.02);%threshold -0.02<=x<=0.02
S=C(row,:);
z_ave=mean(S(:,3));
z_add=radius-z_ave;
Tyz=repmat([0 -yb z_add 0 0 0],length(A),1);
D=C+Tyz;
```

Figure 3. 9 Code for translation in y- and z-directions

Figure 3.10 is an example of a completed translation. The range of y varies between 0 to 158cm and the maximum z value corresponds to the radius of the test 120904b.

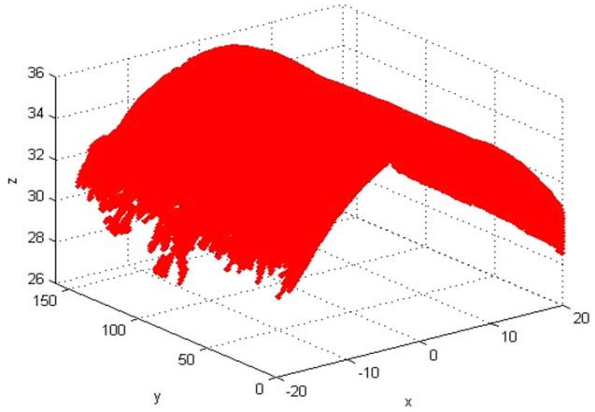

Figure 3. 10 Result of test 120904b after translation on y- and z- directions

3.3.3 Trend Fitting Plane Coefficients and Rotation Analysis

Figure 3.11 shows a snapshot image of the raw coordinate's data, and the fitting plane plots in the x-z plane for test 120904c. It was observed that in general, plots before and after rotations did not show a significant difference. To investigate the effects of rotation angles, plane coefficients and rotation angles from each fitting plane, results of the coordinate transformation are presented in Table 3.1 and Figure 3.12.

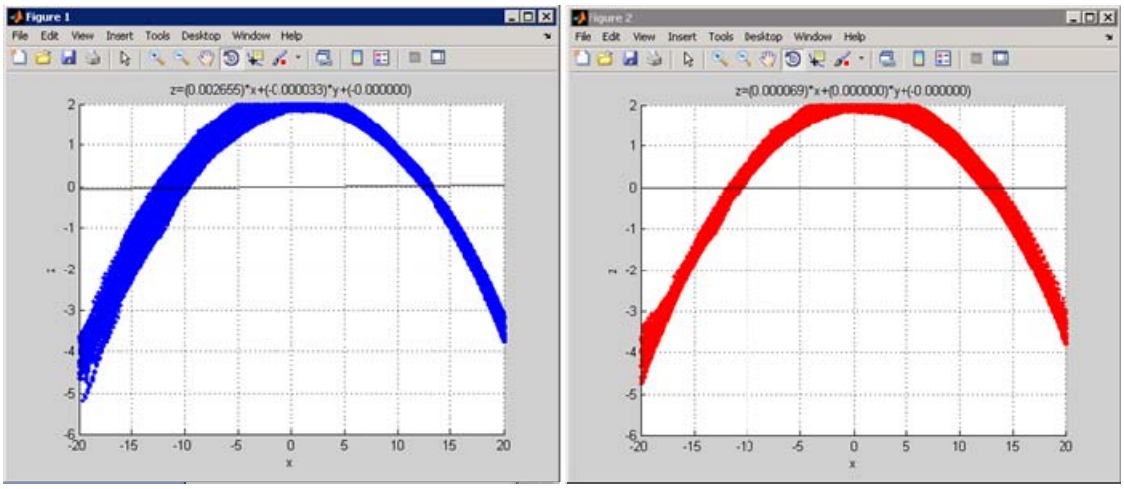

(a) before rotation (b) after rotation

Figure 3. 11 Data plots and a fitting plane in x-z plane for test 120904c (a) before rotation (b) after rotation

The rotation angle in the z-direction, φ, oscilated between 0 and 4.25° and ten tests out of twenty seven tests showed more than 1° of φ. The rotation angle in the y-direction, θ, is less than 1° for all tests. Therefore, it can be concluded that the effects of the rotation angles are not significant, and that the axis translation process would be enough, before computing the total displacements. This corroborates that the internal VIC-3D plane view adjustment of the coordinates is within a reasonable degree of accuracy.

Table 3. 1 Plane coefficients and rotation angle analysis (plane equation: z=ax+bx+c)

Case		Plane Coefficients			Angle (deg)	
No.	**Test Name**	**a**	**b**	**c**	**φ**	**θ**
1	092903b	0.00623	-0.00008	0	0.76292	0.35715
2	093003b	-0.00594	-0.00012	-0.00002	1.15811	0.34017
3	100103a	-0.00188	-0.00010	0.00003	2.91701	0.10809
4	100103b	-0.00682	-0.00026	-0.00073	2.20098	0.39087
5	100103c	-0.00643	-0.00007	0	0.58772	0.36866
6	100103d	-0.00914	-0.00016	0	0.98398	0.52380
7	100203a	-0.00887	-0.00012	0	0.78146	0.50830
8	100203b	-0.00730	-0.00018	0	1.39622	0.41855
9	100303b	-0.00449	0.00000	0	0.00000	0.25697
10	101104a	-0.01320	-0.00024	0	1.05866	0.75662
11	101204a	-0.01627	0.00013	0	0.44021	0.93209
12	120604a	0.00698	-0.00006	0	0.50049	0.40011
13	120604b	0.00652	-0.00001	0	0.05273	0.37356
14	120604c	0.00759	-0.00007	0	0.49821	0.43488
15	120604d	0.00765	0.00005	0	0.38222	0.43803
16	120704a	0.00427	-0.00006	0	0.84489	0.24479
17	120704b	0.00590	-0.00010	0	0.92279	0.33797
18	120704c	0.00541	-0.00010	0	1.02681	0.31013
19	120904a	0.00561	-0.00006	0	0.59245	0.32139
20	120904b	0.00433	-0.00001	0	0.13229	0.24815
21	120904c	0.00266	-0.00003	0	0.71211	0.15213
22	120904d	0.00267	0.00000	0	0.08584	0.15298

Table 3. 2 continued

Case		Plane Coefficients			Angle (deg)	
No.	**Test Name**	**a**	**b**	**c**	**φ**	**θ**
23	120904e	-0.00326	0.00017	0.04187	3.05522	0.18705
24	121304a	0.00230	-0.00014	0	3.56545	0.13175
25	121304b	0.00405	-0.00013	0	1.84031	0.23194
26	121304c	0.00188	-0.00014	0	4.25209	0.10819
27	121304d	0.00254	-0.00001	0	0.24833	0.14542

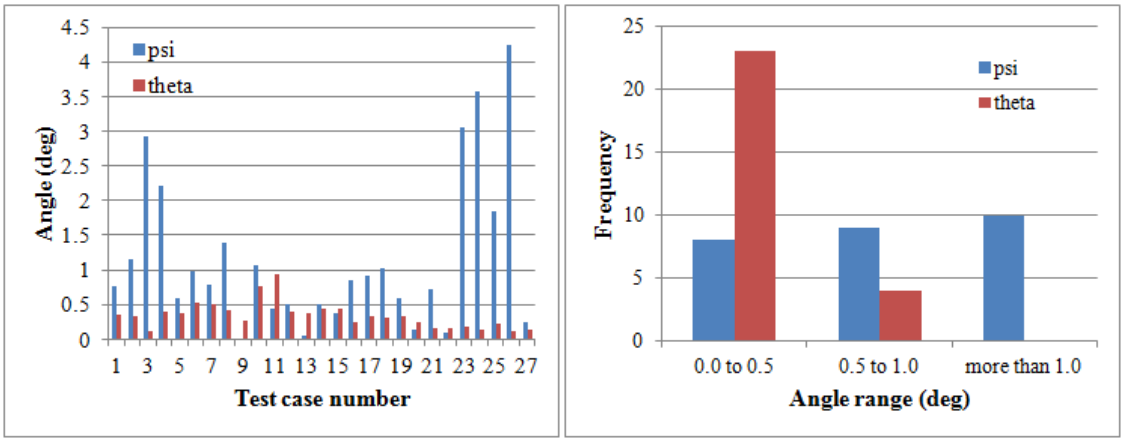

(a) (b)

Figure 3. 12 Rotation angle analysis (a) rotation angles of each test (b) frequency histogram of rotation angle

3.4 Interpolation of Image Data

3.4.1 Interpolation and Extrapolation for Cumulative Displacement Fields

Displacements are computed by comparing the position of a data point between the reference image and consecutive images. However, if a data point is out of the area

which is available to capture data points by the cameras, displacements are no longer acquired. For that reason, the 3D-DIC system updated the reference images for every 4th image, and consequently the coordinates of each sequence of image deformation do not correspond to each other (i.e. every segment of analysis is independent of each other). Interpolation and extrapolation of reference image data is therefore the key to elicit cumulative displacement fields with respect to the first reference image (undeformed state at zero strain).

Figure 3.13 illustrates the interpolation and extrapolation flow chart analysis as applied from image no.000 to image no.008, which corresponds to 0.4% of axial strain. The reference image for the no.000-004 image set is image no.000, but for the no.004-008 image set, the reference image is now image no.004. The reference image of the no.004-008 image set is extrapolated on designated grid points. Extrapolated displacements on this grid required to be updated from the previous node position. The displacement from the initial position of nodes of image no.000 to the final position of no.008 becomes the cumulative displacement of image no.008. Figure 3.14 shows actual image data movements by the interpolation and extrapolation in the data subsample corresponds to the center of the specimen, close to x=0, y=80mm. Cumulative total displacement fields of the undeformed state (image no.000) and deformed state (image no.008) at 0.4% of axial strain are shown in Figure 3.15.

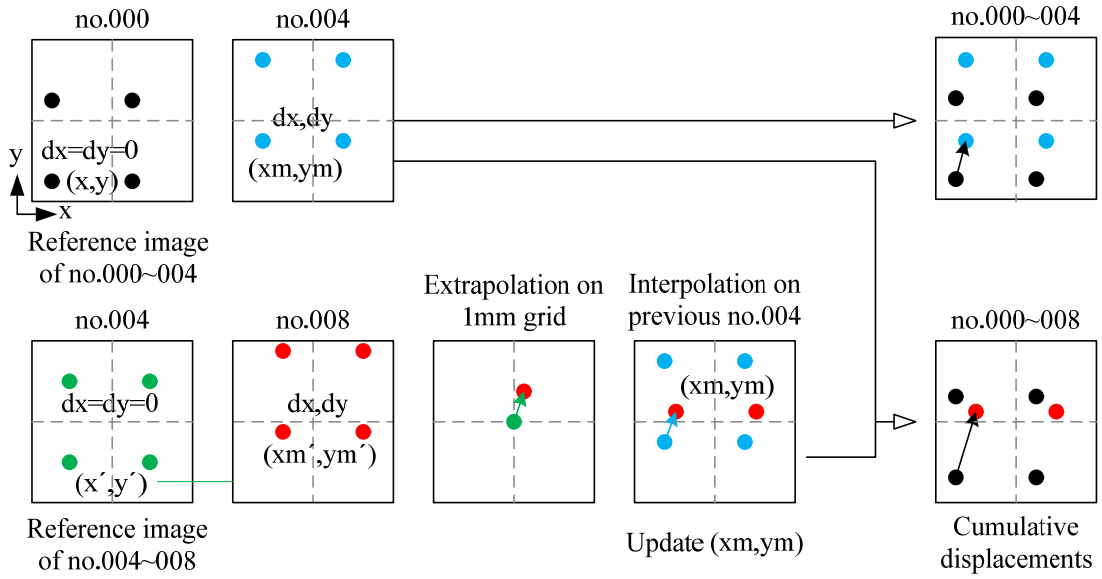

Figure 3. 13 Scheme of interpolation and extrapolation

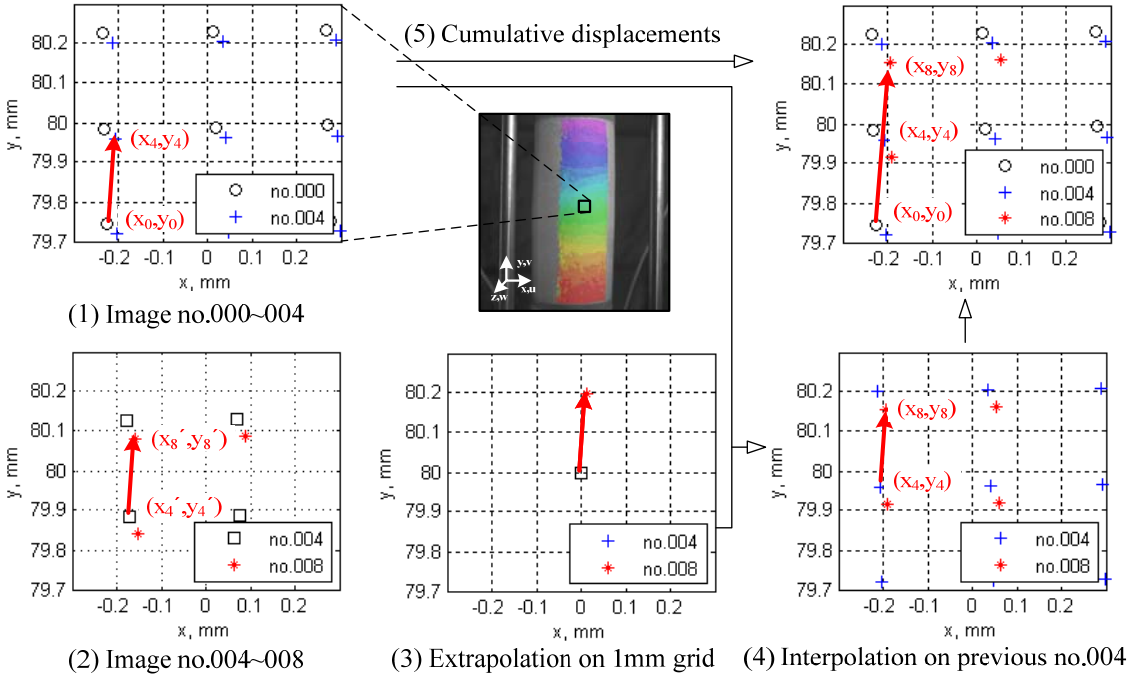

Figure 3. 14 Interpolation and extrapolation between image no.000 and no.008 (0.4% of axial strain)

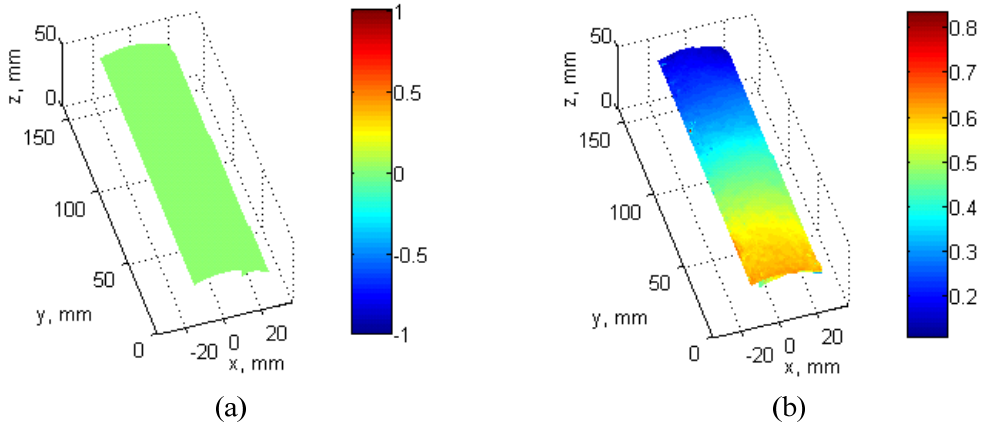

Figure 3. 15 Total displacement fields of test 120904c (a) undeformed state (b) deformed state at 0.4% of axial strain

3.4.2 Interpolation for Ccorrection of Incorrect Image Data

As illustrated in Figure 2.10, light reflection causes missing data points or incorrect assessment of displacement values because the 3D digital image system could not recognize pixels in that area, even within a short deformation range. Also, an excessive gap produced between bulging zone and a bottom block by shearing plane brings incorrect **w** displacement fields. During a compression loading, some sand particles stuck between a membrane and other soil particles show no movement in the vertical direction which could contribute to incorrect data points. Figure 3.16 is an example where it is required to solve a light reflection problem by an interpolation method using contiguous data points to the missing data zone. Another example of a similar problem is presented in Figure 3.17, where a gap occurred by shearing and radial displacement plots generated a poor displacement recognition by VIC-3D. In cases like these, raw data points are replaced with interpolated data points, conditioned by

contiguous data points near the gap. Improved displacement field assessment is presented on Figure 3.16 (c) and 3.17 (c) respectively.

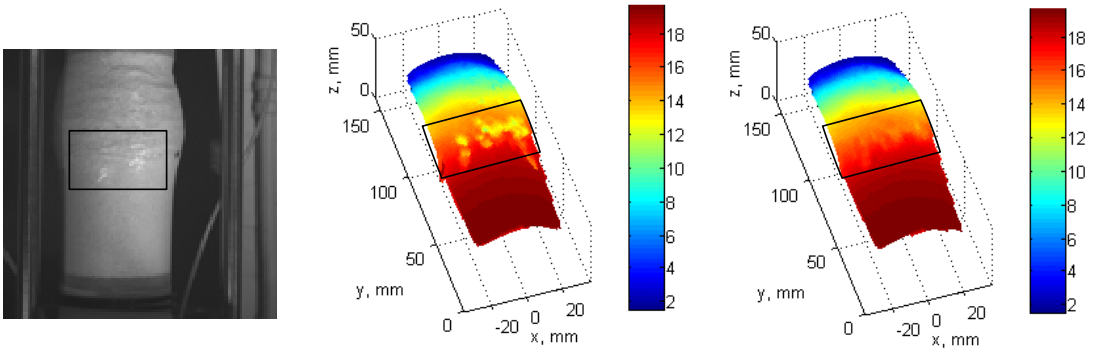

(a) photo image (b) incorrect data due to light reflection (c) corrected data by interpolation

Figure 3. 16 Correction of light reflection problem for test 120704c

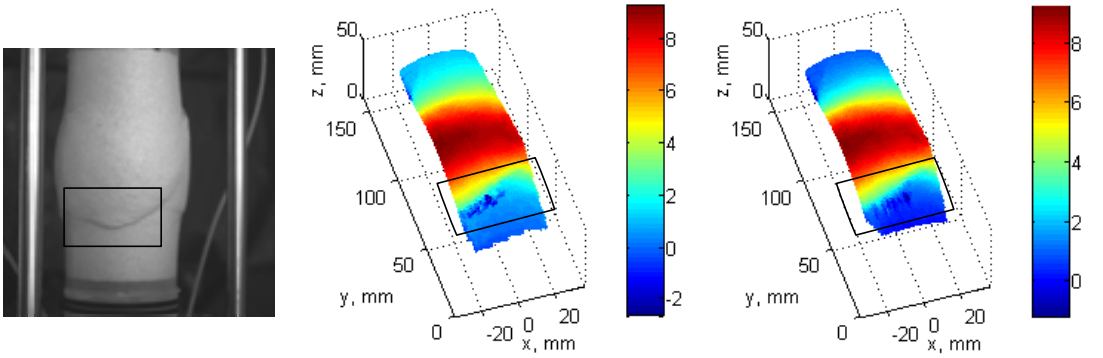

(a) photo image (b) incorrect data by shearing plane (c) corrected plot by interpolation

Figure 3. 17 Correction of incorrect data generated by shearing plane for test 121304d

3.5 Cumulative Displacement Fields

Cumulative radial and vertical displacement fields at 0.2%, 3.6%, 7% and 12% of axial strain after the 3D-DIC analyses are presented in Figure 3.18 and 3.19 respectively. Figure 3.18 illustrates the horizontal, vertical, and out-of-plane

displacement fields (**u**, **v**, and **w** fields) in Cartesian coordinates. Horizontal displacement fields show a developing persistent shear band clearly from 3.6% of axial strain. Vertical displacement fields at the bottom of the specimen correspond to global displacement, which follows displacement loading rate with 0.2% of axial strain/min. The out-of-plane displacement fields show a bulging zone that becomes evident after 3.6% of axial strain.

Radial displacement fields mainly represent the bulging effect of the specimen, which shows higher displacement values around the mid height of the sample. Notice that the vertical displacements at the bottom of the specimen correspond to the global displacement that follows the strain rate during shearing. After peak, Figure 3.19 (d) shows a clear distinction of displacement fields between the bottom segment and the rest of the specimen. This can be interpreted as a separated portion of the sample moving as a block.

Figure 3.20 (a) shows the average of the radial displacement across the same heights over the surface of the sample. This is symmetric with respect to the midpoint of the boundary at strain levels between 0.2% and 3.6% of axial strain, but definitely not after 7% of axial strain. This observation is expected, due to the shear plane that developed in the specimen after the peak stress. The shear band seen in Figure 3.19 (d) can also be seen by observing the displacement fields shown in Figure 3.19 (d). Unlike the displacements in the radial direction, the vertical displacements are distributed linearly at 0.2% and 3.6% of axial strain, but they become non-homogeneous after the peak. This change in the distribution confirms the presence of a shear plane in the sample. Based on the observed results, the bottom segment of the specimen is separated from the bulging surface of the specimen by shearing, and then it moves independently as a single block.

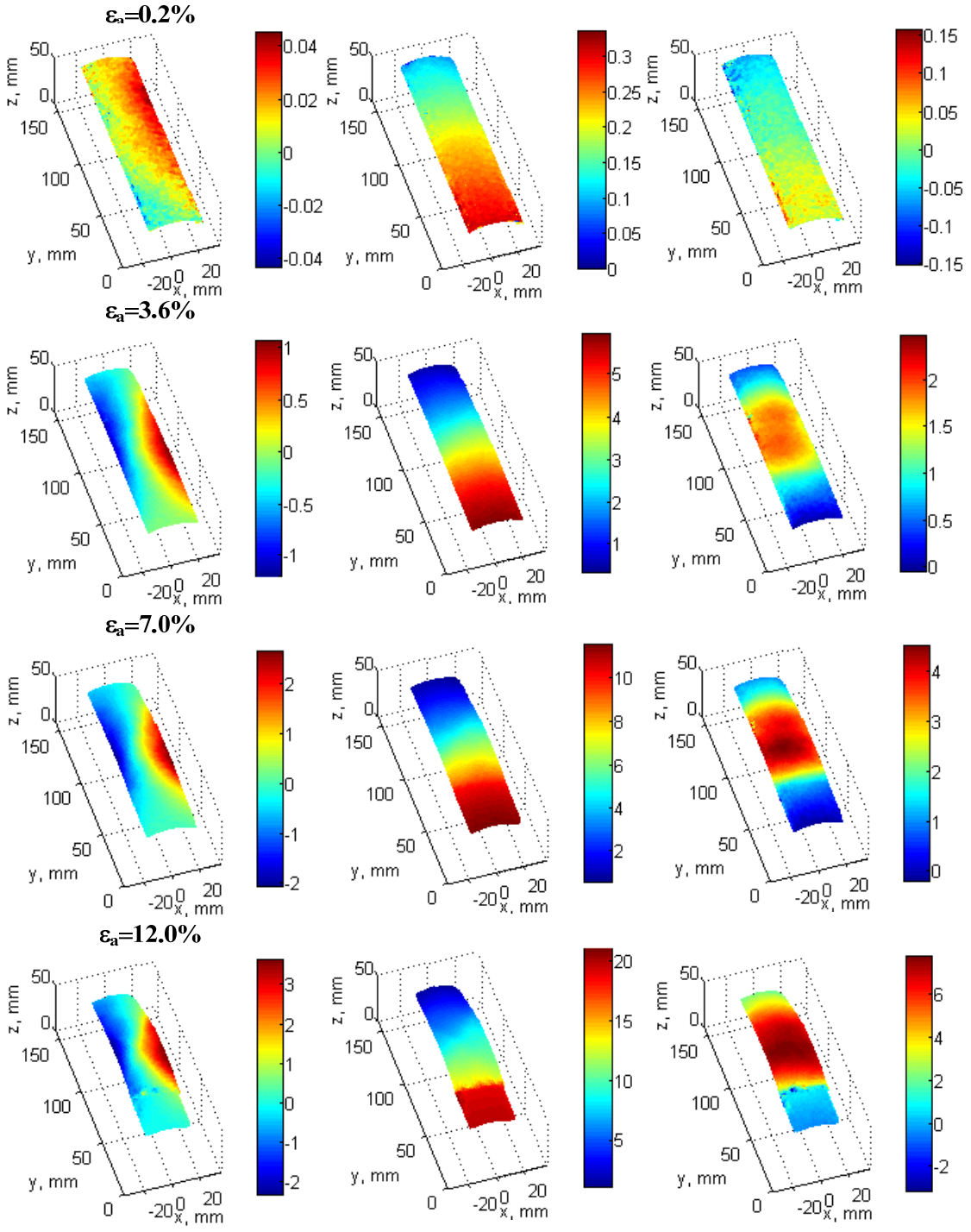

Figure 3. 18 Cumulative displacement fields of test 120904c in Cartesian coordinate system at 0.2%, 3.6%, 7%, and 12% of axial strain: (a) horizontal (u) displacement field (b) vertical (v) displacement field (c) out-of-plane (w) displacement field

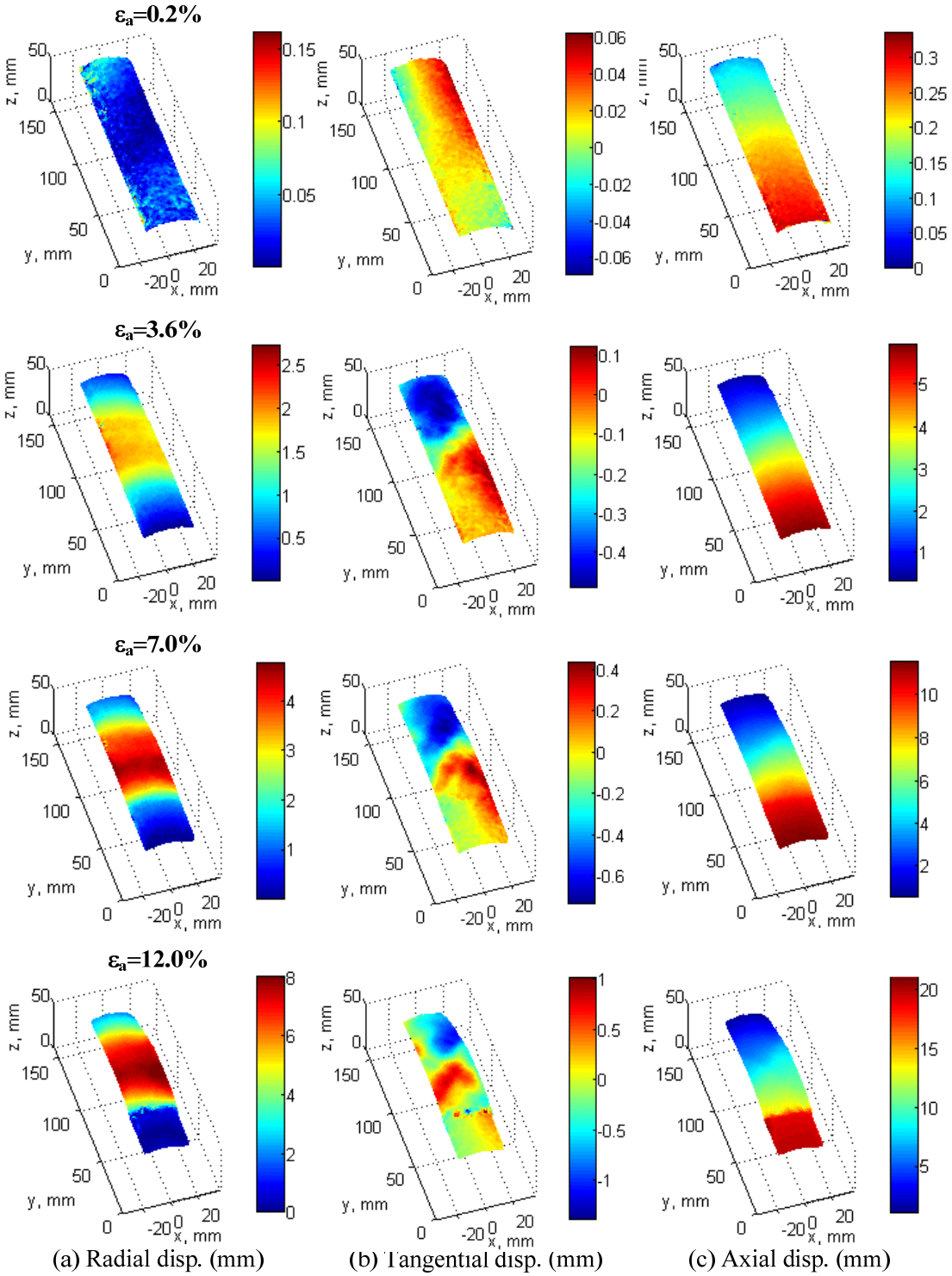

Figure 3. 19 Cumulative displacement fields of test 120904c in cylindrical coordinate system at 0.2%, 3.6%, 7%, and 12% of axial strain: (a) radial displacement field (b) tangential displacement field (c) axial displacement field

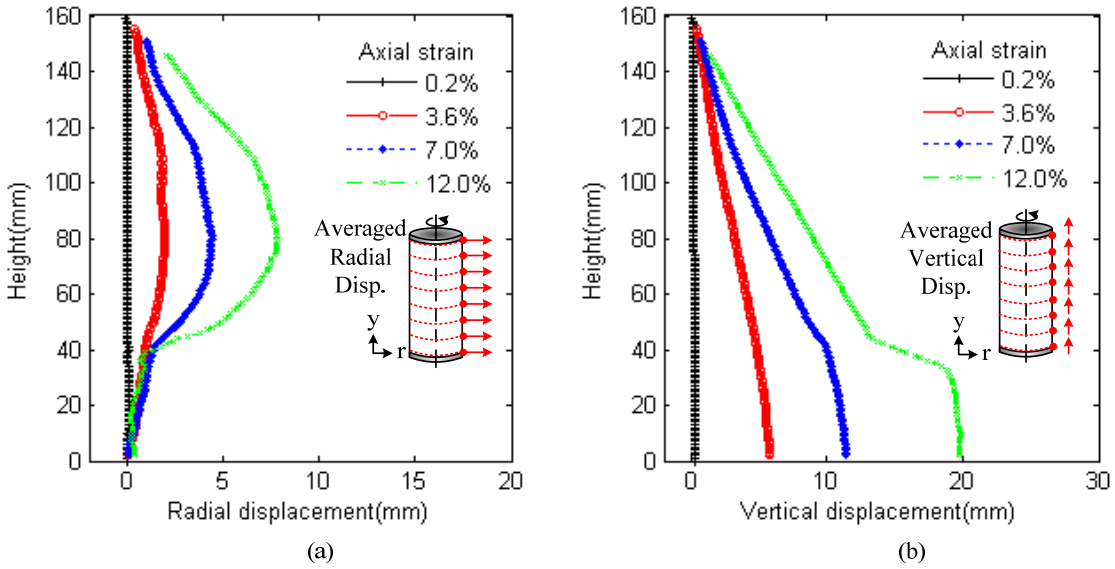

Figure 3. 20 Averaged displacements of test 120904c (a) radial displacement (b) vertical displacement

Cylindrical displacements, radial and tangential displacements, are computed from standard VIC-3D **u**, **v**, and **w** displacement fields in Cartesian coordinates. Radial and tangential displacements are calculated by the angles determined from the relationship between x and z or dx (i.e. **u**) and dz (i.e. **w**) as well as **u** and **w** displacements. A graphical explanation about the calculation of cylindrical displacements is presented in Figure 3.21.

$$\theta = \begin{cases} \tan^{-1}\left(\frac{z}{x}\right) & \text{if } x>0 \\ \tan^{-1}\left(\frac{z}{x}\right)+\pi & \text{if } x<0 \text{ and } z \geq 0 \\ \tan^{-1}\left(\frac{z}{x}\right)-\pi & \text{if } x<0 \text{ and } z < 0 \\ \frac{\pi}{2} & \text{if } x=0 \text{ and } z>0 \\ -\frac{\pi}{2} & \text{if } x=0 \text{ and } z<0 \\ 0 & \text{if } x=0 \text{ and } z=0 \end{cases}, \quad d\theta = \begin{cases} \tan^{-1}\left(\frac{dz}{dx}\right) & \text{if } dx>0 \\ \tan^{-1}\left(\frac{dz}{dx}\right)+\pi & \text{if } dx<0 \text{ and } dz \geq 0 \\ \tan^{-1}\left(\frac{dz}{dx}\right)-\pi & \text{if } dx<0 \text{ and } dz < 0 \\ \frac{\pi}{2} & \text{if } dx=0 \text{ and } dz>0 \\ -\frac{\pi}{2} & \text{if } dx=0 \text{ and } dz<0 \\ 0 & \text{if } dx=0 \text{ and } dz=0 \end{cases}$$

$dr_i = \sqrt{dx_i^2+dz_i^2} \times \cos(\theta_i - d\theta_i)$: radial displacement

$dt_i = \sqrt{dx_i^2+dz_i^2} \times \sin(\theta_i - d\theta_i)$: tangential displacement

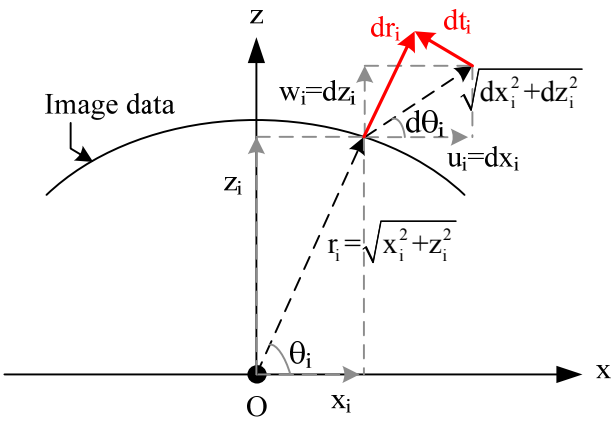

Figure 3. 21 Conversion between Cartesian and cylindrical coordinate systems

3.6 Cumulative Strain Fields

The cumulative strain fields are derived from the cumulative displacements fields in the same way as computing the cumulative displacements using strain-displacement relationships. Assuming small or infinitesimal strains, shear strain components for three dimensional cases (Desai and Siriwardane 1984; Iskander 2010) are expressed as

$$\varepsilon_x = \varepsilon_{11} = \frac{\partial u}{\partial x}$$

$$\varepsilon_y = \varepsilon_{22} = \frac{\partial v}{\partial y}$$

$$\varepsilon_{xy} = \varepsilon_{12} = \frac{1}{2}\left(\frac{\partial u}{\partial y} + \frac{\partial v}{\partial x}\right)$$

Above, ε represents a local strain field, with the x-axis direction, ε_{11}, and the y-axis direction, ε_{22}. Horizontal and vertical displacement fields in plane are represented with u and v. Shear bands are coaxially crossed from the peak stress, which can be observed at 7% and 12% of axial strain in Figure 3.22.

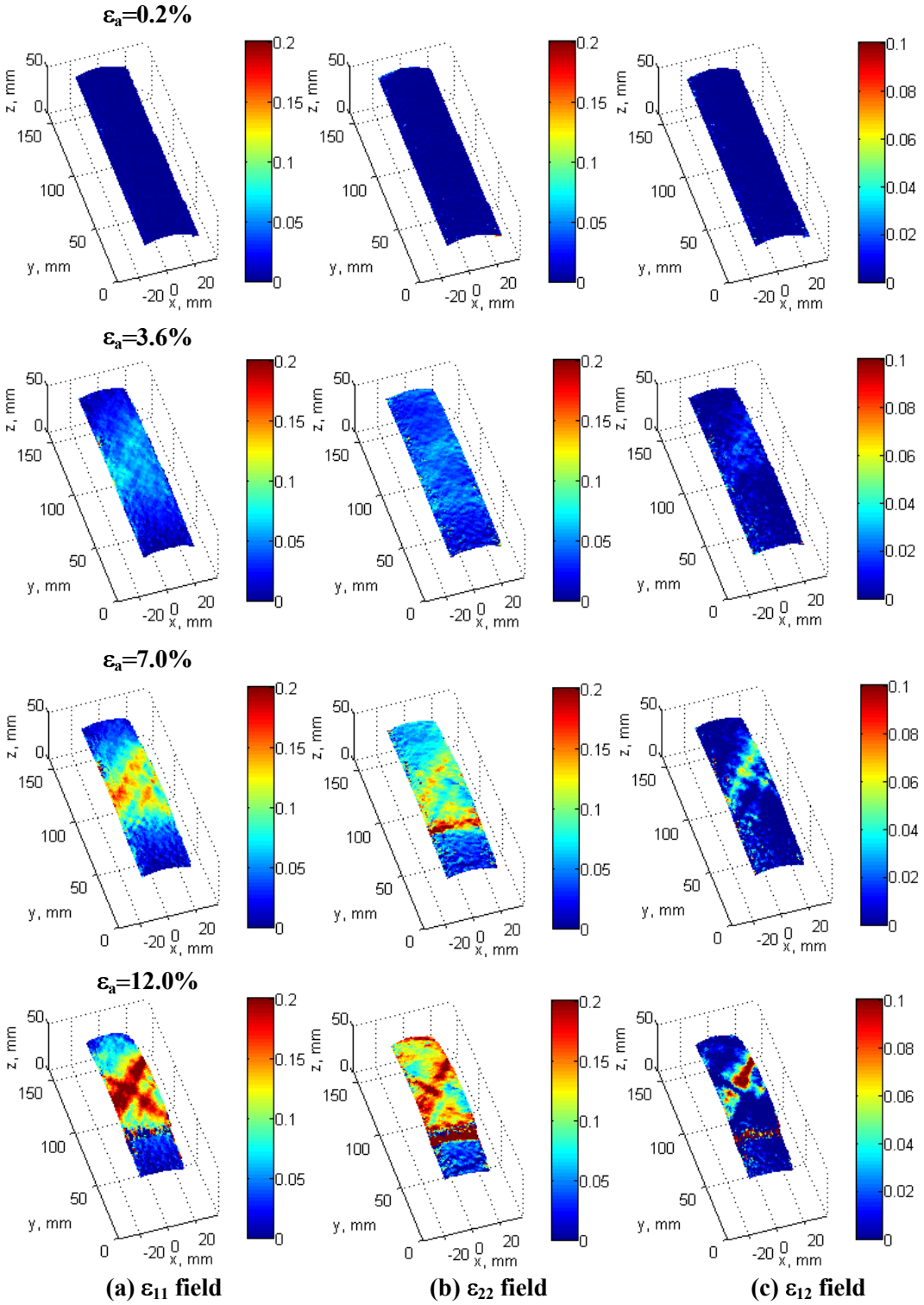

Figure 3. 22 Cumulative strain fields of test 120904c at 0.2%, 3.6%, 7%, and 12% of axial strain: (a) ε_{11} field (b) ε_{22} field (c) ε_{12} field

3.7 Volumetric Strain

Due to the lack of volumetric strain measurements (Plexiglass cell was removed to avoid image distortion), a method is proposed based on the representation of the volume specimen as a sum of a series of stacked disks. To determine the volume of the specimen making this assumption, it is required to know the diameter and height of each individual disk. The height of each disk was assumed to be a uniform height of 1 mm, whereas the diameter of each disk was obtained from the initial specimen profile, assumed as the average of the actual radius measured on the area of interest for each 'layer'. This approach has been used previously with a circular disk model to estimate the volume from a digitized image (Macari et al. 1997). Results from this technique showed a qualitative good agreement to conventional volumetric strain measurements obtained in wet conditions. This procedure was selected as an alternative method to measure the volume changes of dry sand specimens.

In order to compute the volume change of a specimen and volumetric strain according to the axial strain, the cylindrical volume calculation method was adopted. After transformation and interpolation of the coordinate data points, it is observed that these are not uniformly distributed on a Cartesian coordinate system. Thus, the data points and their displacements are redistributed on a material domain grid with each 1 mm space in the x-, y-, and z-directions. A representative radius of the i^{th} layer is computed by averaging the radius of each data points at the layer. The number of data and the y (height) range depend on the resolution of the digital image for the deformation process. Although digital image correlation is capable of showing a wide

range of a specimen surface at relatively early stages of loading, unfortunately the identifiable range decreases from the top platens as the loading progresses. The upper limit of the height is therefore bounded by 155~160 mm, which is the height of the samples, if the y-direction data exceeds the height of the sample. Otherwise, if y-direction data is recorded less than the height, a fixed data point with the measured height and radius is provided as an upper bound. The lower bound of a specimen is changing by the bottom platen and is reflected in the collected digital image data, so it does not need to be modified.

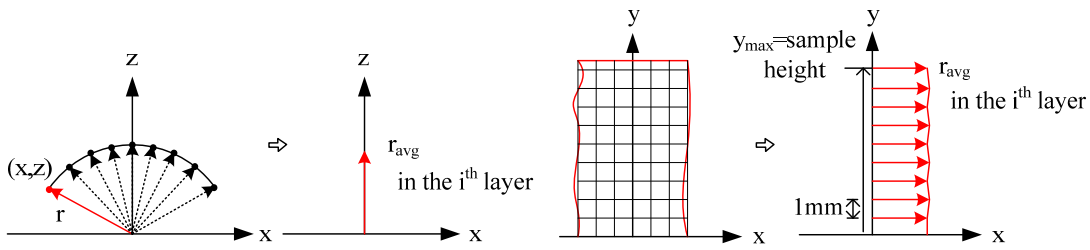

(a) averaged radius in the i^{th} layer (b) sample height and specimen profile

Figure 3. 23 Process for averaging radius and uniformalizing height

Once all the new coordinate data points with radius and heights are computed, the volume of each layer is estimated by the use of a trapezoidal numerical integration function and then added together. Since all the data points are forced to be located in a 1 mm grid and y-direction lower boundary change is not smooth, it is expected that the averaged volume with respect to height shows some variation.

$$V=\int_0^H \int_0^{2\pi} \int_0^R r\, dr\, d\theta\, dz=\int_0^H \int_0^{2\pi} \frac{1}{2}R^2\, d\theta\, dz=\frac{1}{2}R^2 2\pi \int_0^H dz=\pi \int_0^H R^2 dz$$

The local effects captured by the VIC-3D can be averaged with respect to the height of the specimen as illustrated in Figure 3.24, which presents the averaged radius profile in a blue line with a standard deviation in a red line, and the number of data points in a black line. The data points contacting on the top porous stone were lost in the interpolation and extrapolation process for cumulative displacements. Thus, the average radius at the top of the specimen is assumed as the initial measured radius of the sample, and the whole volume of the specimen is computed including the extrapolation of the missing data with respect to the initial condition.

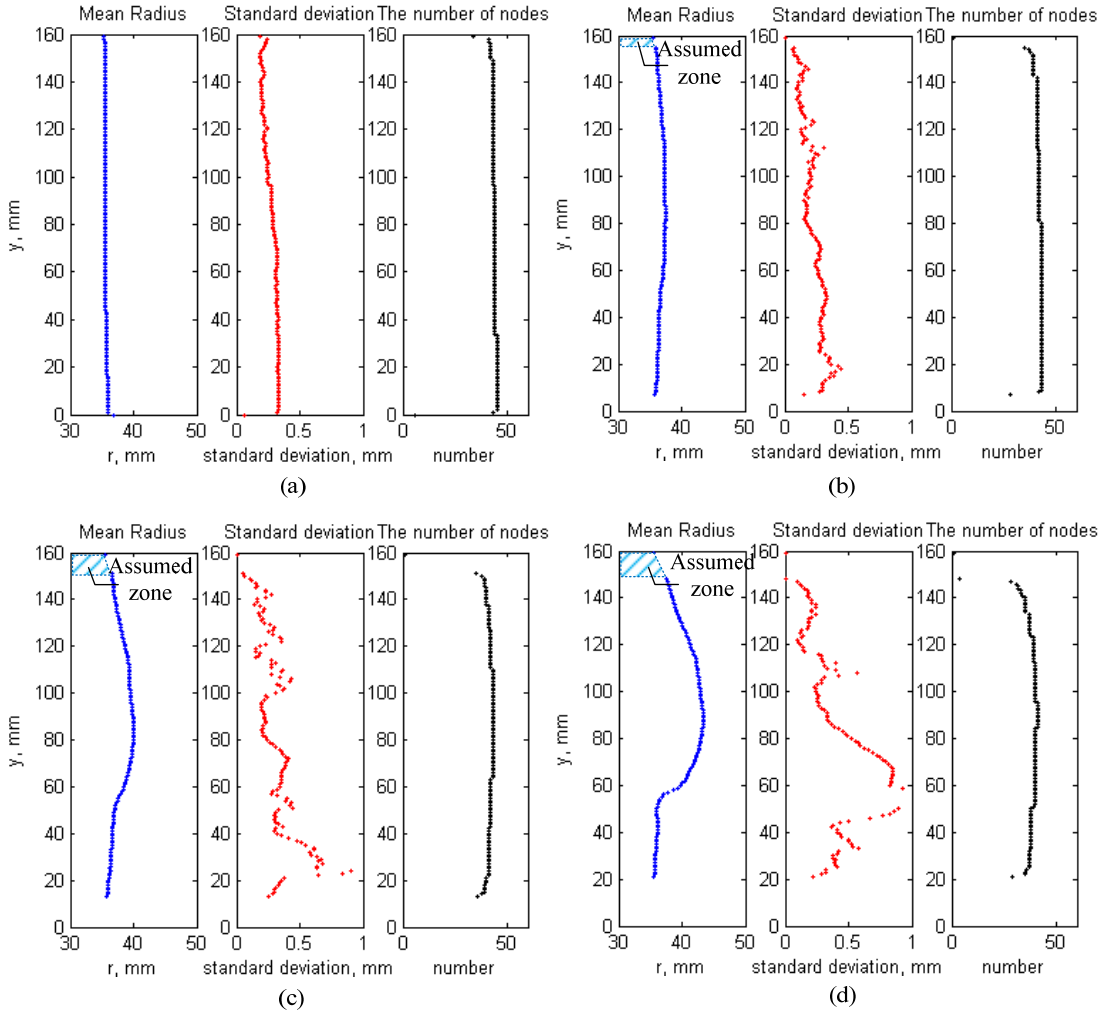

Figure 3. 24 Averaged radius profile for test 120904c at (a) 0.2% of axial strain (b) 3.6% of axial strain (c) 7% of axial strain (d) 12% of axial strain

Figure 3.25 presents the axial strain vs. volumetric strain relationship computed using the disks' profile assumption obtained from the radius profile after the VIC-3D digital image analysis. This example shows how the sample is compressed from the initial state up to 1.4% of axial strain and then dilates, until it reaches the critical state at 8.8% of axial strain. A calculation code for a sample volume is presented in Figure 3.26.

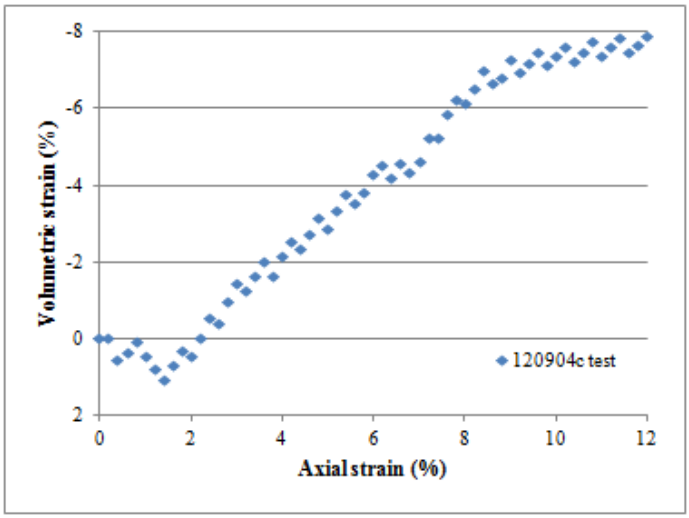

Figure 3. 25 Axial strain vs. volumetric strain curve of test 120904c

```
%<Part 4. Volume>%%%%%%%%%%%%%%%%%%%%%%%%%%%%%%%%%%%%%%%%%%%%%%%%%%%%%%%%%%%%
%height from 'DIA_SummaryAnlayses.xls' Data Summary sheet, use integer
height=159;
if yym(length(yym),1)>=height;
    row=find(yym(:,1)==height);
    vol=pi*trapz(yym(1:row,1),rmint_mean(1:row).^2);
    vol_add=0;
else
    yym=[yym;repmat(height,1,size(yym,2))];
    rmint=[rmint;radius repmat(nan,1,size(rmint,2)-1)];
    rmint_mean=[rmint_mean;radius];
    vol=pi*trapz(yym(:,1),rmint_mean.^2);
    row=find(yym(:,1)==height);
end
```

Figure 3. 26 Code for volume calculation

4. SIMPLE ONE ELEMENT MODEL TEST

4.1 Calibration of Model Parameters

The global stress-strain behavior of the test 120904c specimen captured by the triaxial testing system is presented in Figure 4.1 (a). This shows the typical behavior of a dense sand. Meanwhile, the volumetric strain is computed from the 3D-DIC analysis as explained before, since the specimen was vacuum consolidated. Results from the computed volumetric strain are presented in Figure 4.1 (b).

The interpretation of the triaxial results makes it possible to represent the dilative behavior of the sand by using an elasto-plastic model. The elastic and plastic parameters which can be deduced from the test are: Poisson's ratio, Young's modulus, dilation angle, axial strains at the characteristic state and the plastic limit as shown in Figure 4.1. The Mohr-Coulomb model parameters are determined by the graphical interpretation of the triaxial results according to the approach presented by Gay et al. (2003).

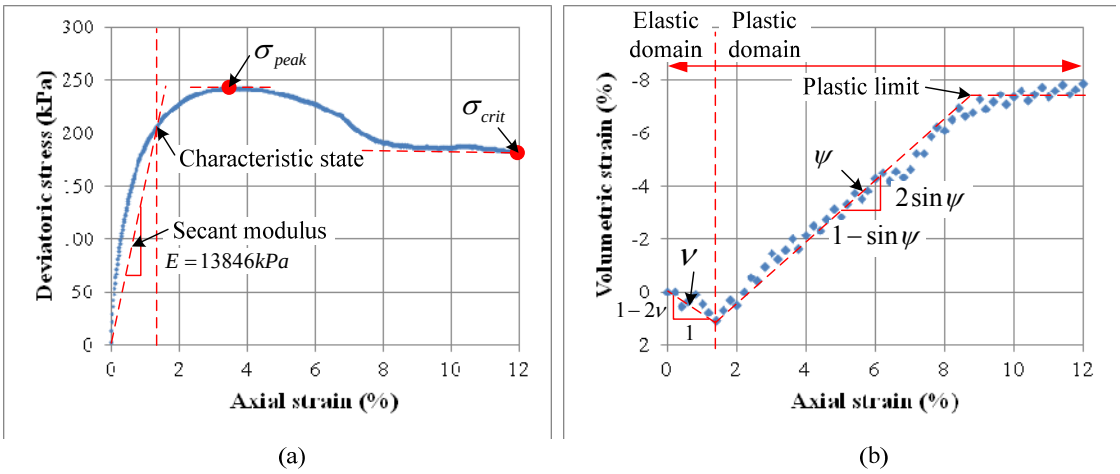

(a) (b)

Figure 4. 1 Global stress-strain behavior of test 120904c (a) stress vs. strain curve (b) axial strain vs. volumetric strain curve

4.2 One Element Model Test Cases

The purpose of performing a one element model analysis is to calibrate the soil constitutive model based on the global stress-strain measurements. In the case of the one element model, the local stresses and strains are expected to show small variations, compared with the global stresses and strains. Under this condition, the results of a finite element model could be directly compared to the calculation from the constitutive model, so the material properties and boundary conditions can be easily validated.

A set of analysis including one element model test cases, and its material properties are presented in Table 4.1. Both One_pk and One_cr tests were compared to explore the effect of the friction angle, which is obtained at the peak and critical state, and the One_pk_pp and One_cr_pp tests aimed at modeling sands using an elasto-perfectly plastic model, i.e. a traditional Mohr-Coulomb model. Test One_pk_step consists of two loading steps, an initial condition under consolidation and displacement

controlled loading, while the other tests consist of four steps. These aim at reconstructing the actual initial shape of the specimen by removing the isotropic compression from the initial condition and then add the isotropic compression followed by the shear loading, replicating the actual experimental loading conditions. One_cr_hs test is modeled by fitting a hardening and softening curve that is computed from the global stress-strain curve.

For the elastic state, the elastic modulus is estimated as 13,846kPa, the Poisson's ratio is estimated as 0.115. For the plastic state, the friction angles at the peak strength and at the critical state are estimated as 48.59° and 43.81° respectively, and the dilation angle is estimated as 24.30° for all cases. These material properties are determined by the graphical interpretation of the triaxial results according to the methodology outlined by Gay et al. (2003), which is illustrated in Figure 4.1.

Table 4. 1 One element model test cases and material properties

Name	Elastic modulus (kPa)	Poisson's ratio	Friction angle (deg)	Dilation angle (deg)	Note
One_pk	13,846	0.115	48.59	24.3	Hardening/Softening
One_pk_pp	13,846	0.115	48.59	24.3	Perfectly plasticity
One_cr	13,846	0.115	43.81	24.3	Hardening/Softening
One_cr_pp	13,846	0.115	43.81	24.3	Perfectly plasticity
One_pk_step	13,846	0.115	48.59	24.3	Hardening/Softening Two loading steps
One_cr_hs	13,846	0.115	43.81	24.3	Fitting hardening/softening

4.3 Boundary and Loading Conditions

By taking advantage of the symmetric configuration of a cylindrical specimen, a 2D axisymmetric finite element, 4-node bilinear with reduced integration (CAX4R) model is adopted. The geometry of the element is 10cm in height and 5cm in radius, following the height to radius ratio of the experimental sample.

The boundary and loading conditions were set up by referring to the examples about the consolidation of a triaxial test specimen (Bayoumi 2006; Helwany 2007; ABAQUS user's manual 2008). The initial and loading conditions consist of four steps: step 1 (initial geometry and confining stress), step 2 (release confining stress), step 3 (re-application of confining stress), and step 4 (shear loading). The stress paths of this sequence as described on the p-q stresses plane are illustrated in Figure 4.5 (a), while boundary conditions and stress loading at each step are shown in Figure 4.2. At step 1, the initial confining pressure is defined through the initial condition option in ABAQUS, with boundaries restrained so that the initial geometry of the specimen can be replicated. Step 2 simulates the actual initial state with a 'zero' stress condition by applying a tensile isotropic stress to the element. In this step, the restraints along the element boundaries are removed except for the bottom surface, letting the specimen deform to its true initial geometry. Assuming the element after step 2 is in the actual initial condition of a triaxial test, step 3 and step 4 simulate the actual confining and shear loadings. The confining pressure is applied on the element in step 3. From this experiment, it is observed that the boundary conditions for step 3 are the same as step 2. However, the stresses and displacements after step 3 indicate almost the same values as the results of

step 1. This means that the modeling of the actual initial state (step 2) has no effect on the initial geometry of the specimen. At step 4, only the top boundary is restrained and the bottom boundary is controlled by uniform displacement as a loading. As the element is compressed by the displacement control, both the mean and deviatoric stresses are increased. The mean stress and vertical displacement contours in Figure 4.3 and 4.4 prove that the boundary and loading conditions of all the procedures are set up correctly.

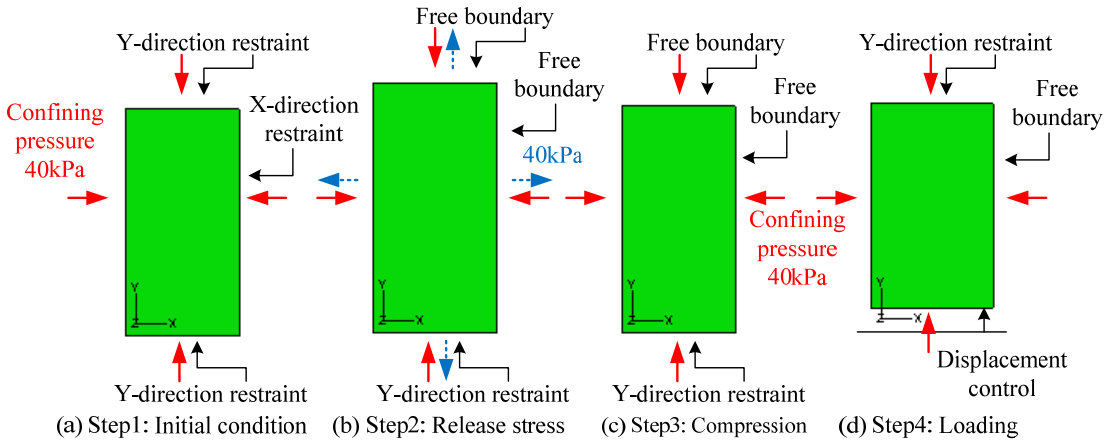

Figure 4. 2 Applied loading steps on the one element model

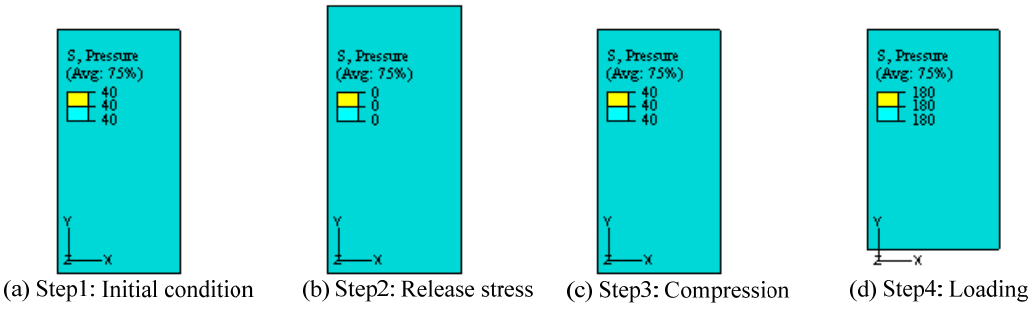

Figure 4. 3 Mean stress contour at different loading steps

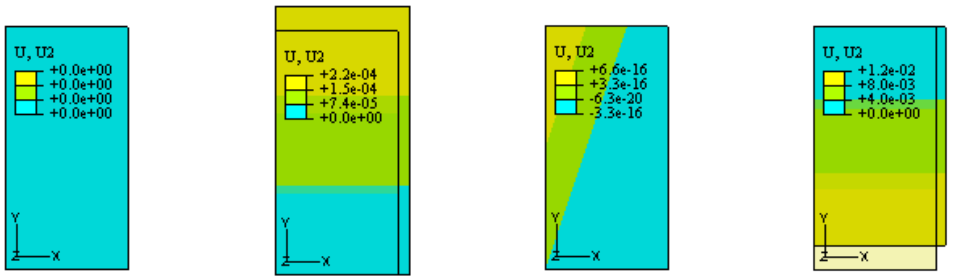

(a) Step1: Initial condition (b) Step2: Release stress (c) Step3: Compression (d) Step4: Loading

Figure 4. 4 Vertical displacement contour at different loading steps

In order to examine the loading phases, test One_pk with a full loading sequence (step 1 to step 4), and test One_pk_step with step 1 (initial condition) and step 2 (displacement loading) are compared in Figure 4.5. The stress path during loading is the same for both One_pk and One_pk_step tests and an observed difference is whether a model can simulate the real initial state with zero stress. An effect on the element by additional steps to simulate the process from the initial state to confinement is not expected to provide any additional stress or strain, which proves that step 2 and step 3 (release stress and confinement) can be neglected to provide an economical analysis on a larger finite element model.

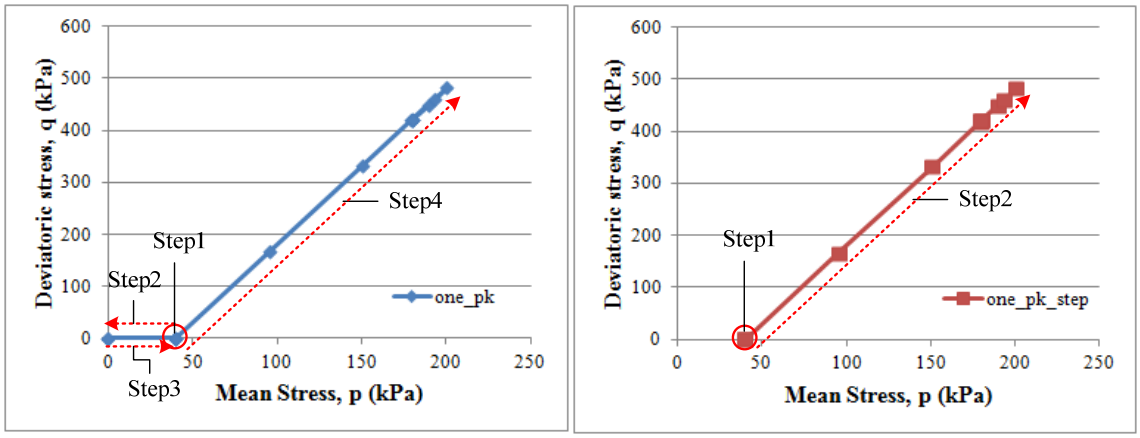

(a) Four loading steps (b) Two loading steps

Figure 4. 5 Stress paths in p-q plane (a) four loading steps condition of test One_ pk (b) two loading steps condition of test One_pk_step

In a loading step of a nonlinear finite element analysis, the step is divided into increments and iterate as much as necessary. Since increments that correspond to the force or displacement increments applied in nodes control the numerical solutions, it is important to obtain accurate result in the behavior of materials and to avoid iteration errors in solution process (Zienkiewicz and Taylor 2000; Sloan et al. 2001). In this study, the maximum increment was restricted to 1.2% of axial strain and the tolerance is 0.06% of axial strain with automatic incrementation that allows the flexible increment size for an effective analysis. In addition, Newton's method with unsymmetric stiffness matrix storage was used to solve this nonlinear problem. Some cases can be solved with the extra iteration by a symmetric matrix, but this problem with Coulomb friction was needed to use "unsymm" option to improve the convergence in ABAQUS. Since a friction coefficient was modified to simulate a hardening and softening behavior of

dense sands, it would not be able to complete the analysis without introducing the unsymmetric matrix storage.

4.4 Stress and Strain Behavior

From the experimental results it is observed that at the end of the tests the shear stress condition represents the critical state, where the soil continues to deform at a constant stress ratio q/p' and constant specific volume. The critical state line (CSL) is defined by the following equation, q=Mp', where M is the critical state parameter related to the friction angle at critical state, ϕ_{crit} (Schofield and Wroth 1968; Atkinson and Bransby 1978; Powrie 1997).

For an elasto-perfectly plastic material, the selected friction angle for the finite element model defines the slope of the yield surface by the critical state parameter, M that is related to the critical state as shown in Figure 4.6. Thus by taking the friction angle at the critical state, hardening and softening straining can be controlled by varying the yield surface.

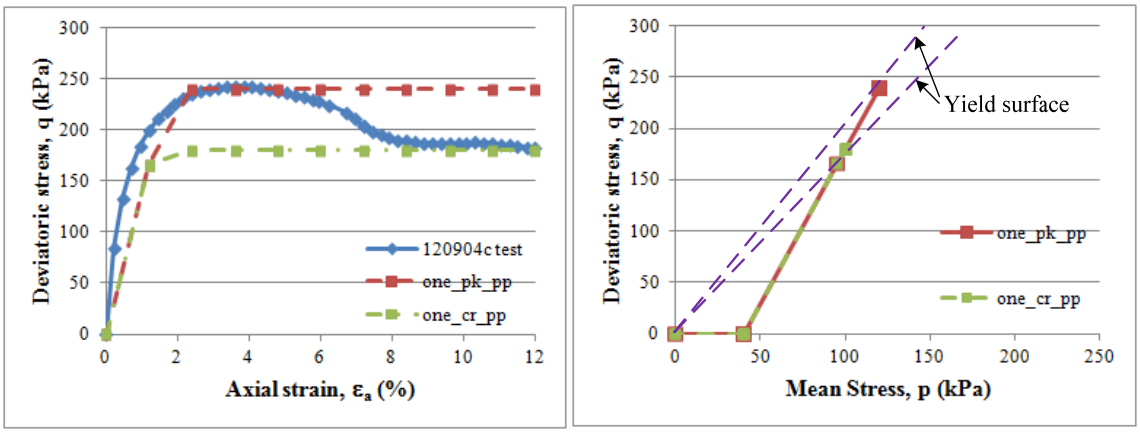

(a) Stress-strain curve (b) Stress path in p-q plane

Figure 4. 6 Comparison of stress-strain behavior of an elasto-perfectly plastic models with different friction angles at peak and critical state

An elasto-plastic models with hardening and softening laws (test One_pk) and an elasto-perfectly plastic model (test One_pk_pp) are compared in Figure 4.7. For the elasto-perfectly plastic model, the friction angles at both the critical state and peak state are the same ($\phi_{crit}=\phi_{peak}$). When the stress path reaches the critical state, where the soil response is perfectly plastic, a limit state is attained. If a model is used as a failure surface, the material exhibits an unlimited flow when the stress reaches yield. This is a perfect plasticity behavior. Since the model is also provided with isotopic hardening and softening, plastic flow causes the yield surface to change size uniformly with respect to all stress directions. This hardening and softening laws are useful for cases involving plastic straining, so the evolution of the yield surface with plastic deformation is described in terms of stresses as shown in Figure 4.7 (b).

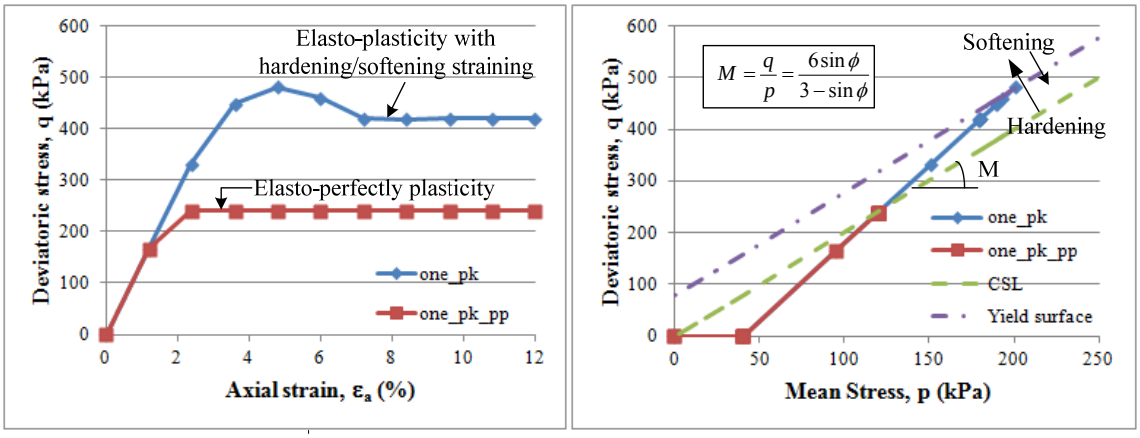

(a) Stress-strain curve (b) Stress path in p-q plane

Figure 4. 7 Comparison of stress-strain behavior between an elasto-perfectly plasticity model and an elasto-plasticity model

For the elasto-plastic model with the hardening and softening laws, the stress path jumps the critical state line because of hardening straining in Figure 4.7. The hardening and softening curve is defined as a relationship between the equivalent plastic strain (PEEQ) and cohesion yield stress (c) in ABAQUS. The cohesion yield stress must be greater than zero, in the case of an elasto-perfectly plastic material the cohesion yield stress is given as a very small number, for example, 10^{-6}. This means that if the friction angle at the peak state is used for the finite element analysis, the deviatoric stress never reach the limit at the critical state. This means that the friction angle at critical state should be applied as an input parameter for the soil constitutive model, and the peak stress of the soil would be controlled by the cohesion yield stress of the hardening/softening curve.

In the analysis, soil materials conformed to the Mohr-Coulomb yield criterion, which has already provided by ABAQUS, together with implementation of the

hardening/softening law. Figure 4.8 illustrates the Mohr-Coulomb yield surface in principal stress space and in the p-R_{mc}q stress plane as coded in ABAQUS. The yield surface touches the corner of hexagon at the Lode angle $\theta=\pi/3$ (triaxial compression). Various methods for smoothing the corners in Mohr-Coulomb yield functions have been discussed. Sloan and Booker (1986) modified yield functions for round vertices in the range 25° to 29° of Lode angle at which the transition occurs. Abbo (1997) used a hyperbolic approximation of the surface that removes all gradient singularities from the Mohr-Coulomb yield function. Zienkiewicz and Taylor (2000) modified the yield function that becomes an overall rounded surface. Similarly, the Mohr-Coulomb function defined in ABAQUS is modified to the elliptic function using a parameter that describes the out-of-roundedness in terms of stresses. This modification allows the convergence of numerical computation at corners in the yield surfaces.

The friction angle (ϕ) is defined as the slope of the Mohr-Coulomb yield surface in the p-R_{mc}q stress plane in ABAQUS (Figure 4.8). The Mohr-Coulomb yield criterion is defined as $F=R_{mc}q-p\tan\phi-c=0$, where ϕ is the friction angle and c represents the evolution of the cohesion of the material in the form of isotropic hardening or softening and a function of $\bar{\varepsilon}^{pl}$ (PEEQ) that is an equivalent plastic strain. R_{mc} is a function of the deviatoric polar angle (θ) and friction angle (ϕ) and defined as

$$R_{mc}(\theta,\phi)=\frac{1}{\sqrt{3}\cos\phi}\sin\left(\theta+\frac{\pi}{3}\right)+\frac{1}{3}\cos\left(\theta+\frac{\pi}{3}\right)\tan\phi$$

where the deviatoric polar angle (θ) defined as

$$\cos(3\theta)=\left(\frac{r}{q}\right)^3=\frac{3\sqrt{3}J_{3D}}{2J_{2D}^{3/2}}$$

If the deviatoric polar angle is equal to $\pi/3$, R_{mc} becomes a function of only the friction angle. The Mises equivalent stress (deviatoric stress), q, and a function of the third invariant of deviator stress, r, are define as follows.

$$q=\sqrt{\frac{3}{2}(S:S)}=\sqrt{3J_{2D}}$$

$$r=\left(\frac{9}{2}S\times S:S\right)^{\frac{1}{3}} \rightarrow r^3=\frac{27}{2}J_{3D}$$

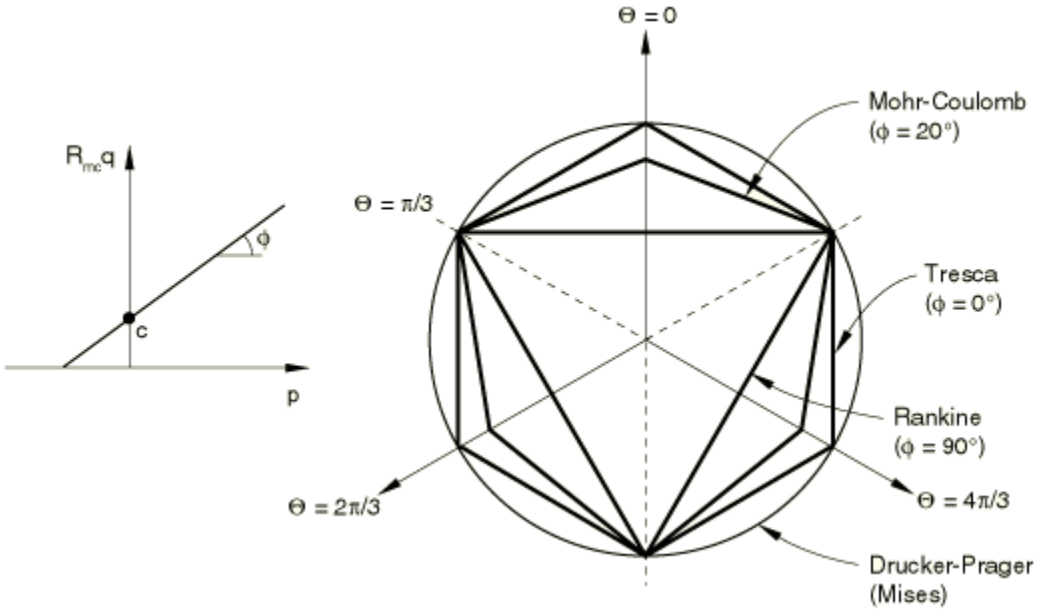

Figure 4. 8 Mohr-Coulomb yield surface in meridional and deviatoric planes (ABAQUS user's manual 2008)

4.5 Hardening and Softening Analysis

4.5.1 Stress and Strain Relationship in the Hardening and Softening Curve

As output of finite element analysis for the one element model, stress and strain components in vertical (notated as direction 1) and radial (notated as direction 2) are obtained, and these components are compared with the components that are computed by the equations of linear elasticity and the yield function and potential function of the Mohr-Coulomb model. The vertical total strain component (ε_{11}) is defined by the amount of displacement that applied as a loading and the deviatoric stress (σ_d) is captured as a reaction force on the top surface of an element. The elastic and plastic strain components (ε_{11}^e, ε_{22}^e, ε_{11}^p and ε_{22}^p) are calculated as follows.

$$\varepsilon_{11}^e = \sigma_d / E$$
$$\varepsilon_{22}^e = \varepsilon_{11}^e \times -\nu$$
$$\varepsilon_{11}^p = \varepsilon_{11} - \varepsilon_{11}^{el}$$
$$\varepsilon_{22}^p = \varepsilon_{11}^p \times \nu^p$$

where ν is the Poisson's ratio and ν^p is a plastic component of the Poisson's ratio, which is determined by plastic strain components. Dean and Crocker (2001) reported the plastic component of the Poisson's ratio determined under uniaxial tension for the linear Drucker-Prager model and this concept is modified to follow the Mohr-Coulomb model criterion.

The general flow rule is defined as

$$d\varepsilon^p = \lambda \frac{\partial Q}{\partial \sigma}$$

where Q is potential function as expressed $Q=\sqrt{(\in c|_0 \tan\psi)^2+(R_{mw} q)^2}$ -ptanψ

where $\in$ is a parameter for the meridional eccentricity, $c|_0$ is an initial cohesion yield stress, ψ is the dilation angle, and R_{mw} is as follows.

$$R_{mw}(\theta,e)=\frac{4(1-e^2)\cos^2\theta+(2e-1)^2}{2(1-e^2)\cos\theta+(2e-1)\sqrt{4(1-e^2)\cos^2\theta+5e^2-4e}} R_{mc}\left(\frac{\pi}{3},\phi\right)$$

where e is a parameter for the deviatoric eccentricity and by default, it can be defined as a function of the friction angle.

$$e=\frac{3-\sin\phi}{3+\sin\phi}$$

$$R_{mc}\left(\frac{\pi}{3},\phi\right)=\frac{3-\sin\phi}{6\cos\phi}$$

If the deviatoric polar angle (θ) is equal to $\pi/3$, R_{mw} becomes a function of the friction angle.

$$R_{mw}(\frac{\pi}{3},e)=R_{mc}\left(\frac{\pi}{3},\phi\right)=\frac{3-\sin\phi}{6\cos\phi}$$

Therefore, using the flow rule and the definition of a plastic component of the Poisson's ratio, ν^p is defined as a function of the friction angle and the dilation angle.

$$\nu^p=\frac{d\varepsilon^p_{22}}{d\varepsilon^p_{11}}\times\frac{1}{2}=\frac{\frac{\partial Q}{\partial \sigma_{22}}}{\frac{\partial Q}{\partial \sigma_{11}}}\times\frac{1}{2}=\frac{R_{mw}+\frac{2}{3}\tan\psi}{-R_{mw}+\frac{1}{3}\tan\psi}\times\frac{1}{2}=\frac{\frac{3-\sin\phi}{6\cos\phi}+\frac{2}{3}\tan\psi}{-\frac{3-\sin\phi}{6\cos\phi}+\frac{1}{3}\tan\psi}\times\frac{1}{2}$$

4.5.2 Determination of the Hardening and Softening Parameters

The Mohr-Coulomb model can be numerically adjusted to permit variations of the accumulated plastic strains, introducing a simple hardening rule consisting of segment zones, as reported by Potts and Zdravkovic (1999). Potts and Zdravkovic (1999) suggested a simple hardening rule that consists of three zones: in each zone, the variation of the strength parameters are assumed to increase from initial values to peak values, and to remain constant with equal to the peak values, and then to reduce from the peak values to residual values.

The same approach is implemented in ABAQUS, by introducing a hardening and softening curve that consists of the equivalent plastic strain (PEEQ, $\overline{\varepsilon}^{pl}$) and yield stress (a cohesion for the Mohr-Coulomb model). The relation between PEEQ and the yield stress is defined as a smooth curve by conducting a quadratic spline interpolation from the given five data points. The five data points imply the elastic limit, peak state, softening state, the beginning of critical state (plastic limit), and the final state based on the stress-strain curve produced from triaxial tests. The coordinates of these five data points are $A(\overline{\varepsilon}_{el}^{pl}, c_{el})$, $B(\overline{\varepsilon}_{pk}^{pl}, c_{pk})$, $C(\overline{\varepsilon}_{s}^{pl}, c_{s})$, $D(\overline{\varepsilon}_{pl}^{pl}, c_{pl})$, and $E(\overline{\varepsilon}_{f}^{pl}, c_{f})$ as shown in Figure 4.9.

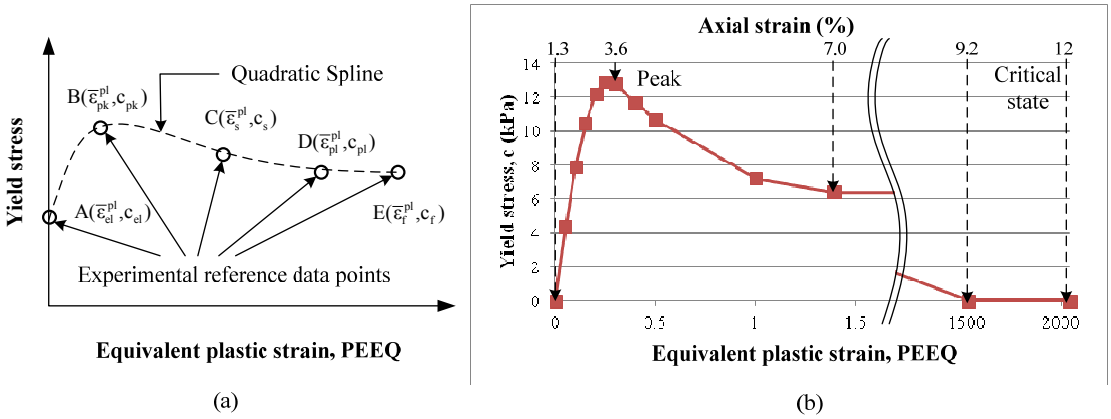

Figure 4. 9 Hardening and softening curve (a) concept of experimental data points (b) generated smooth hardening and softening curve

In order to define these control points, axial strains and deviatoric stresses (ε_{el}, ε_{pk}, ε_{s}, ε_{pl}, $\sigma_{d,el}$, $\sigma_{d,pk}$, $\sigma_{d,s}$ and $\sigma_{d,pl}$) at four data points representing elastic limit, peak state, softening state and plastic limit are required. Also for calculating the elastic and plastic parameters by graphical interpretation, the volumetric strains ($\varepsilon_{v,el}$ and $\varepsilon_{v,pl}$) at the elastic limit and plastic limit and confining pressure (σ_c) are required.

$$E=\frac{\sigma_{d,el}}{\varepsilon_{el}}$$

$$\upsilon= -\frac{1}{2}\left(1-\frac{\varepsilon_{v,el}}{\varepsilon_{el}}\right)$$

$$\phi=\tan^{-1}\left(\sqrt{\left(\frac{[(\sigma_{d,el}/2)+\sigma_c]^2}{[(\sigma_{d,el}/2)+\sigma_c]^2-(\sigma_{d,el}/2)^2}\right)}-1\right)$$

$$\psi=\sin^{-1}\left(\frac{\varepsilon_{v,el}-\varepsilon_{v,pl}}{2(\varepsilon_{pl}-\varepsilon_{el})+(\varepsilon_{v,el}-\varepsilon_{v,pl})}\right)$$

The elastic and plastic strain components are defined as in section. Stress components are defined as

$$\sigma_{11} = \sigma_d + \sigma_c$$
$$\sigma_{22} = \sigma_c$$

The cohesion yield stress is calculated by the yield function of the Mohr-Coulomb model, and the corresponding equivalent plastic strain is computed from the relationship between strain work and yield stress by the definition of the equivalent plastic strain.

$$c = \frac{(\sigma_{11} - \sigma_{22}) - (\sigma_{11} + \sigma_{22}) \times \sin\phi}{2\cos\phi}$$
$$\bar{\varepsilon}^{pl} = \frac{\sigma_{11} \times \varepsilon_{11}^{p} + 2(\sigma_{22} \times \varepsilon_{22}^{p})}{c}$$

4.5.3 Quadratic Spline Interpolation

The relationship between PEEQ and the yield stress can be expressed with a smooth curve by conducting a quadratic spline interpolation from the given five data points. A quadratic spline interpolation method is explained in detail below.

Given (n+1) data points, n splines exist with a quadratic equation, $a_i x^2 + b_i x + c_i = 0$, $i = 1,...,n$. Since there are 3n unknown coefficients, 3n equations are required. First, each spline goes through two consecutive data points. One spline passes two points, so 2n equations are obtained.

$$\begin{cases} a_i x_{i-1}^2 + b_i x_{i-1} + c_i = y_{i-1}, & i = 1,...,n \\ a_i x_i^2 + b_i x_i + c_i = y_i, & i = 1,...,n \end{cases}$$

Second, each spline has same slope at the interior data points, which means that derivatives are continuous at interior data points. From this, n-1 equations are obtained.

$$\frac{d}{dx}(a_i x^2+b_i x+c_i)\Big|_{x=x_i} = \frac{d}{dx}(a_{i+1} x^2+b_{i+1} x+c_{i+1})\Big|_{x=x_i}$$

$$2a_i x_i+b_i = 2a_{i+1} x_i+b_{i+1},\ i=1,\ldots,n-1$$

The last equation is obtained by assuming that the first spline is linear as $a_1=0$.

Therefore, by solving 3n equations, 3n unknown coefficients, $a_i, b_i, c_{i-i}=1,\ldots,n$ are obtained. Figure 4.10 is the code for calculation of the coefficients of a quadratic spline.

```
%Quadratic spline interpolation
clear all
x=[0 0.1041 0.2901 0.4180 0.5662];%equivalent plastic strain
y=[34.0168 45.3551 39.6861 34.0171 34.0171];%cohesion yield stress
Eqns_left=[x(1)^2 x(1) 1 0 0 0 0 0 0 0 0 0;
    x(2)^2 x(2) 1 0 0 0 0 0 0 0 0 0;
    0 0 0 x(2)^2 x(2) 1 0 0 0 0 0 0;
    0 0 0 x(3)^2 x(3) 1 0 0 0 0 0 0;
    0 0 0 0 0 0 x(3)^2 x(3) 1 0 0 0;
    0 0 0 0 0 0 x(4)^2 x(4) 1 0 0 0;
    0 0 0 0 0 0 0 0 0 x(4)^2 x(4) 1;
    0 0 0 0 0 0 0 0 0 x(5)^2 x(5) 1;
    2*x(2) 1 0 -2*x(2) -1 0 0 0 0 0 0 0;
    0 0 0 2*x(3) 1 0 -2*x(3) -1 0 0 0 0;
    0 0 0 0 0 0 2*x(4) 1 0 -2*x(4) -1 0;
    0 0 0 0 0 0 0 0 0 1 0 0];
Equns_right=[y(1);y(2);y(2);y(3);y(3);y(4);y(4);y(5);0;0;0;0];
coefficients=inv(Eqns_left)*Equns_right;
```

Figure 4. 10 Code for calculation of the coefficients of a quadratic spline

5. CASE STUDY

5.1 Simulation of the Compression Triaxial Test

The commercial finite element program ABAQUS (ABAQUS Inc., 2008) was used to simulate the specimen experimental response. A 2D finite element model illustrated in Figure 5.1 was built for the simulation of the triaxial compression test. Although the actual specimen was not a perfect cylinder, only half of the specimen, bounded by an axis of symmetry, was modeled by introducing the averaged initial radius profile to the 2D specimen representation.

For the initial conditions, the initial stress was specified by adopting the 'geostatic' option available in ABAQUS to calculate the stress, which is in equilibrium with the external loading and boundary conditions. The displacements that occur during the geostatic step should be near zero or negligible for the equilibrium condition, therefore no displacements in the directions perpendicular to outer surfaces were allowed with regard to the displacement boundary condition. At the same time, a distributed surface loading boundary condition was applied at the top, bottom and lateral surfaces to model a constant isotropic confining pressure of 40kPa applied by vacuum consolidation. The shearing in a standard automated triaxial testing system at a constant strain rate of 0.2%/min was introduced with a displacement controlled loading on the bottom of the model. Displacements were allowed at the lateral boundary, but an isotropic confining pressure was maintained during the compression test.

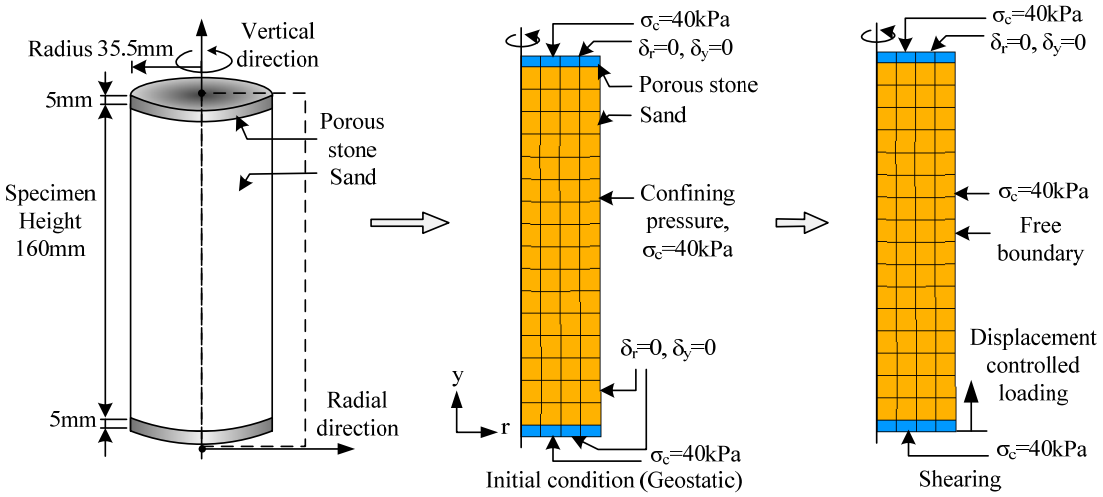

Figure 5. 1 2D axisymmetric finite element full model

5.2 Homogeneous Material Tests for a Dense Sand Specimen

5.2.1 Local Deformation Effects from a Dense Sand Specimen

The results from a 3D-DIC analysis on a dense sand specimen obtained during a triaxial test are used to investigate potential failure mechanisms, from a wide range of strain levels. The kinematic information of the digitally generated data was formatted by the combination of a 3D-DIC technique and an interpolation method. This approach permits the treatment of digitalized images by using a commercial digital image correlation program, and then enabling the assessment of cumulative local displacement fields as shown in Figure 5.2. It is anticipated that from the information of total displacements computed in the 'surface' of the specimen, this can be incorporated for solving the inverse problem for a spectrum of geomechanical models, with the aim of improving the understanding of the 'inner' composition and mechanical behavior of the

specimen. Accordingly, a better understanding of the mechanisms being involved in localized deformation at different stages of deformation is considered in this study, for the case of the triaxial compression test of a dense sand specimen.

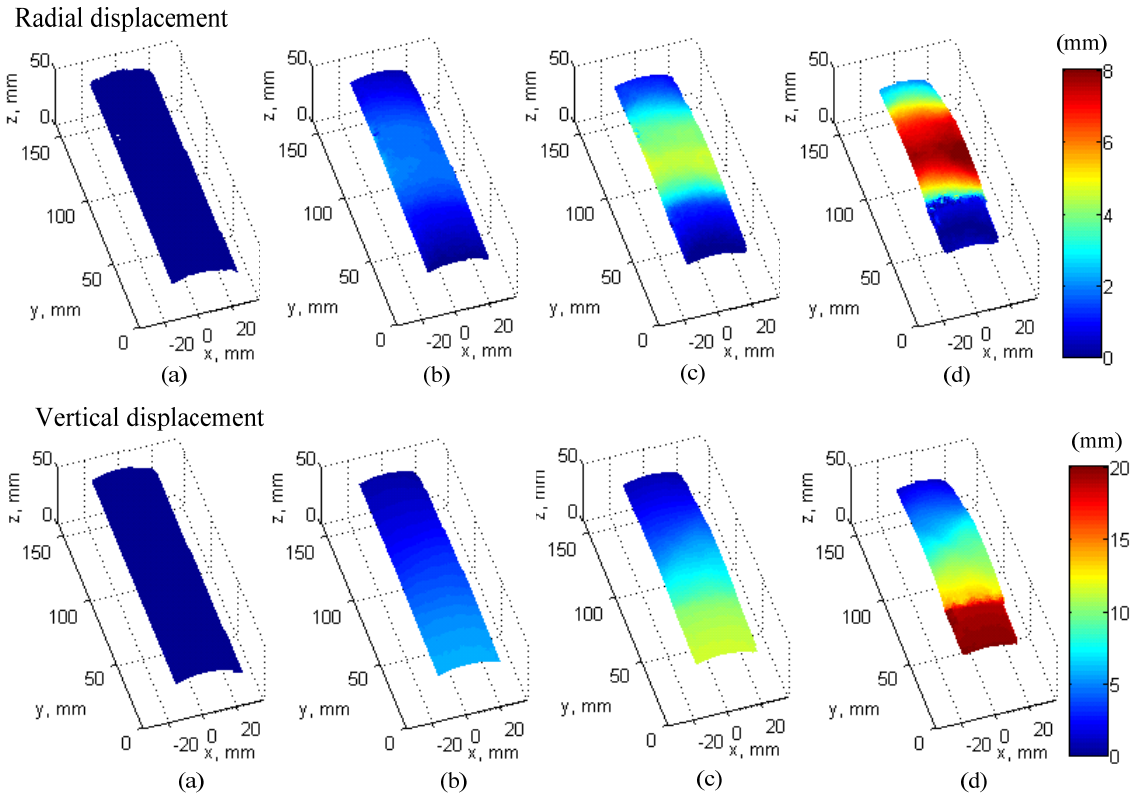

Figure 5. 2 Cumulative displacement fields at (a) 0.2% of axial strain (b) 3.6% of axial strain (c) 7% of axial strain (d) 12% of axial strain

5.2.2 Local Deformation of Homogeneous Materials

To describe mechanical behavior of a sand specimen during a specific deformation path, 2D axisymmetric analyses were carried out with spatially correlated homogeneous distributions of the material properties in a dense sand model, which was assumed to behave as a simple elasto-plastic constitutive model, following the Mohr-

Coulomb model but with hardening and softening capabilities (Potts and Zdravkovic 1999). A summary of the model parameters for homogeneous materials is provided in Table 5.1. Herein, the specimen is assumed to be homogeneous with three distinct values defined to explore the specimen response. The material property of Homogeneous_0 is found from the graphical interpretation discussed above. Homogeneous_p10 and Homogeneous_n10 have both the same elastic characteristics but with 10% increase and 10% decrease for the friction angle respectively, which introduces similar changes on the dilation angle. The hardening softening curve varies along the friction angle as presented in Figure 5.3.

Table 5. 1 Summary of model parameters for homogeneous materials

Property	**Sand**			**Porous stone**
	Homogeneous_0	**Homogeneous_p10**	**Homogeneous_n10**	
Unit weight (kN/m^3)	20	20	20	20
Young's modulus (kPa)	13,846	13,846	13,846	1,000,000
Poisson's ratio	0.115	0.115	0.115	0.2
Friction angle (deg)	48.59	53.45	43.73	-
Dilation angle (deg)	24.29	26.72	21.86	-
Model type	Mohr-Coulomb with hardening/softening curve			Linear Elasticity

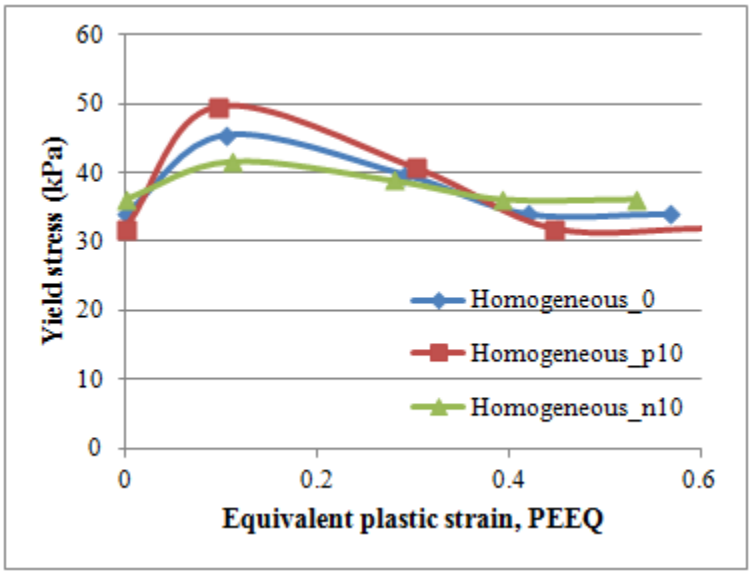

Figure 5. 3 Hardening and softening curve for homogeneous materials

A comparison of the global specimen's behavior vs. predictions of the finite element model is presented in Figure 5.4. Since material property of Homogeneous_0 is based on the global behavior of an actual triaxial test, the stress-strain curve is the closet to the actual test results. Model Homogeneous_p10 has the highest peak stress and Homogeneous_n10 shows the behavior of an elasto-perfectly plastic material. Homogeneous_p10 has excessive volumetric strain and Homogeneous_n10 shows the closest strain curve to the strain curve of the actual test at a peak stress, followed closely by Homogeneous_0. After the peak stress, the gap of volumetric strain between the test result and finite element models decreases.

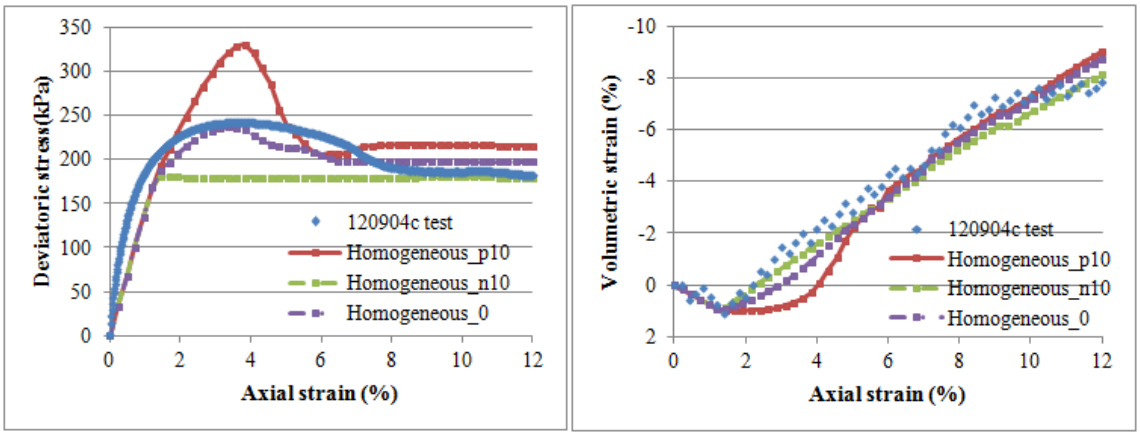

(a) stress-strain curve (b) axial strain vs. volumetric strain

Figure 5. 4 Global stress-strain behavior of homogeneous materials

Averaged radial and axial displacements at 3.6% and 7% of axial strain are used as benchmarks to compare model predictions vs. actual displacement fields as showed in Figure 5.5. This includes cumulative density functions of the corresponding displacement errors. The difference between the actual test and the model predictions are more evident at 3.6% of axial strain when comparing radial displacements. However, for vertical displacement deviations at the peak are not as significant as after the peak. Results showed better agreement on the vertical than in the radial displacements, with higher and unbiased deviations at the peak for the radial displacements over the tangential displacement, and similar unbiased deviations for both the radial and the tangential after the peak.

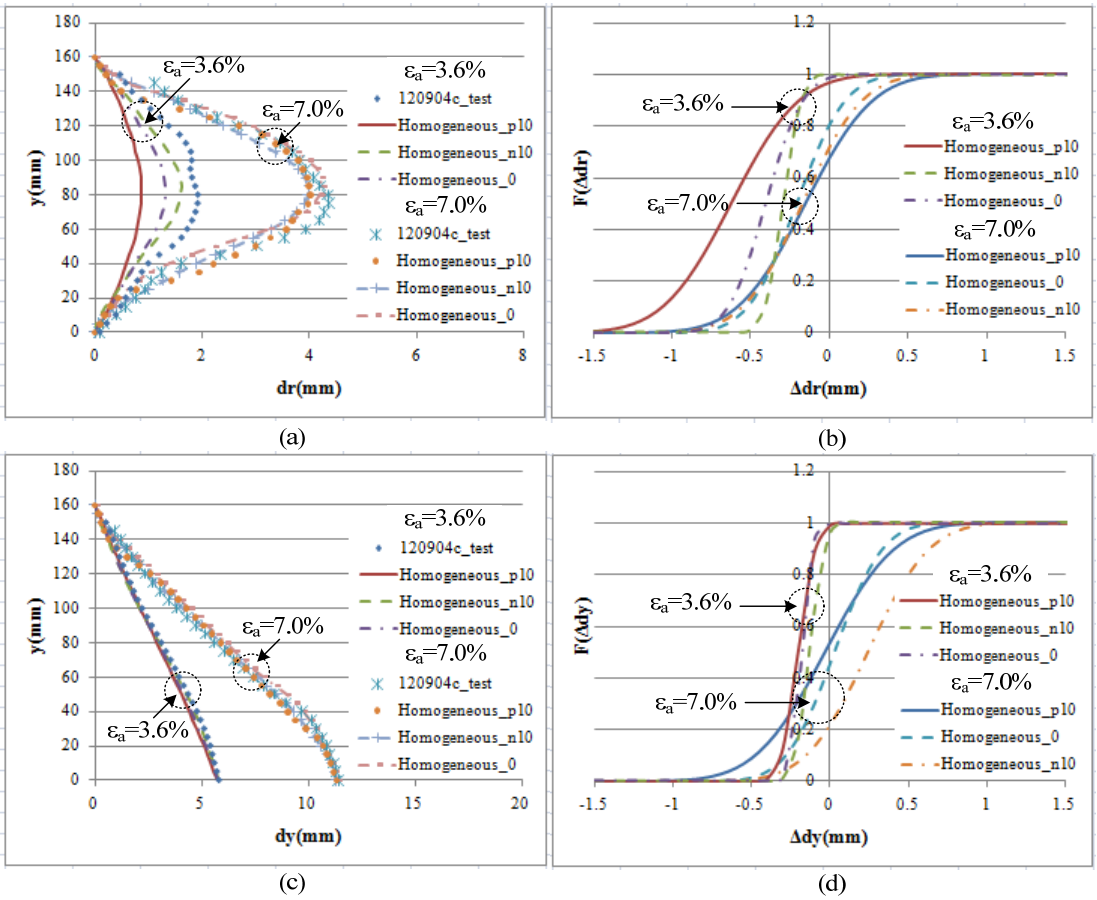

Figure 5. 5 Displacements and cumulative density function at 3.6% and 7% of axial strain (a) radial displacement (b) cumulative density function of radial displacement errors (c) axial displacement (d) cumulative density function of axial displacement errors

5.3 Mesh Sensitivity Analysis in Plastic Straining

5.3.1 Problem Definition

The research by Read and Hegemier (1984) used experimental observations to provide a comprehensive review about strain softening with respect to the effects of specimen size and shape. They concluded that the strain softening is not a real property of materials but rather, the results of inhomogeneous deformation that can be constructed

with a sufficiently small size of material elements. Therefore, a finite element method is proposed for numerically analyzing the behavior of materials which show strain softening. However, for numerical approaches on elasto-plastic materials, the numerical solutions suffer from instability and finite element mesh size sensitivity in stress-strain or load-displacement responses when the material enters the strain softening range. This has been acknowledged by numerous researchers and a number of approaches have been proposed to overcome these difficulties.

Pietruszczak and Mroz (1981) formulated the stiffness matrix accounting for the thickness of a shear band of the Coulomb-softening material in plane strain condition. They also showed the load-displacement curves are not sensitive to the mesh size used in the proposed model, compared to the results of a conventional finite element model that show high sensitivity in both the limit load and the slope of strain softening. Pietruszczak and Stolle (1985) discussed the influence of discretization of the finite element mesh and presented the results of the footing problem solved by the constitutive relationship suggested by Pietruszczak and Mroz (1981). Steinmann and William (1991) performed a convergence study of compressive failure for an elasto-plastic material under a plane strain condition. Although the peak point predictions correspond, the post peak response indicates mesh sensitivity and the localization performance of different elements.

Another finite element implementation of strain softening is an application of a damage variable in constitutive relations. Frantziskonis and Desai (1987a) proposed a model that separates the behavior of a material into the continuum part and the damaged

part. The damaged part is softened because of the accumulation of damage. The finite element solutions obtained by using the proposed model were not sensitive to the changes in mesh size for material response predictions (Frantziskonis and Desai 1987b).

Recently, finite element methods based on the discontinuities in displacements or strains are introduced for the localization analysis, which is caused by material instability (Borja 2000; Wells et al. 2002). The gradient regularization is also considered for finite element simulations of shear band formation during strain softening (de Borst et al. 1993; Anand et al. 2012).

In this study, numerical simulations of a drained triaxial compression test using a two-dimensional finite element model were carried out to calibrate an elasto-plastic soil constitutive model. Results from the numerical simulations are used to discuss the sensitivity of mesh discretization in terms of the material behavior. For the numerical analysis of the problem, robustness in the numerical solution for an elasto-plastic simulation of the soil specimen is difficult to expect, because numerical instability in a stress-strain response in the case of dense sands can be attributed to plastic straining effects. To characterize the extent of the sensitivity of these effects, a parametric study is introduced.

Previous studies on the similar problem related to the numerical modeling for granular materials are more focused on the model prediction in global behavior, by comparing the global stress-strain and volumetric strain predictions with respect to the test data (Wan and Guo 1998; Cameron and Carter 2009). Other studies related to the numerical simulation of a drained triaxial compression test are focused on the discrete

element modeling of the problem dealing with the characteristics of sand grains and its physical properties as a model parameter (Chang and Hicher 2005; Belheine et al. 2009).

However, this study is focused on the investigation of the localized deformation effects measured on the boundary of dense sand specimens by comparing the model predictions with experimental data. This comparison demonstrates the ability of the model to reproduce accurately the overall mechanical behavior of the specimens and to take into account the influence of local effects by an improved definition of mechanical parameters obtained by a three-dimensional digital image correlation analysis (3D-DIC), which is used to generate 3D local kinematic information retrieved from the deforming specimen.

5.3.2 Effects of Mesh Discretization

The actual process of the compression triaxial test, in terms of the initial and boundary conditions related to testing procedures and calibration of parameters was simulated via a finite element analysis. Under certain conditions based on the actual shearing process, the finite element analyses for typical dense sands are affected by the determination of the mesh discretization, such as element type and mesh size. The material behavior, in particular the plastic straining incorporating strain softening, is attributed to the sensitivity of this discretization. Therefore, the finite element model prediction was analyzed to quantify the effects of element type and mesh size. Figure 5.6 illustrates all the mesh types and sizes of the 2D models used in the parametric study. Mesh sizes of 3 mm, 5 mm, 10 mm, 20 mm, and 40 mm respectively, were used to vary

the number of elements, using triangular (denoted as 'tr') and rectangular (denoted as 'sq') elements. A summary describing the test cases is presented in Table 5.2.

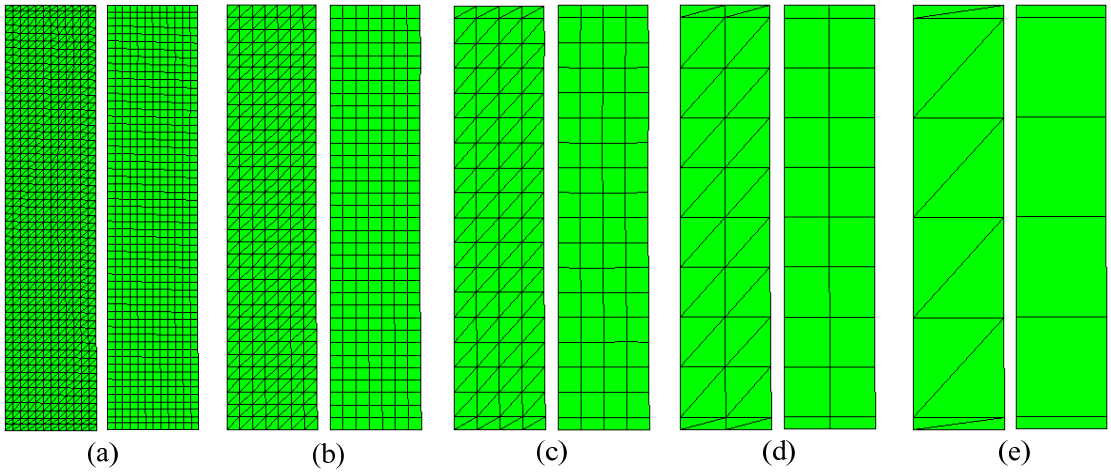

Figure 5. 6 Mesh discretization of 2D finite element models (a) 3mm_tr, 3mm_sq (b) 5mm_tr, 5mm_sq (c) 10mm_tr, 10mm_sq (d) 20mm_tr, 20mm_sq (e) 40mm_tr, 40mm_sq

Table 5. 2 Test cases for mesh sensitivity analysis

Name	No. of nodes	No. of elements	Mesh size (mm)	Element type
3mm_tr_3	754	1,368	3	a 3-node linear triangle
3mm_tr_6	2,875	1,368	3	a 6-node quadratic triangle
3mm_sq_4	754	684	3	a 4-node bilinear rectangle
3mm_sq_8	2,191	684	3	an 8-node biquadratic rectangle
5mm_tr_3	280	476	5	a 3-node linear triangle
5mm_sq_8	797	238	5	an 8-node biquadratic rectangle

Table 5.2 continued

Name	No. of nodes	No. of elements	Mesh size (mm)	Element type
10mm_tr_3	95	144	10	a 3-node linear triangle
10mm_sq_8	261	72	10	an 8-node biquadratic rectangle
20mm_tr_3	33	40	20	a 3-node linear triangle
20mm_sq_8	85	20	20	an 8-node biquadratic rectangle
40mm_tr_3	14	12	40	a 3-node linear triangle
40mm_tr_6	39	12	40	a 6-node quadratic triangle
40mm_sq_4	14	6	40	a 4-node bilinear rectangle

5.3.3 Effects of Element Type

The effects of element type are first examined by analyzing the global stress-strain behavior of the specimen. Four element types are compared when using 3mm and 40mm mesh sizes. As shown in Figure 5.7 (a), an 8-node biquadratic rectangle (sq_8) element generates a better prediction than a 3-node linear triangle (tr_3) element. This result shows the effects of the number of nodes and the number of integration points. With the higher order elements, or the more number of nodes, the prediction of the maximum stress is more accurate and the variation of stress at the critical state is also smaller. Another finding is that the results of fine mesh size (Figure 5.7 (a) and (b)) are nearly insensitive to the element type, as seen by the similar model predictions. In contrast, a coarse mesh (Figure 5.7 (c) and (d)) affects significantly the element type, as seen by the disparity in the stress strain curves.

Mesh size, 3mm

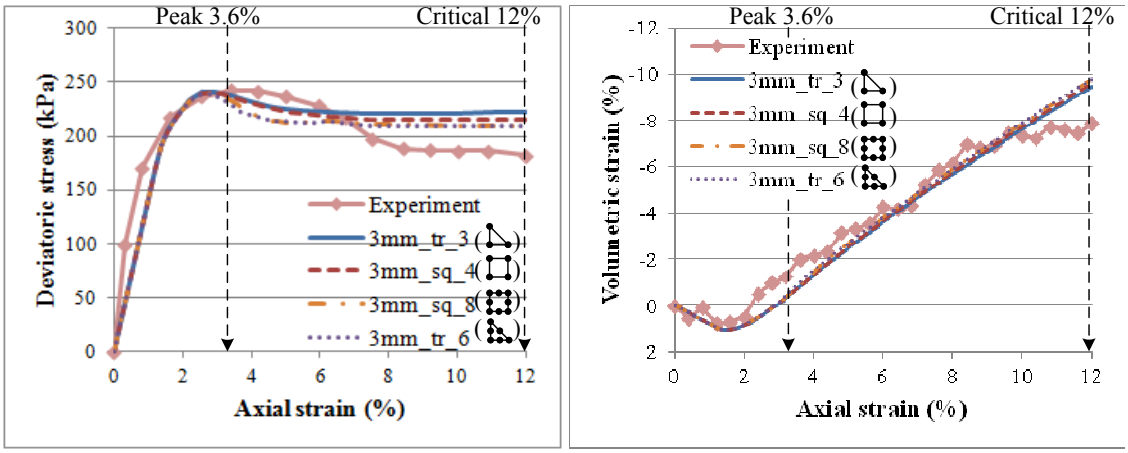

(a) (b)

Mesh size, 40mm

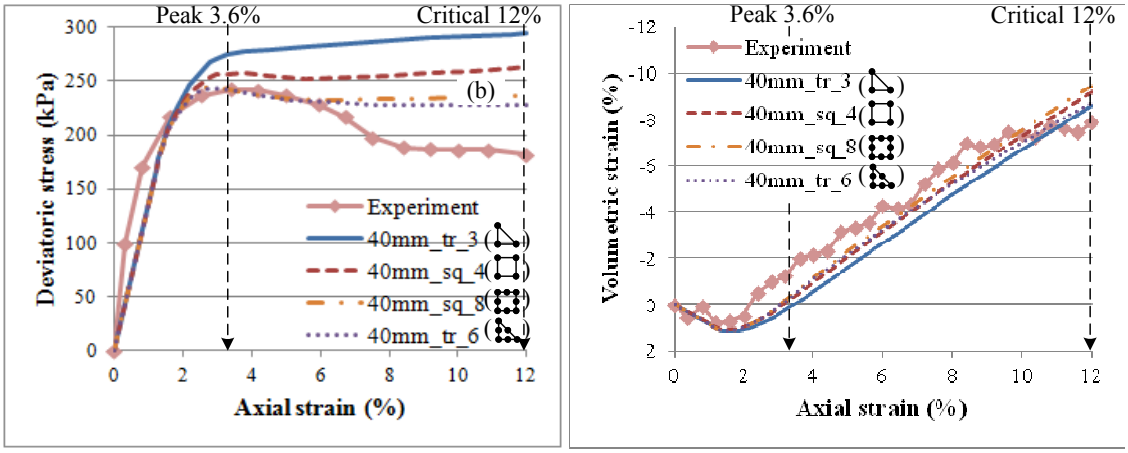

(c) (d)

Figure 5. 7 Effects of element type on global stress-strain behavior

5.3.4 Effects of Mesh Size

Figure 5.8 presents a comparison of the global stress-strain behavior due to different mesh sizes. The mesh size has an effect on the maximum stress and corresponding axial strain. For the coarse mesh, the magnitude of the maximum stress is higher and the slope of strain softening curve is decreasing, which constitutes an inaccurate prediction. For instance, the test 40mm_tr_3 in Figure 5.8 (a) does not exhibit a strain softening behavior, even though the softening law was imposed, and the stress difference between the prediction of the test 40mm_tr_3 and the experimental curve at the critical state is 120kPa. The axial strain at the maximum stress is, therefore, increasing as the mesh size becomes larger. Even though the influence of mesh size is significant on predicting stresses, the variation of the volumetric strain in the models is relatively small. The trends shown in Figure 5.7 and 5.8, presenting the peak stress and strain softening after peak are affected by both the number and type of elements, are in agreement with those by Petruszczak and Mroz (1981) and Petruszczak and Stolle (1985).

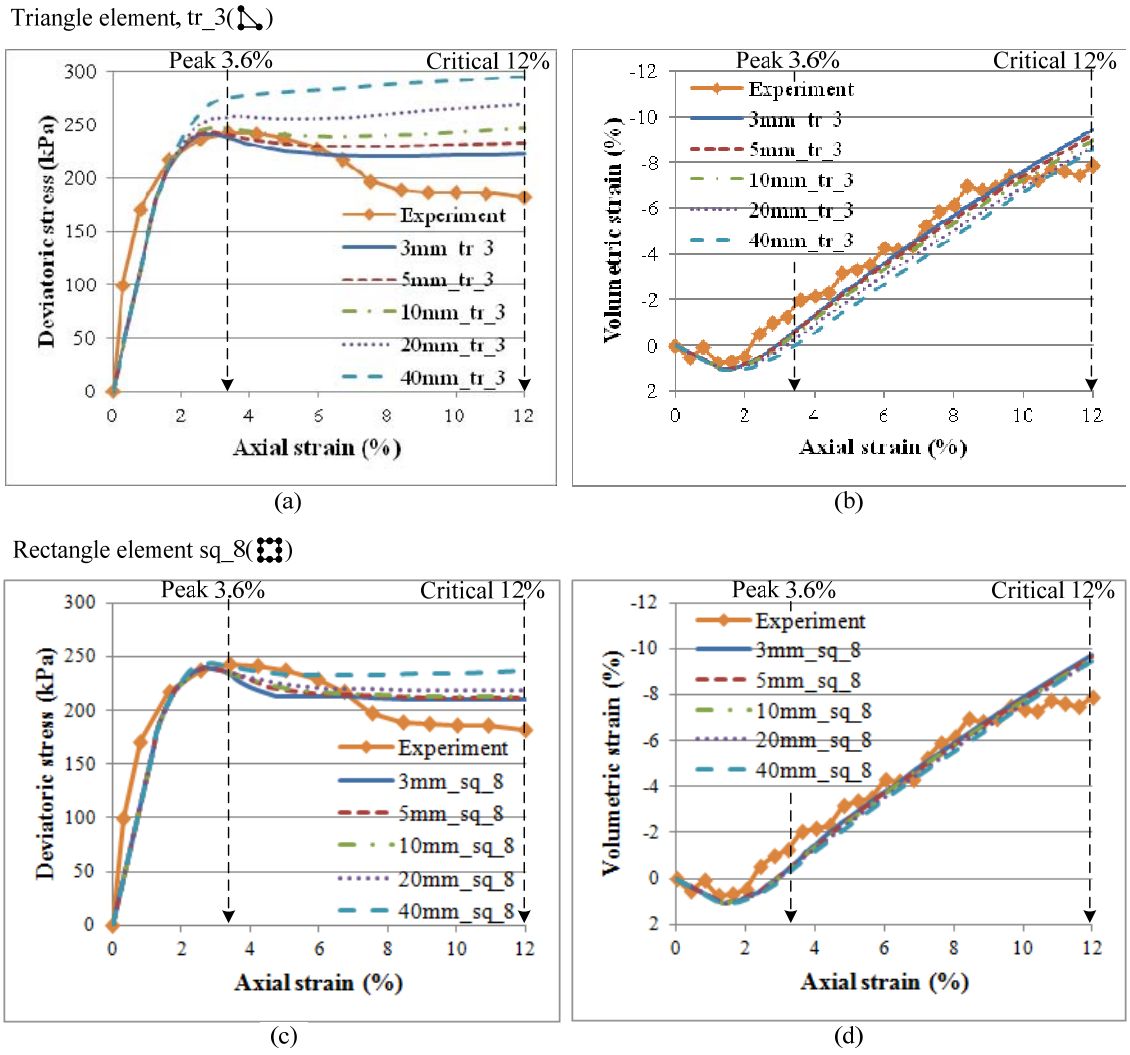

Figure 5. 8 Effects of mesh size on global stress-strain behavior

An innovative comparison now, is the analysis of the averaged radial and vertical displacements, representing the local kinematic effects. For instance, these displacements at the peak (3.6% of axial strain) and critical state (12% of axial strain) are used as benchmarks to compare model predictions as showed in Figure 5.9 and 5.10

respectively. The displacement errors (Figure 5.9 (b), (d) and 5.10 (b), (d)) indicate the difference between predictions and actual displacements.

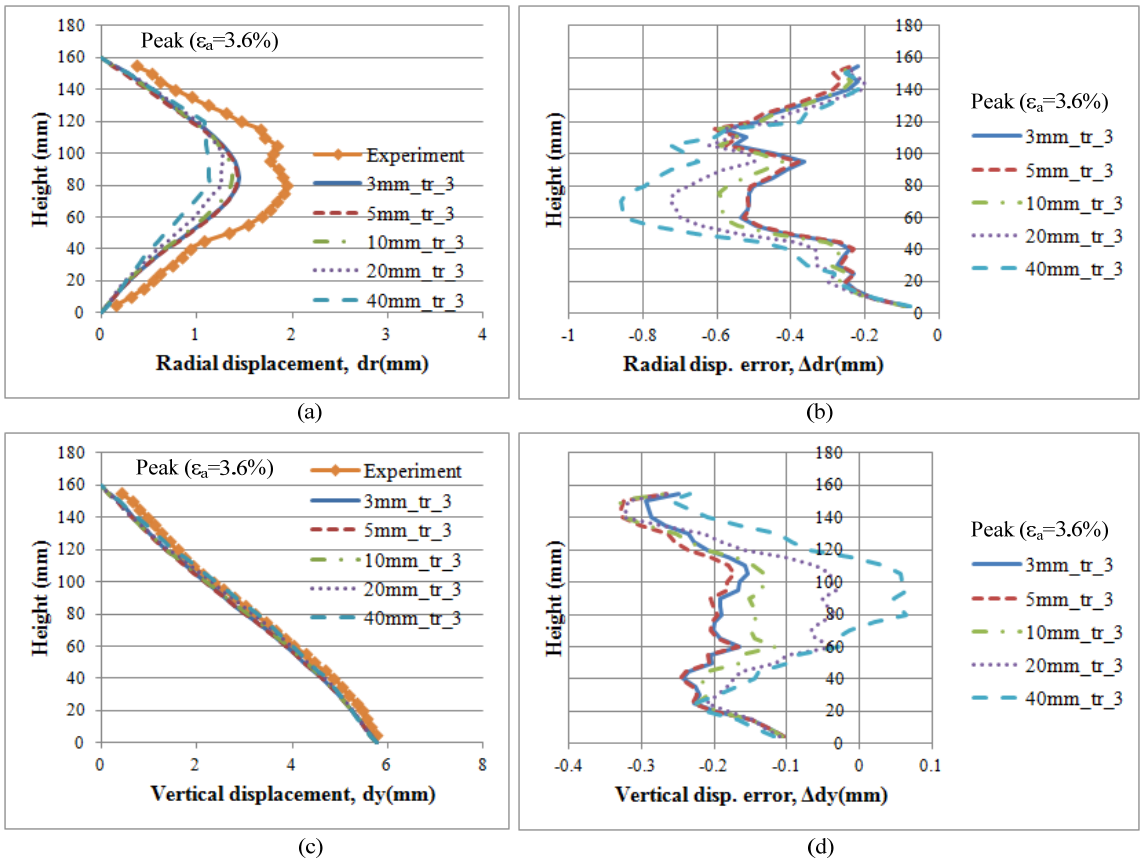

Figure 5. 9 Displacements and displacement errors at peak: (a) radial displacement (b) radial displacement errors (c) vertical displacement (d) vertical displacement errors

The difference between the actual test and the model predictions is relatively higher at the peak values when comparing radial displacements. The radial displacement predictions are distributed symmetrically around the middle of the specimen height. However, for vertical displacement, deviations at the peak are not as significant. Notice that the order of magnitude on the radial displacements is around 0.8 mm for the radial displacements, and 0.3 mm for the vertical displacements.

After the peak, the deformation within the specimen tends to localize along concentrated shear bands, and the relative differences between the experimental observations and the model prediction are relatively small for both the radial and vertical displacements. Due to the movement of the bottom one third of a specimen, the radial displacement error dramatically decreased at a height of 40mm. Notice the effect on the directionality of the triangular coarse mesh, such as the test 40mm_tr_3 (Figure 5.11 (3)), which imposes an effect on the location of maximum displacements, thus it causes an inaccurate prediction of displacements.

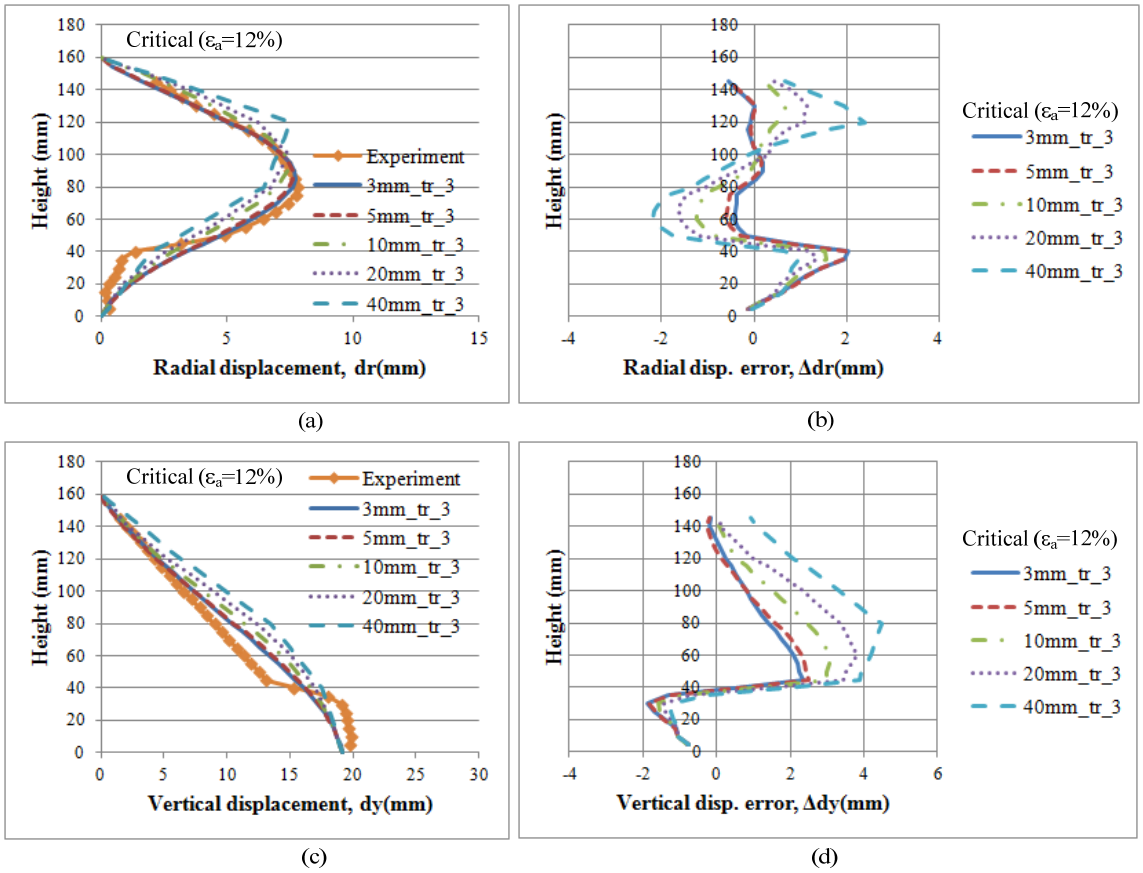

Figure 5. 10 Displacements and displacement errors at critical state: (a) radial displacement (b) radial displacement errors (c) vertical displacement (d) vertical displacement errors

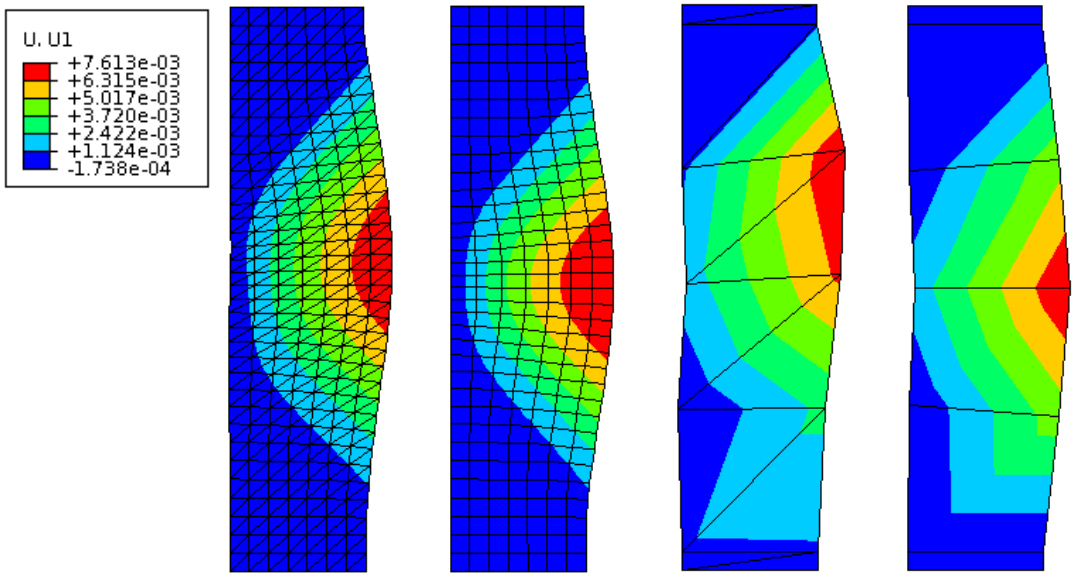

(a) 5mm_triangle (b) 5mm_square (c) 40mm_triangle (d) 40mm_square

Figure 5. 11 Deformed meshes with horizontal displacement contour

5.3.5 Stress and Strain Cross Sections

The deviatoric stress and plastic strain distribution in different stress states are illustrated in Figure 5.12, which describes the variation inside the specimen. The Mises equivalent stress is defined as $\sqrt{(2/3)\,S{:}S}$, where S=the stress deviator and the symbol (:) denotes a scalar product operation. The plastic strain magnitude, PEMAG is defined as $\sqrt{(2/3)\,\varepsilon^{pl}{:}\varepsilon^{pl}}$, where ε^{pl}=plastic strain.

While the deviatoric stresses at the peak and critical state in a global stress-strain curve are respectively 230kPa and 210kPa as shown in Figure 5.8 (c), the Mises stress ranges between 150kPa to 570kPa in Figure 5.12 (a). A stress concentration is observed at the center of the model specimen 100mm from the bottom, and the concentrated stress

diagonally dissipates with regard to strain softening. Figure 5.12 (b) indicates a significant increase in the plastic strain which is a result of strain softening as well. The deformation tends to localize along concentrated shear bands propagating within the specimen. On the other hand, these trends can be explained in terms of the material strength. The displacement load applied after the peak resulted in the increased deformation of the specimen due to the decreased strength of material.

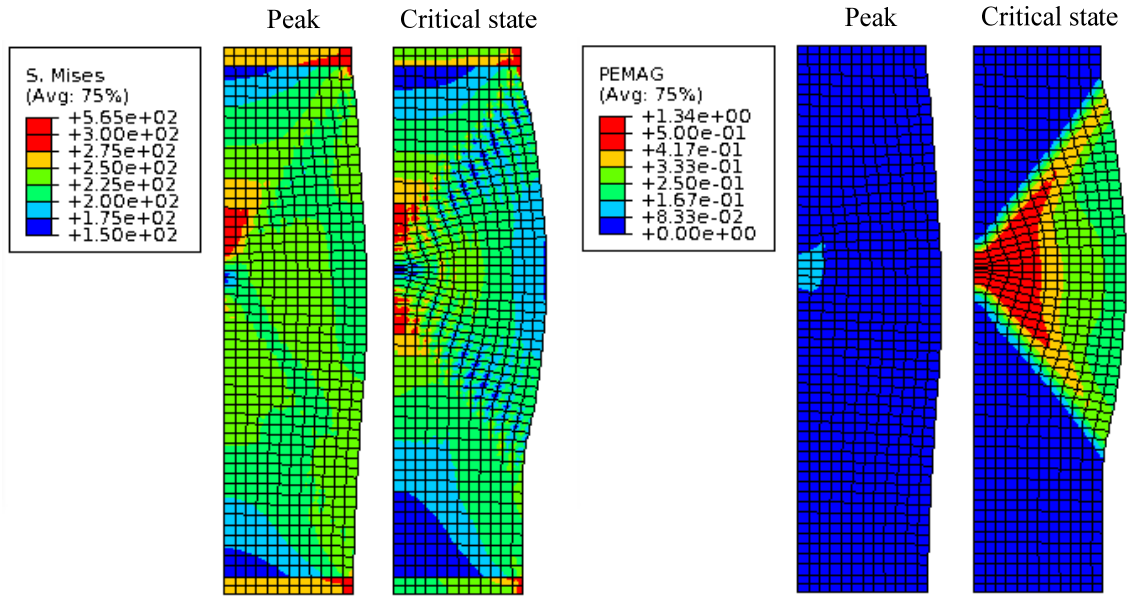

(a) Deviatoric stress distribution (b) Plastic strain distribution

Figure 5. 12 Deviatoric stress and plastic strain distribution of test 3mm_sq_8 at peak and critical state (a) deviatoric stress (b) plastic strain

5.4 Comparative Analysis among Dense, Loose and Layered Sand Specimens

5.4.1 Experimental Comparison

This study presents an elasto-plastic comparative analysis of different sand specimen configurations, including loose, dense and layered (half-loose half-dense) specimens. Experimental conditions were simulated by a finite element model with an elasto-plastic constitutive model, to investigate the elasticity and hardening plasticity responses of sand specimens during a triaxial test. Calibration of the numerical models for each specimen condition was based on the use of boundary information of the kinematics generated by 3D digital image correlation analysis. The photo images and cumulative displacement fields at the elastic and critical states are presented in Figure 5.13 and 5.14. In the elastic state, samples are compressed so radial displacement fields show negative values. Axial displacement fields are linearly distributed except in the case of the layered specimen in which the lower segment moves at the rate of loading and upper segment is compressed. The direction of shearing and the onset of shear bands can be estimated from tangential displacement fields.

A shear band of a dense sand specimen is clearly observed at the critical state and as the bottom segment of the specimen is separated from the bulging surface of the specimen by shearing, and then it moves independently as a single block. A loose specimen deformed symmetrically without shearing but bulging in radial direction is observed and this implies that the occurrence of bulging may cause an increase of volume. At the lower segment of the layered specimen, radial and tangential

displacements are not significant. The upper segment of the specimen shows a relatively significant deformation, which means that the deformation is concentrated on the weak part, i.e. the upper segment.

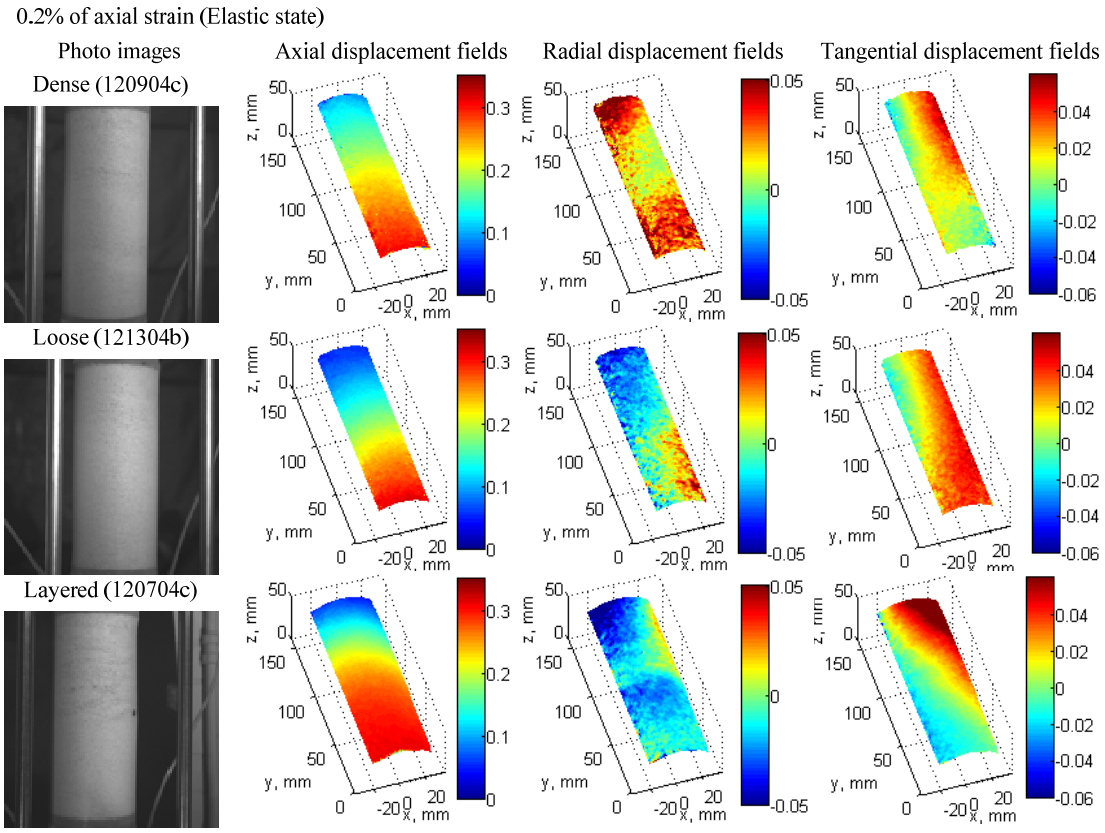

Figure 5. 13 3D digital image correlation analysis at 0.2% of axial strain (elastic state)

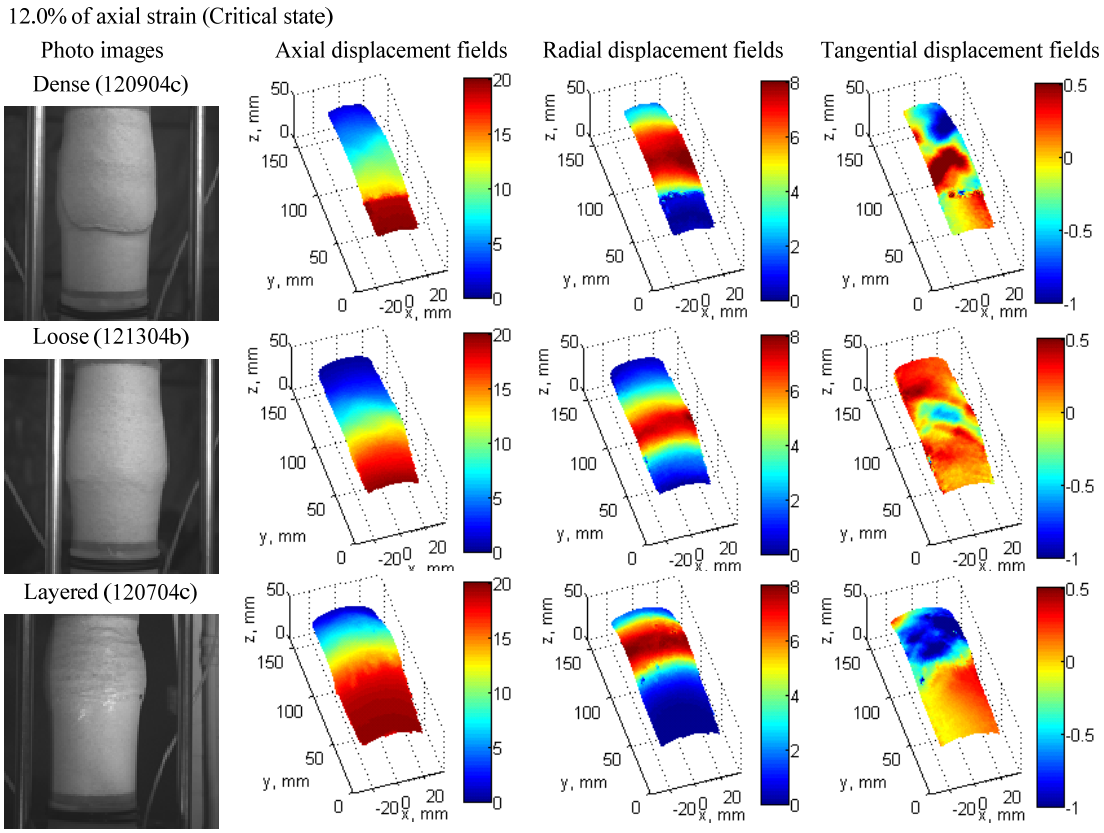

Figure 5. 14 3D digital image correlation analysis at 12% of axial strain (critical state)

Global stress-strain and volumetric strain curves are presented in Figure 5.15. The global behavior of a layered specimen that consists of two layers with different densities but the same heights shows a typical behavior of a loose specimen and even the maximum stress is also close to the maximum stress of the loose specimen. This means that the kinematic characteristics of the multi-layered soil structure are controlled by a weak layer, and averaged material parameters of all layers will overestimate the actual global behavior though depth of layers are considered.

Volumetric strains of the loose and layered specimens show dilation like a dense sand specimen in Figure 5.15 (b). Relative densities of loose and layered specimens are 46.39% and 68.90% respectively. Note that the relative density of the layered specimen is an average value that was computed from the total volume of the specimen. The condition of granular materials can be determined by relative density. The material with 15% to 50% of relative density is defined as a loose material, and with 50% to 70% of relative density it is defined as a medium material (Das 2001). Also, some experimental data of sands with relative density between 42% and 47% shows dilation in global volumetric strain behavior (Finno and Rechenmacher 2003). If these two samples are assumed as medium material, this dilation phenomenon in volume can be explained.

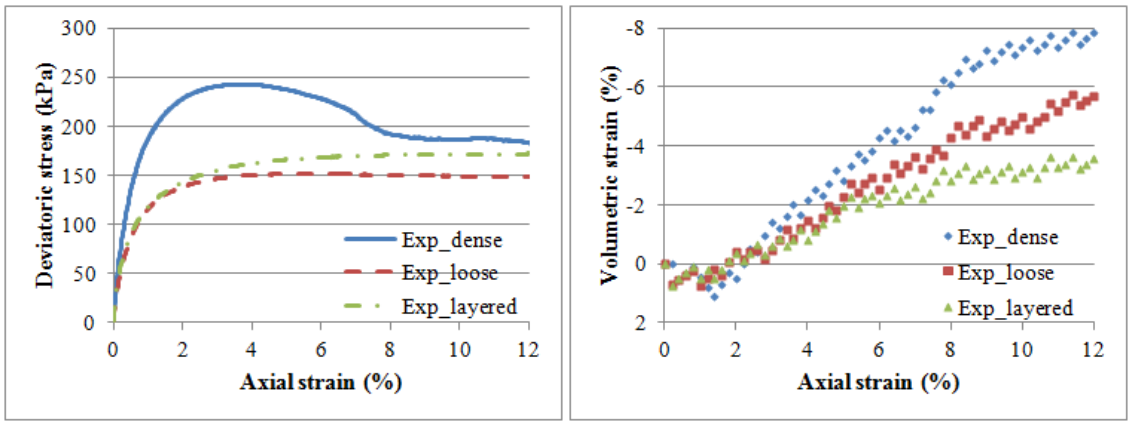

(a) stress-strain ccruve (b) axial strain vs. volumetric strain

Figure 5. 15 Comparison between experimental results (a) deviatoric stress vs. axial strain curve (b) volumetric behavior vs. axial strain

5.4.2 2D Axisymmetric Finite Element Modeling

For a simulation of triaxial tests on sand specimens, a 2D axisymmetric finite element model is adopted. Dense and loose specimens are modeled as homogeneous materials. A layered specimen is analyzed in both homogeneous and heterogeneous materials considering the specimen configurations. For a layered specimen, three cases are considered: a homogeneous material using the global kinematics captured in Figure 5.15, a heterogeneous material with two layers of loose and dense sands as built in experimental sample preparation, and another heterogeneous condition considering transition zone between loose and dense sands (Figure 5.16).

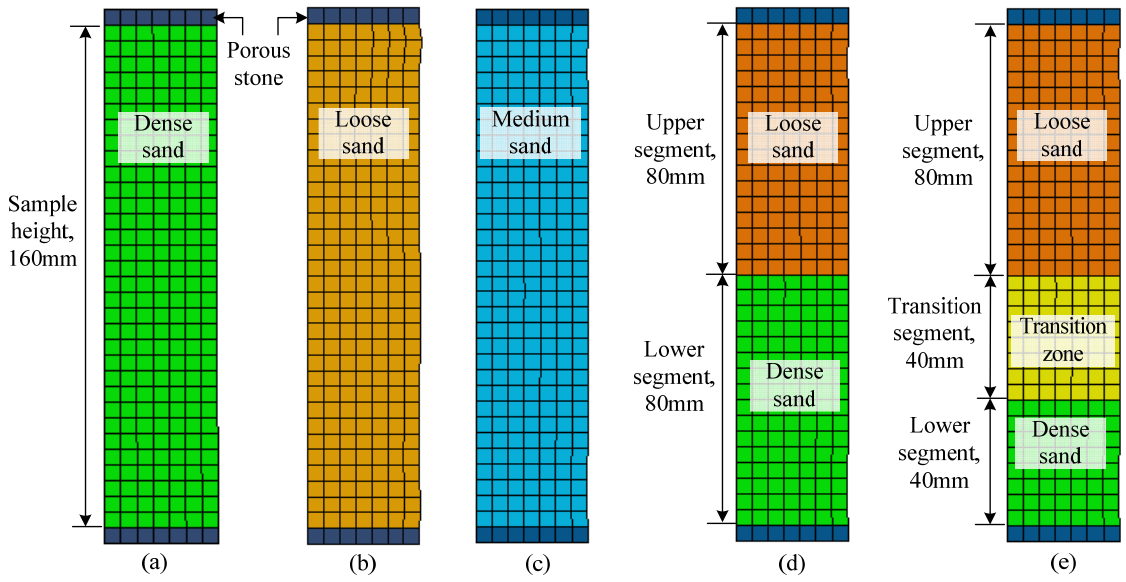

Figure 5. 16 Sand specimen configurations (a) dense specimen (b) loose specimen (c) layered specimen modeled with a homogeneous material (layered_hom) (d) layered specimen consists of two layers (layered_het) (e) layered specimen considering a transition zone (layered_het_transition)

A summary of material properties for dense, loose and layered samples is presented in Table 5.4. For a lower dense segment, the properties of a dense specimen are adopted since both are very dense materials. However, the upper loose segment requires a modification of the properties of a loose specimen because the loose sample has the characteristics of a medium material but the upper segment may behave more like a loose material. Duncan (2004) suggested an equation for an estimate of the friction angle from an experimental database of relative density, grain size, particle gradation and pressure as a form of ϕ=A+B(D_r)-[C+D(D_r)]$\log_{10}\left(\frac{\sigma_N}{P_a}\right)$, where D_r is a relative density, σ_N is a confining pressure, and P_a is the standard atmospheric pressure of 101.325kPa. The coefficients A, B, C, and D that are dependent on the material type are presented in Table 5.3.

Table 5. 3 Coefficients for an estimation of the friction angle (Duncan, J.M. 2004)

Material type	A	B	C	D	Standard deviation
Gravel with C_u>4	44	10	7	2	3.1°
Sand with C_u>6	39	10	3	2	3.2°
Sand with C_u<6	34	10	3	2	3.2°

Using the equation, the friction angle for the upper loose segment is determined to 38.51° with a standard deviation of 3.2° at the critical state. Since friction angles used for a finite element analysis are computed at the elastic limit, it may be smaller than the friction angles at the critical state. Thus the ratio of the friction angle of the upper

segment to the friction angle of the loose sample at the critical state is used to modify the hardening/softening curve of the loose sample. The adopted hardening and softening curve is presented in Figure 5.17. The parameters of the transition zone are computed by averaging two global stress-strain curves of loose and dense specimens.

Table 5. 4 Summary of material properties for dense, loose and layered specimens

Name		Unit weight (kN/m^3)	Young's modulus (kPa)	Poisson's ratio	Friction angle (deg)	Dilation angle (deg)	Relative density (%)	Note
Dense		20	21,559	0.44	43.09	22.78	91.83	homogeneous
Loose		20	15,818	0.25	32.86	14.48	46.39	homogeneous
Layered _hom	Medium	20	18,164	0.2	32.12	11.97	68.90	homogeneous
Layered _het	Upper loose	20	15,818	0.25	32.86	14.48	30.54	heterogeneous, two layers
	Lower dense	20	21,559	0.44	43.09	22.78	98.87	
Layered _het _transition	Upper loose	20	15,818	0.25	32.86	14.48	30.54	heterogeneous, three layers including transition zone
	Transition zone	20	20,361	0.37	36.86	18.19	-	
	Lower dense	20	21,559	0.44	43.09	22.78	98.87	
Porous stone		20	1,000,000	0.2	-	-	-	linear elasticity

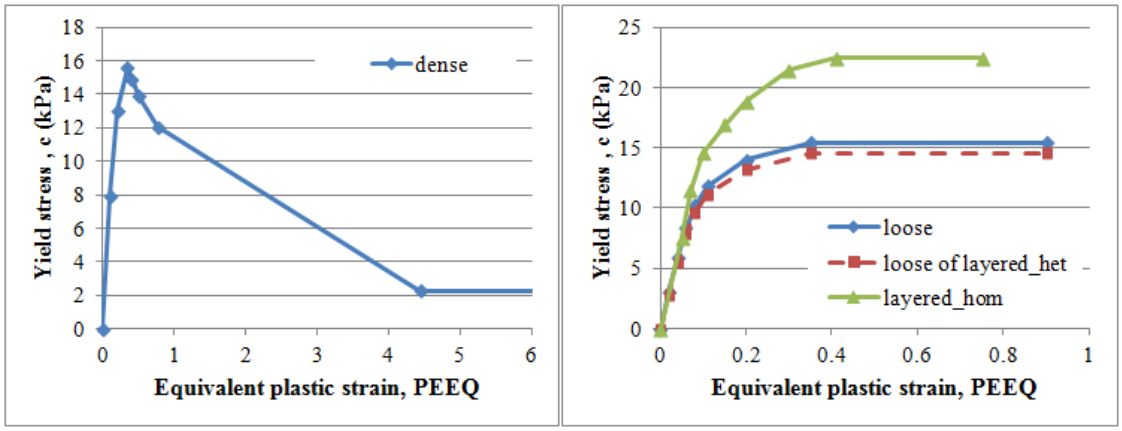

(a) dense **(b) loose, loose of layer_het and layerd_hom**

Figure 5. 17 Hardening and softening curves for (a) dense specimen (b) loose specimen, upper loose segment of layered_het model, and layered_hom model

5.4.3 Comparative Results

Figure 5.18 and 5.19 illustrated model predictions with experimental results. Results show that the numerical model predictions are in good agreement with the laboratory tests in terms of stress. With respect to volumetric strain, compression in elastic state is underestimated by adopting a tangential elastic modulus for a better prediction of stress in the elastic state. For a layered specimen, 'layered_hom' test shows the best fit to global behavior of a laboratory test and other two heterogeneous models shows about 10 to 20kPa of deviation in a stress-strain curve. It may be occurred because of the deviation in the estimation of the friction angle or neglect of a difference of material properties between a dense specimen and the lower dense segment.

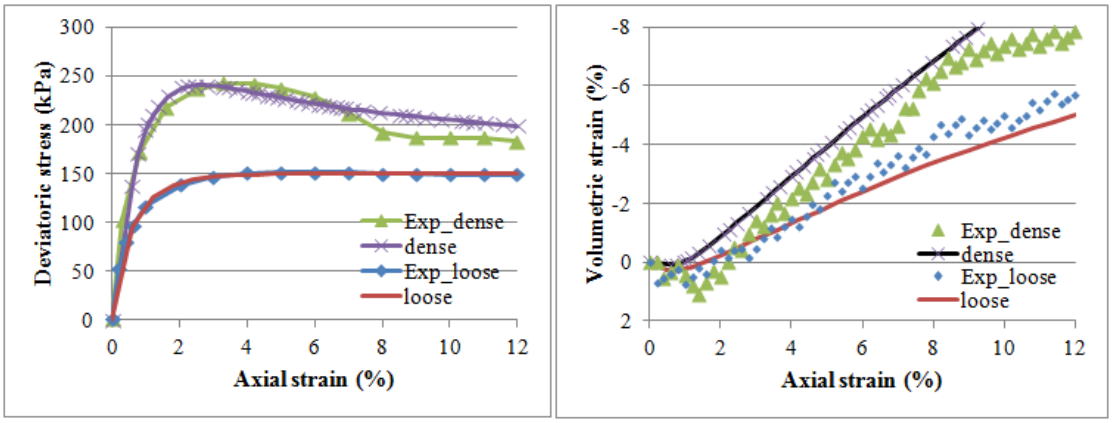

(a) stress-strain curve (b) axial strain vs. volumetric strain

Figure 5. 18 Model predictions in global behavior for dense and loose specimens

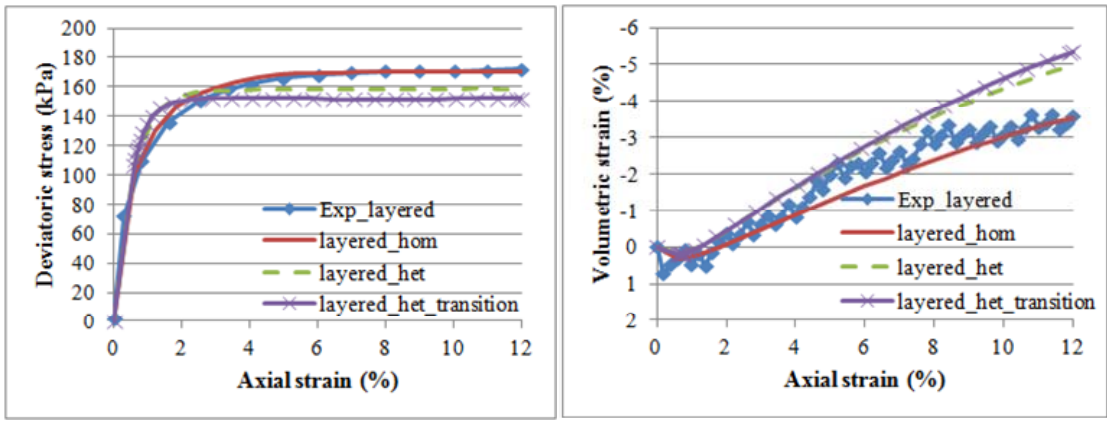

(a) stress-strain curve (b) axial strain vs. volumetric strain

Figure 5. 19 Model predictions in global behavior for a layered specimen

Local deformation of a layered specimen at 12% of axial strain, i.e. critical state is analyzed in Figure 5.20 and 5.21. Contrary to the global behavior, homogeneous model (layered_hom) shows symmetric deformation in radial direction and it proves the necessity of a heterogeneous model. The first heterogeneous model with two layers, 'layered_het' shows a similar trend of displacement distribution in both radial and

vertical directions. However, at a height between 40mm and 80mm, the model deformation is too stiff to fit the laboratory results. Thus, heterogeneous model (layered_het_transition) introduced a transition zone of 40mm between the upper and lower segments to allow for changes in the stiffness of sands. The layered_het_transition model has better agreement with minor deviations of 1mm in both the radial and vertical displacements rather than the other two layered model predictions.

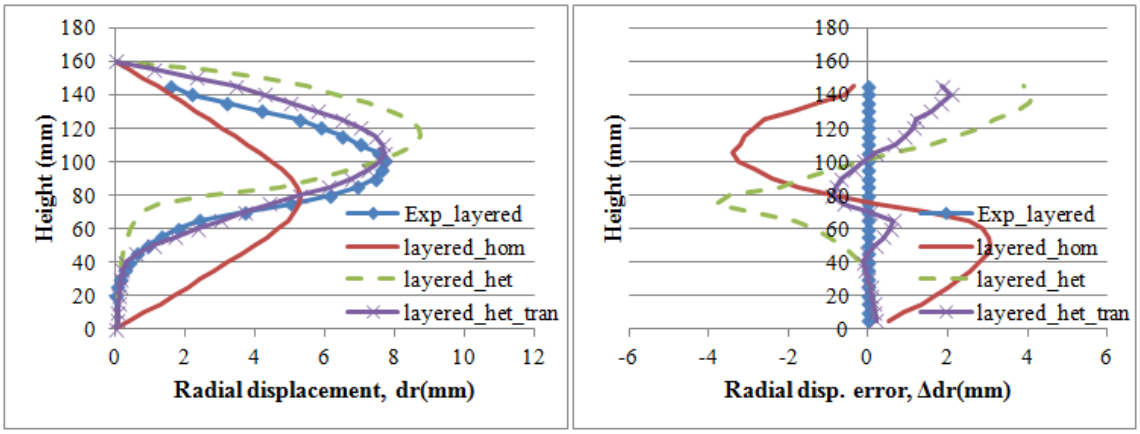

(a) radial diaplecement (b) radial displacement error

Figure 5. 20 Radial displacement distributions and its errors (a) radial displacement distribution (b) radial displacement errors

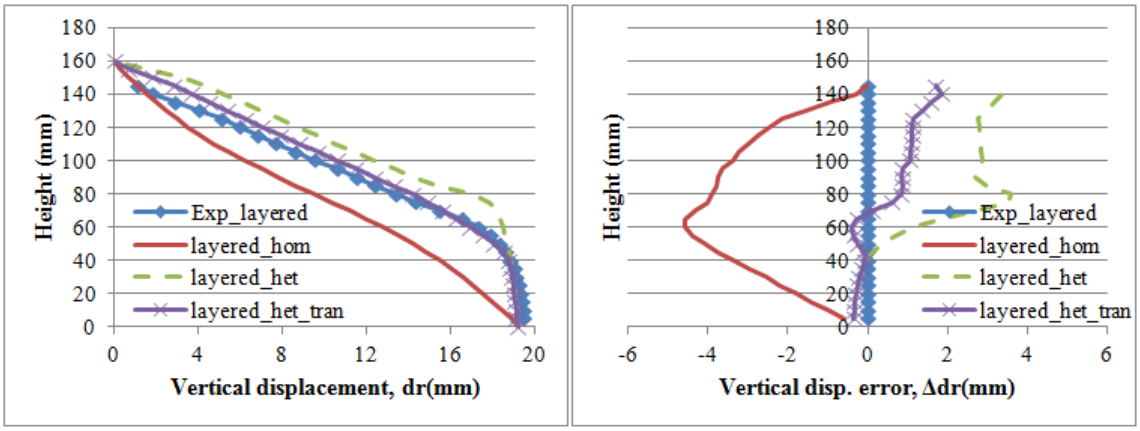

(a) vertical diaplecement (b) vertical displacement error

Figure 5. 21 Vertical displacement distributions and its errors (a) vertical displacement distribution (b) vertical displacement errors

Total displacement vectors and a deformed mesh of layered specimen prediction models are illustrated in Figure 5.22. The homogeneous model, layered_hom, is deformed in a shape of a barrel like a loose sand. In the heterogeneous models, layered_het and layered_het_transition, deformations mainly occurred in the loose specimen section.

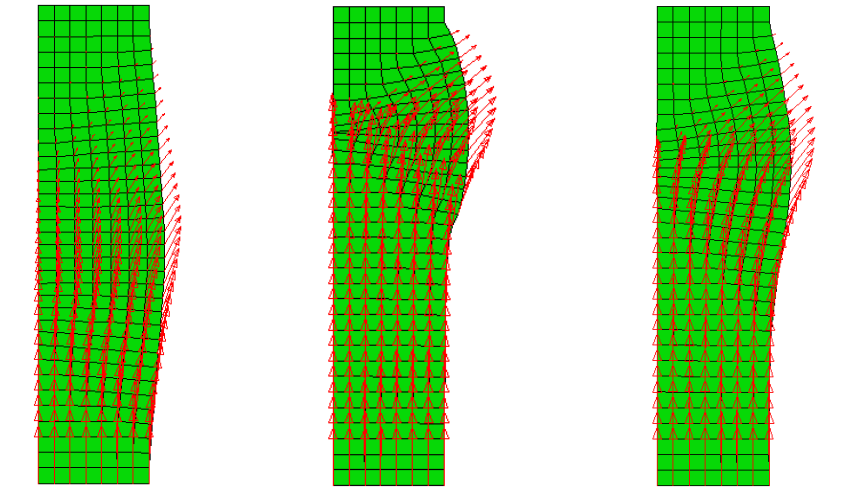

(a) Layered_hom (b) Layered_het (c) Layered_het_transient

Figure 5. 22 Total displacement vectors (a) layered_hom (b) layered_het (c) layered_het_transition

6. CONCLUSIONS

3D digital image correlation provides local displacement information that enables the determination of model parameters for the modeling of local kinematic effects. After the digital image correlation, post-processing analyses was performed to better align the initial undeformed state with the coordinate system, and to accumulate displacements from the step-wise analyses required to populate the local kinematic effects. The deformation of a representative volume of the material captured by 3D-DIC is used for the estimation of the kinematic and volumetric conditions of the specimen at different stages of deformation, combined with the readings of the global axial compression of the specimen, which allow for the characterization of the Mohr-Coulomb plasticity model with hardening and softening laws.

A 2D axisymmetric finite element model was proposed as a first approach to replicate the local effects. This included an elasto-plastic constitutive model with hardening and softening capabilities. Results of the finite element model showed better agreement on the vertical than in the radial displacements, with higher and unbiased deviations at the peak for the radial displacements over the tangential displacement, and similar unbiased deviations for both the radial and the tangential after the peak.

In order to provide sensitivity of mesh discretization in strain softening, a parametric study of a 2D finite element model was carried out to examine the effects of element type and mesh size. Higher order element types and fine mesh sizes produce more accurate stress and displacement distribution predictions. Another relevant

observation from this investigation was that after the peak strength was reached, the deformation within the specimen tended to localize and became more sensitive to mesh discretization. Still finite element models, with a homogeneous material, have a limitation in modeling non-symmetric displacement distributions by shearing after the peak stress, but give useful information on the variation of plastic strain and stress inside of the specimen.

A comparative analysis of different specimen configurations was performed using a 2D finite element model. The model parameters for an elasto-plastic.model with hardening and softening law were calibrated from the global kinematics of dense and loose specimens. A layered specimen consists of two layers with different relative densities so the material parameters of the two layers were obtained from dense and loose specimens with modifications in a hardening and softening curve. The heterogeneous model with transition zone between loose and dense segments presented better predictions on the local deformation of the layered specimen.

REFERENCES

ABAQUS Inc. (2008). *ABAQUS user's manual, version 6.8*, Hibbitt, Karlsson, and Sorensen., Pawtucket, RI.

Abbo, A.J. (1997). *Finite element algorithms for elastoplasticity and consolidation*, Ph.D. dissertation, The University of Newcastle, New South Wales, Australia.

Almeida, O.D., Lagattu, F., and Brillaud, J. (2008). "Analysis by a 3D DIC technique of volumetric deformation gradients: Application to polypropylene/EPR/talc composites." *Composites Part A: Applied Science and Manufacturing,* 39(8), 1210-1217.

Anand, L., Aslan, O., and Chester, S.A. (2012), "A large-deformation gradient theory for elastic-plastic materials: Strain softening and regularization of shear bands." *International Journal of Plasticity*, 30-31, 116-143.

Atkinson, J.H. and Bransby, P.L. (1978). *The mechanics of soils: an introduction to critical state soil mechanics.* McGraw-Hill, London, UK.

Bayoumi, A. (2006). *New laboratory test procedure for the enhanced calibration of constitutive models*, Ph.D. dissertation, Georgia Institute of Technology, Atlanta, GA.

Belheine, N., Plassiard, J.-P., Donze, F.-V., Darve, F., and Seridi, A. (2009). "Numerical simulation of drained triaxial test using 3D discrete element modeling." *Computers and Geotechnics,* 36(1-2), 320-331.

Brinkgreve, R.B.J. (2005). "Selection of Soil Models and Parameters for Geotechnical Engineering Application." *Soil Constitutive Models: Evaluation, Selection, and Calibration*, Geotechnical Special Publications, 128, 69-98.

Boldyrev, G.G., Idrisov, I.Kh., and Valeev, D.N. (2006). "Determination of parameters for soil models." *Soil Mechanics and Foundation Engineering*, 43(3), 101-108.

Borja, R.I. (2000). "A finite element model for strain localization analysis of strong discontinuous fields based on standard Galerkin approximation." *Computer Methods in Applied Mechanics and Engineering*, 190(11-12). 1529-1549.

Cameron, D.A. and Carter, J.P. (2009). "A constitutive model for sand based on non-linear elasticity and the state parameter." *Computers and Geotechnics*, 36(7), 1219–1228.

Chang, C.S. and Hicher, P.-Y, (2005). "An elasto-plastic model for granular materials with microstructural consideration." *International Journal of Solids and Structures*, 42(14), 4258–4277.

Charalampidou, E.M., Hall, S.A., Stanchits, S., Viggiani, G., and Lewis, H. (2010). "Experimental characterization of shear and compaction band mechanisms in porous sandstone by a combination of AE and 3D DIC." *14th International Conference on Experimental Mechanics*, Poitiers, France, EPJ Web of Conferences, 6.

Chupin, O., Rechenmacher, A.L., and Abedi, S. (2011). "Finite strain analysis of nonuniform dieformation inside shear bands in sands." *International Journal for Numerical and Analytical Methods in Geomechanics*.

Correlated Solutions, Inc. (2010). *VIC-3D*, Columbia, SC.

Das, B. M. (2001). *Principles of geotechnical engineering, 5th edition*, Thomson Learning, Pacific Grove, CA.

de Borst, R., Sluys, L.J., Muhlhaus, H.-B., and Pamin, J. (1993). "Fundamental issues in finite element analyses of localization of deformation." *Engineering Computations*, 10(2), 99-121.

Dean, G. and Crocker, L. (2001). "The use of finite element methods for design with adhesives." *NPL Good Practice Guide*, 48, Teddington, UK.

Desai, C.S. and Siriwardane, H.J. (1984). *Constitutive laws for engineering materials: with emphasis on geologic materials*, Prentice-Hall, Englewood Cliffs, NJ.

Desrues, J. (1996) "Localisation patterns in ductile and brittle geomaterials." *Material Instabilities in Solids*, 137-158.

Desrues, J. and Viggiani, G. (2004). "Strain localization in sand: an overview of the experimental results obtained in Grenoble using stereophotogrammetry." *International Journal for Numerical and Analytical Methods in Geomechanics*, 28(4), 279-321

Duncan, J.M. (1994). "The role of advanced constitutive relations in practical applications." *Proceedings, 13th International Conference Soil Mechanics and Foundation Engineering*, New Delhi, India, 5, 31-48.

Duncan, J.M. (2004). "Friction angles for sand, gravel and rockfill." *Notes of a lecture presented at the Kenneth L. Lee Memorial Seminar*, Long Beach, CA.

Finno, R.J. and Rechenmacher, A.L. (2003). "Effects of consolidation history on critical state of sand." *Journal of Geotechnical and Geoenvironmental Engineering*, 129(4), 350-360.

Foley, J.D., van Dam, A., Feiner, S.K., and Hughes, J.F. (1996). *Computer graphics: principles and practice in C. 2nd edition*, Addison-Wesley Professional, New York, NY.

Frantziskonis, G. and Desai, C.S. (1987a). "Constitutive model with strain softening." *International Journal of Solids and Structures*, 23(6), 733-750.

Frantziskonis, G. and Desai, C.S. (1987b). "Analysis of a strain softening constitutive model." *International Journal of Solids and Structures*, 23(6), 751-767.

Fredlund, D.G., Xing, A., Frelund, M.D., and Barbour, S.L. (1996). "The relationship of the unsaturated soil shear strength function to the soil-water characteristic curve." *Canadian Geotechnical Journal*, 33(3), 440-448.

Gay, O., Boutonnier, L., Foray, P., and Flavigny, E. (2003). "Laboratory characterization of Hostun RF sand at very low confining stresses." *Deformation Characteristics of Geomaterials*, Di Benedetto et al. eds., 423-430.

Helwany, S. (2007). *Applied soil mechanics: with ABAQUS applications*, John Wiley & Sons, Hoboken, NJ.

Hicher, P.Y. and Shao, J.F. (2008). *Constitutive modeling of soils and rocks*, John Wiley & Sons, Hoboken, NJ.

Holtz, R.D. and Kovacs, W.D. (1981). *An introduction to geotechnical engineering*, Prentice-Hall, Englewood Cliffs, NJ.

Iskander, M. (2010). *Modelling with transparent soils: visualizing soil structure interaction and multi phase flow, non-intrusively*, Springer Series in Geomechanics and Geoengineering, Springer-Verlag Berlin Heidelberg, New York, NY.

Lade, P.V. (2005). "Overview of constitutive models for soils." *Soil constitutive models: Evaluation, selection and calibration*, Yamamuro, J.A. and Kalaikin, V.N. eds., ASCE Geotechnical Special Publication, No.128, 1-34.

Lava, P., Coppieters, S., Wang, Y., Van Houtte, P., and Debruyne, D. (2011). "Error estimation in measuring strain fields with DIC on planar sheet metal specimens with a non-perpendicular camera alignment." *Optics and Laser in Engineering*, 49(1), 57-65.

Macari, E.J., Parker, J.K., and Costes, N.C. (1997). "Measurement of volume changes in triaxial tests using digital imaging techniques." *Geotechnical Testing Journal*, GTJODJ, 20(1), 103-109.

McNeill, S.R., Sutton, M.A., Miao, Z., and Ma, J. (1997). "Measurement of surface profile using digital image correlation." *Experimental Mechanics*, 37(1), 13-20.

Medina-Cetina, Z. (2006). *Probabilistic calibration of soil constitutive models*, Ph.D. dissertation, Johns Hopkins University, Baltimore, MD.

Medina-Cetina, Z. and Rechenmacher, A. (2010). "Influence of boundary conditions, specimen geometry and material heterogeneity on model calibration from triaxial tests." *International Journal for Numerical and Analytical Methods in Geomechanics*, 34(6), 627-643.

Nuth, M. and Laloui, L. (2008), "Effective stress concept in unsaturated soils: Clarification and validation of a unified framework." *International Journal for Numerical and Analytical Methods in Geomechanics*, 32(7), 771-801.

Peterson, R.F.W. (1988). "Interpretation of triaxial compression test results on partially saturated soils." *Advanced Triaxial Testing of Soil and Rock*, American Society for Testing and Materials, ASTM STP 977, 512-538.

Pietruszczak, ST. and Mroz, Z. (1981). "Finite element analysis of deformation of strain-softening materials." *International Journal for Numerical Methods in Engineering*, 17(3), 327-334.

Pietruszczak, ST. and Stolle, D.F.E. (1985). "Deformation of strain softening materials. Part I: Objectivity of finite element solutions based on conventional strain softening formulations." *Computer and Geotechnics*, 1(2), 99-115.

Potts, D.M. and Zdravkovic, L. (1999). *Finite element analysis in geotechnical engineering: Volume 1-Theory*, Thomas Telford Publishing, London, UK.

Potts, D.M. (2003). "Numerical analysis: a virtual dream or practical reality?" *Géotechnique*, 53(6), 535-573.

Powrie, W. (1997). *Soil mechanics: concepts and applications*, E&FN Spon, Oxford, UK.

Read, H.E. and Hegemier, G.A. (1984). "Strain softening of rock, soil and concrete – A review article." *Mechanics of Materials*, 3(4), 271-294.

Rechenmacher, A.L. (2006). "Grain-scale processes governing shear band initiation and evolution in sands." *Journal of the Mechanics and Physics of Solids*, 54(1), 22-45.

Schofield, A.N. and Wroth, P. (1968). *Critical state soil mechanics*, McGraw-Hill, New York, NY.

Sloan, S.W., Abbo, A.J., and Sheng, D., (2001). "Refined explicit integrateion of elastoplastic models with automatic error control." *Engineering Computations*, 18(1-2), 121-154.

Sloan, S.W. and Booker, J.R., (1986). "Removal of singularities in Tresca and Mohr-Coulomb yield functions." *Communications in Applied Numerical Methods*, 2(2), 173-179.

Steinmann, P. and William, K. (1991). "Performance of enhanced finite element formulations in localized failure computations." *Computer Methods in Applied Mechanics and Engineering*, 90(1-3). 845-867.

Sutton, M.A., McNeill, S.R., Helm, J.D., and Chao, Y.J. (2000). "Advances in two-dimensional and three-dimensional computer vision." *Photomechanics (Topics in Applied Physics)*, Rastogi, P.K. ed., 77, 323-372.

Sutton, M.A., Yan, J.H., Tiwari, V., Schreier, H.W., and Orteu, J.J. (2008). "The effect of out-of-plane motion on 2D and 3D digital image correlation measurements." *Optics and Lasers in Engineering*, 46(10), 746-757.

Tai, Y.H., Zanganeh, M., Asquith, D., and Yates, J.R. (2010). "Characterisation of full-field deformation behaviour using digital imaging techniques." *Applied Mechanics and Materials*, AMM, 24-25, 141-146.

The MathWorks, Inc. (2009). *MATLAB version R2009b*, Natick, MA.

Vesic, A.S., and Clough, G.W. (1968). "Behaviour of granular material under high stresses." *Journal of Soil Mechanics Foundation Devision*, 94, 661-688.

Wan, R.G., and Guo, P.J. (1998). "A simple constitutive model for granular soils: Modified stress-dilatancy approach." *Computers and Geotechnics*, 22(2), 109-133.

Wells, G.N., Sluys, L.J., and de Borst, R. (2002). "Simulating the propagation of displacement discontinuities in a regularized strain-softening medium." *International Journal for Numerical Methods in Engineering*, 53(5), 1235-1256.

Zienkiewicz, O.C. and Taylor, R.L. (2000). *The finite element method: Volume 1. Basic formulation and linear problems, Volume 2. Solid mechanics, 5th edition,* Butterworth-Heinemann, Woburn, MA.

VITA

Name: Ahran Song

Address: Zachry Department of Civil Engineering
Texas A&M University
College Station, TX 77843-3136

Email Address: arsong@neo.tamu.edu

Education: B.S., Civil and Environmental Engineering,
Sungkyunkwan University,
South Korea, 2005
M.S., Geotechnical Engineering,
Sungkyunkwan University,
South Korea, 2007
Ph.D., Geotechnical Engineering,
Texas A&M University, 2012